ISSN: 1949-243X (Print), 1947-3818 (Online) Volume 1, Number 2, November 2009

Energy and Power Engineering

www.scirp.org/journal/epe

Scientific Research

Journal Editorial Board

ISSN: 1949-243X (Print) ISSN: 1947-3818 (Online)

http://www.scirp.org/journal/epe

Editor-in-Chief

Prof. Kaipei LIU Wuhan University, China

Editorial Board

Prof. Ji CHEN University of Houston, USA

Dr. Xijiang HAN Harbin Institute of Technology, China

Dr. Jiangjun RUAN Wuhan University, China

Dr. Yinbiao SHU Executive vice president of State Grid, China

Prof. Yonghua SONG Tsinghua University, China

Prof. Felix WU University of Hong Kong, China

Dr. Ben YOUNG The University of Hong Kong, China

Dr. Wenhua YU Pennsylvania State University University, USA

Dr. Jun ZOU Zhejiang University, China

Energy and Power Engineering, 2009, 65-127
http://www.scirp.org/journal/epe

Table of Contents

Computational Aspects of Electromagnetic Fields near H.V. Transmission Lines……65
Ossama E. GOUDA, Ghada M. AMER, Waleed A. SALEM

Wind-Solar Hybrid Electrical Power Production to Support National Grid: Case Study - Jordan……72
Ghassan HALASA, Johnson A. ASUMADU

Biomass Production of Poplar Plantation Ecosystem in Yangtze River Beach Land……..……81
Jianfeng ZHANG, Qixiang SUN, Jinxing ZHOU, Qihua SHAN, Lixun WU

Heat Transfer by Natural Convection from a Vertical and Horizontal Surfaces Using Vertical Fins……..…85
H. R GOSHAYESHI, F. AMPOFO

Modeling of the Unburned Carbon in Fly Ash……....……..…90
Weiping YAN, Jun LI

A New Multi-Method Combination Forecasting Model for ESDD Predicting……..…94
Haiyan SHUAI, Qingwu GONG

Power Management Integrated Circuit with 90Plus Efficiency Used in AC/DC Converter……100
Yanfeng JIANG

Optimal Performance for Solar Thermal Power System……..…110
Jianfeng LU, Jing DING, Jianping YANG

Study on Lignite-Blended Burning Technology in the 1025t/h Bituminous Boiler……..…116
Jinfeng MA, Jingxing WU, Tianshu ZHOU, Jie LENG, Chong JIANG

The Resuming Insulation Discharge Failure and Conductor Overheating Failure Judgment Method of SF_6 Electrical Equipment……..…122
Xiansheng ZHUANG, Zhi LI, Chengji HUANG

Copyright © 2009 SciRes

Energy and Power Engineering (EPE)

Journal Information

SUBSCRIPTIONS

Energy and Power Engineering (Online at Scientific Research Publishing, www.SciRP.org) is published quarterly by Scientific Research Publishing, Inc., USA.

E-mail: epe@scirp.org

Subscription rates: Volume 1 2009
Print: $50 per copy.
Electronic: free, available on www.SciRP.org.
To subscribe, please contact Journals Subscriptions Department, E-mail: epe@scirp.org

Sample copies: If you are interested in subscribing, you may obtain a free sample copy by contacting Scientific Research Publishing, Inc. at the above address.

SERVICES

Advertisements
Advertisement Sales Department, E-mail: epe@scirp.org

Reprints (minimum quantity 100 copies)
Reprints Co-ordinator, Scientific Research Publishing, Inc., USA.
E-mail: epe@scirp.org

COPYRIGHT

Copyright© 2009 Scientific Research Publishing, Inc.

All Rights Reserved. No part of this publication may be reproduced, stored in a retrieval system, or transmitted, in any form or by any means, electronic, mechanical, photocopying, recording, scanning or otherwise, except as described below, without the permission in writing of the Publisher.

Copying of articles is not permitted except for personal and internal use, to the extent permitted by national copyright law, or under the terms of a license issued by the national Reproduction Rights Organization.

Requests for permission for other kinds of copying, such as copying for general distribution, for advertising or promotional purposes, for creating new collective works or for resale, and other enquiries should be addressed to the Publisher.

Statements and opinions expressed in the articles and communications are those of the individual contributors and not the statements and opinion of Scientific Research Publishing, Inc. We assumes no responsibility or liability for any damage or injury to persons or property arising out of the use of any materials, instructions, methods or ideas contained herein. We expressly disclaim any implied warranties of merchantability or fitness for a particular purpose. If expert assistance is required, the services of a competent professional person should be sought.

PRODUCTION INFORMATION

For manuscripts that have been accepted for publication, please contact:
E-mail: epe@scirp.org

Energy and Power Engineering, 2009, 65-71
doi:10.4236/epe.2009.12010 Published Online November 2009 (http://www.scirp.org/journal/epe)

Computational Aspects of Electromagnetic Fields near H.V. Transmission Lines

Ossama E. GOUDA[1], Ghada M. AMER[2], Waleed A. SALEM[2]
[1]*the Engineering College, Cairo University, Cairo, Egypt*
[2]*the High Institute of Technology, Benha University, Benha, Egypt*
Email: *prof_ossama*11@*yahoo.com*, {*dr_ghada*, *eng_waleed*269}@*benha-univ.edu.eg*

Abstract: Biological effects of electromagnetic fields on the human body, animals and plants have been a subject of scientific interest and public concern for their risk on the living organisms such as blood leukemia and others. The high voltage transmission and distribution lines, which pass beside some houses, factories and schools are source of electromagnetic fields. This paper presents the field calculations around and near of high voltage transmission lines 220 kV and 500kV. To calculate the induced current, the power density, the electric field and the magnetic field of grounded and ungrounded human body cylindrical model are used. MATLAB program package is used for mathematical calculation of the distribution of the EMF in human body under high voltage power transmission lines.

Keywords: computational aspects, EMF, H. V., transmission lines

1. Introduction

Electric and magnetic fields produced by electric power systems have recently been added to the list of environmental agents that are a potential threat to public health [1, 2]. The increasing use of distribution and transmission of electrical energy between randomly occurring causes concerns regarding the risks of human exposure to near-field radiation from the transmission lines and electric substations. The studies into the health effects of long-term exposure have been progressing on several fronts [1]. At ground level, beneath high-voltage transmission lines, the electric fields created have the same frequencies as those carried by the power lines. The characteristics of these fields depend on the line voltage, and on the geometrical dimensions and positions of the conductors of the transmission line. [1] Inside buildings near HV transmission lines, the field strengths are typically lower than the unperturbed field by a factor of about 10-100, depending on the structure of the building and the type of materials [1]. The magnetic field beneath high-voltage overhead transmission lines is directed mainly transversely to the line axis. In this paper calculations are carried out for the electromagnetic fields near the overhead transmission lines and also the induced current produces in human body due to these fields.

2. Computational Model for EMF under H.V. Transmission Line Calculation

In this paper the electric field E, induced in the human body when exposed to a transmission power line electric field E^{inc}, is determined in analytical form using the surface integral equation method. Account is taken of the presence of the earth below the three-phase Power line [3]. Model of long-distance power line consists of three-phase power lines which are arranged in several different configurations that are used in this study. The central conductor number l is in the plane y = 0, while conductors number 2 and number 3 are respectively in the planes y = L and y = -L. Three conductors in the plane z=d in the air (Region 0) above the surface z = 0 of the earth (Region 1) are shown in Figure 1. The electromagnetic fields near 220 kV and 500 kV high voltage tower are calculated in three dimensions by using (1) to (6). The analytical formulas for the field calculations of the three phase's power system are derived in [4] Final Stage

$$E_{0x}(0,y,z)=\frac{i\omega\mu_0 l}{\pi k_1^2}(k_0 d)\left\{\frac{(z+d)^2-y^2}{[(z+d)^2+y^2]^2}+e^{\frac{i2\pi}{3}}\left[\frac{(z+d)^2-(y+L)2}{[(z+d)^2+(y+L)^2]^2}\right]\right.$$
$$\left.+e^{-\frac{i2\pi}{3}}\left[\frac{(z+d)^2-(y-L)2}{[(z+d)^2+(y-L)^2]^2}\right]\right\} \quad (1)$$

Copyright © 2009 SciRes

$$E_{0y}(0,y,z)=\frac{i\omega\mu_0 l}{2\pi k_0}\left\{y\left[\frac{1}{(z-d)^2+y^2}-\frac{1-\frac{2k_0^2}{k_1^2}}{(z+d)^2+y^2}\right]+e^{\frac{i2\pi}{3}}(y+L)\left[\frac{1}{(z-d)^2+(y+L)^2}-\frac{1-\frac{2k_0^2}{k_1^2}}{(z+d)^2+(y+L)^2}\right]\right.$$

$$\left.+e^{-\frac{i2\pi}{3}}(y-L)\left[\frac{1}{(z-d)^2+(y-L)^2}-\frac{1-\frac{2k_0^2}{k_1^2}}{(z+d)^2+(y-L)^2}\right]\right\} \tag{2}$$

$$E_{0z}(0,y,z)=\frac{\omega\mu_0 l}{2\pi k_0}\left\{\frac{z-d}{(z-d)^2+y^2}-\frac{z+d}{(z+d)^2+y^2}+e^{i2\pi/3}\left[\frac{z-d}{(z-d)^2+(y+L)^2}-\frac{z+d}{(z+d)^2+(y+L)^2}\right]\right.$$

$$\left.+e^{-i2\pi/3}\left[\frac{z-d}{(z-d)^2+(y-L)^2}-\frac{z+d}{(z+d)^2+(y-L)^2}\right]\right\} \tag{3}$$

$$B_{0x}(0,y,z)=-\frac{2i\mu_0 l k_0}{\pi k_1^2}\left\{\frac{y(z+d)}{[(z+d)^2+y^2]^2}+e^{i2\pi/3}\frac{(y+L)(z+d)}{[(z+d)^2+(y+L)^2]^2}+e^{-i2\pi/3}\frac{(y-L)(z+d)}{[(z+d)^2+(y-L)^2]^2}\right\} \tag{4}$$

$$B_{0y}(0,y,z)=\frac{\mu_0 l}{2\pi}\left\{\frac{4(z+d)(k_0 d)}{k_1^2[(z+d)^2+y^2]^2}\left[1-\frac{2[(z+d)^2-y^2]}{(z+d)^2+y^2}\right]-\frac{z-d}{(z-d)^2+y^2}+\frac{z+d}{(z+d)^2+y^2}+e^{i2\pi/3}\left(\frac{4(z+d)(k_0 d)}{k_1^2[(z+d)^2+(y+L)^2]^2}\right.\right.$$

$$\left[1-\frac{2[(z+d)^2-(y+L)^2]}{(z+d)^2+(y+L)^2}\right]-\frac{z-d}{(z-d)^2+(y+L)^2}+\frac{z+d}{(z+d)^2+(y+L)^2}\Bigg)+e^{-i2\pi/3}\left(\frac{4(z+d)(k_0 d)}{k_1^2[(z+d)^2+(y-L)^2]^2}\right.$$

$$\left.\left.\left[1-\frac{2[(z+d)^2-(y-L)^2]}{(z+d)^2+(y-L)^2}\right]-\frac{z-d}{(z-d)^2+(y-L)^2}+\frac{z+d}{(z+d)^2+(y-L)^2}\right)\right\} \tag{5}$$

$$B_{0z}(0,y,z)=\frac{\mu_0 l}{2\pi}\left\{\frac{y}{(z-d)^2+y^2}-\frac{y(1-2k_0^2/k_1^2)}{(z+d)^2+y^2}+\frac{4y(k_0 d)}{k_1^2[(z+d)^2+y^2]^2}\left[1+\frac{2[(z+d)^2-y^2]}{(z+d)^2+y^2}\right]+e^{i2\pi/3}\left(\frac{(y+L)}{(z-d)^2+(y+L)^2}\right.\right.$$

$$\left.-\frac{(y+L)(1-2k_0^2/k_1^2)}{(z+d)^2+(y+L)^2}+\frac{4(y+L)(k_0 d)}{k_1^2[(z+d)^2+(y+L)^2]^2}\left[1+\frac{2[(z+d)^2-(y+L)^2]}{(z+d)^2+(y+L)^2}\right]\right)+e^{-i2\pi/3}\left(\frac{(y-L)}{(z-d)^2+(y-L)^2}\right.$$

$$\left.\left.-\frac{(y-L)(1-2k_0^2/k_1^2)}{(z+d)^2+(y-L)^2}+\frac{4(y-L)(k_0 d)}{k_1^2[(z+d)^2+(y-L)^2]^2}\times\left[1+\frac{2[(z+d)^2-(y-L)^2]}{(z+d)^2+(y-L)^2}\right]\right)\right\} \tag{6}$$

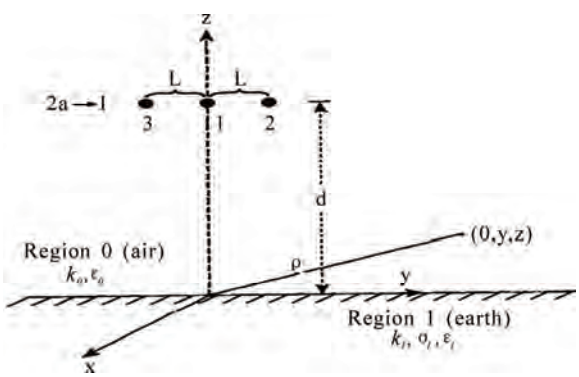

Figure 1. Tower of power line simulation, conductors at height "d" over earth (flat configuration)

where $E_{0x}(0,y,z)$, $E_{0y}(0,y,z)$, and $E_{0z}(0,y,z)$ are electric field components of the three phases in x, y and z planes respectively. $B_{0x}(0,y,z)$, $B_{0y}(0,y,z)$, and $B_{0z}(0,y,z)$ are magnetic field components of the three phases in x, y and z planes respectively. L is the distance between power line phases. d is the vertical distance from the earth to the power lines. I is the line current in ampere. k_0 is the wave number of the air and $k1$ is the wave number of the earth and μ_0 is the permeability of free space. The parameters for the transmission lines 220 kV and 500 kV are given in Table 1. The electromagnetic field for 220 kV and 500 kV are shown in Figures 2 to 10 at distances 0, 2, 4, 6, 8, 10, 12, and 20 meters starting from the transmission lines conductors.

Table 1. the parameters for the transmission lines 220 kV and 500 kV

parameters	220 kV	500 kV
L	3m	12m
D	15m	19.1m
I	300A	1200A
F(frequency)	50 Hz	50 Hz
Z	From 0 to 15 m	From 0 to 18 m

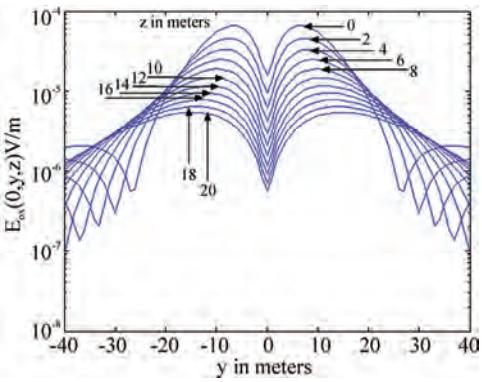

Figure 2. E_{0x} (0, y, z) near a 220kV three-wire power line over vertical distance from 0 to 20 m, current =300 Amp

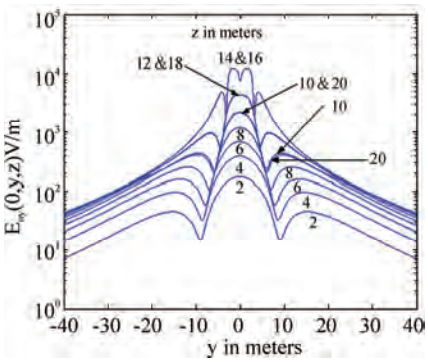

Figure 3. E_{0y} (0, y, z) near a 220kV three-wire power line over vertical distance from 0 to 20 m, current =300 Amp

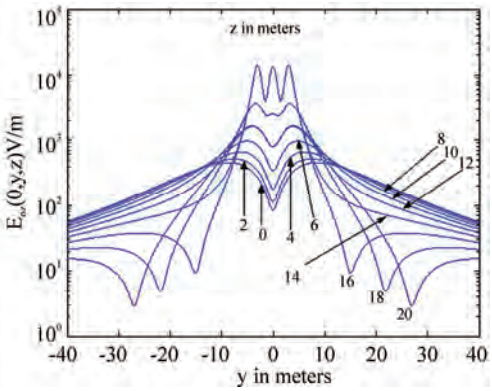

Figure 4. E_{0z} (0, y, z) near a 220kV three-wire power line over vertical distance from 0 to 20 m, current =300 Amp

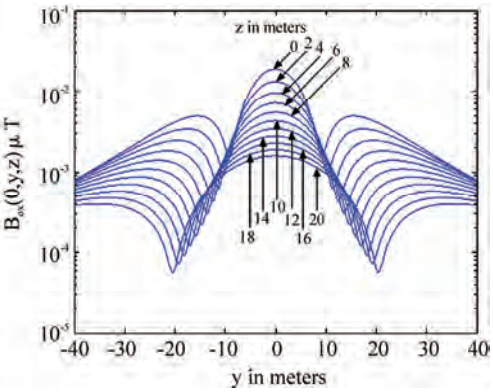

Figure 5. B_{0x} (0, y, z) near a 220kV three-wire power line over vertical distance from 0 to 20 m, current =300 Amp

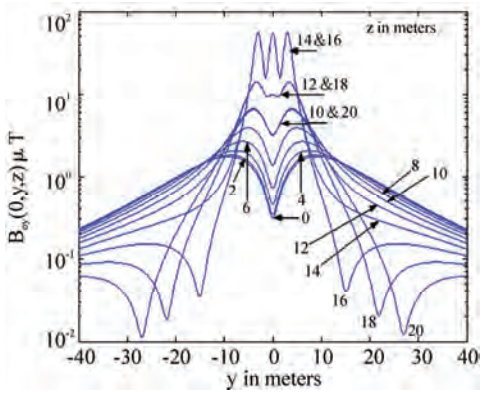

Figure 6. B_{0y} (0, y, z) near a 220kV three-wire power line over vertical distance from 0 to 20 m, current =300 Amp

3. Computational Model for Induced Current in Human Body

The human body is a complex structure with parts like skin, fat, bone, marrow, muscle, blood, nerve fibers, etc., each of which is characterized on the macroscopic level

and within definite boundaries by a conductivity σ and a relative permittivity ε_r, that may be frequency dependent and anisotropic. The average conductivity σ for most tissue types 0.5 S/m is taken in calculation of electric field inside human body [5]. To study the induced current, the power density, the electric field and the magnetic field of grounded and ungrounded human body cylindrical model is represented by a cylinder as shown in Figure 11.

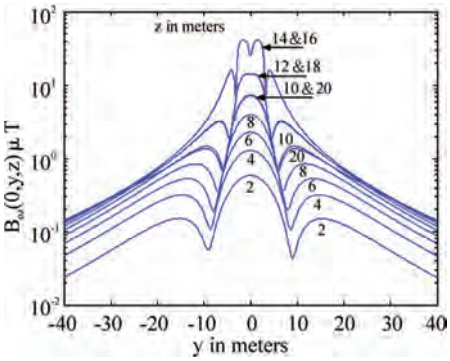

Figure 7. B_{0z} (0, y, z) near a 220kV power line over vertical distance from 0 to 18 m, current =300 Amp

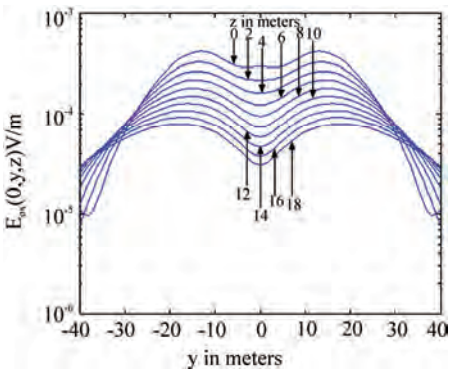

Figure 8. E_{0x} (0, y, z) near a 500kV power line over vertical distance from 0 to 20 m, current =1200 Amp

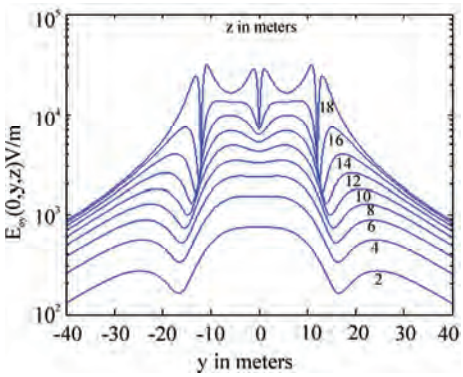

Figure 9. E_{0y} (0, y, z) near a 500kV three-wire power line over vertical distance from 0 to 18 m, current =1200 Amp

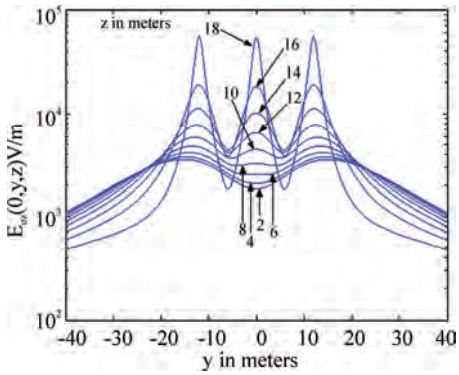

Figure 10. E_{0z} (0, y, z) near a 500kV three-wire power line over vertical distance from 0 to 18 m, current =1200 Amp

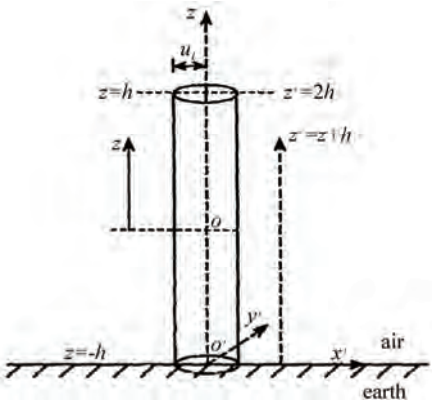

Figure 11. Coordinates x′ , y′, z with origin O on axis at center of cylinder and x′, y′, z′ with origin O ′on axis at base (surface of earth); z′= z+ h, h′=2h

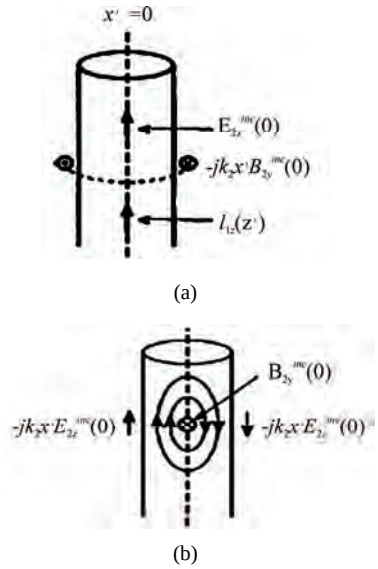

Figure 12. Induced current in a cylindrical conducting body (a) governed by an integral equation (b) governed by ampere's law

The integral equation for the current induced in a cylindrical conducting body as shown in Figure 12 is readily evaluated when the body is electrically short, a) $E_{2z}^{inc}(0)$ and $B_{2y}^{inc}(0)$ induce an axial current $I_{1z}(z')$ by using an integral equation, and b) $E_{2z}^{inc}(0)$ and $B_{2y}^{inc}(0)$ induce a circulating current governed by ampere's law. The circulating current of electric field induced in the cylindrical body by B_{2y}^{inc} component is smaller than that induced by E_{2z}^{inc} and it can be ignored.

When a person is under or near a power line not too close to the earth, such as lying in a bed in an upstairs bedroom near a power line, or a lineman in an elevated basket works under one of the wires, the body acts as an isolated electrically very short parasitic antenna excited by the component of the electric field parallel to its length. Since the body is a good conductor at f= 50 Hz and is long compared with its cross sectional dimensions, the well-known integral equation for the total axial current induced in a conducting cylinder by the field E_s^{inc} can be applied. Here E_s^{inc} is the part of the axial field that is constant in amplitude over any transverse cross section of the body. With a body length 2h = 1.75 m and a mean radius a_l = 0.14 m, the electrical half-length at f= 50 Hz is k_o = 9.l6 X lo^{-7} << 1, where k_o is the wave number of the air. The current induced in a parasitic antenna parallel to an s-directed electric field is [6–10].

$$I_s(s) = \frac{j4\pi E_s^{inc}}{k_0\zeta_0}\frac{\cos k_0 s - \cos k_0 h}{\psi_{dU}\cos k_0 h - \psi_U(h)} \tag{7}$$

where:

s = 0 is the center of the body.

s = ± h are its two ends of the body.

k_o is the wave number of the air, $k_o = \omega/c = 2\pi f/c$ and c is the velocity of the light.

$\zeta_0 = (\mu_0/\varepsilon_o)^{1/2}$, μ_0 is permeability of free space and ε_o is permittivity of free space.

When $k_o h << 1$, (7) can be reduced to

$$I_s(s) = \frac{j2\pi k_0 h^Z E_s^{inc}}{\zeta_0\psi_{dU}}\left(1-\frac{s^Z}{h^Z}\right) \tag{8}$$

Note that the current at the center, s=0, is

$$I_s(0) = \frac{j2\pi k_0 h^Z E_s^{inc}}{\zeta_0\psi_{dU}} \tag{9}$$

where $\psi_{dU} = 2\ln(2h/a_1) - 3$, $k_0 h << 1$

$$E_s(s) = \frac{J_s(s)}{\sigma} = \frac{I_s(s)}{\sigma\pi a_1^Z} \tag{10}$$

The heat generated in the body by J(s) is given by power density

$$P(s) = \sigma\left\|E(s)\right\|^2 \tag{11}$$

the magnetic field in the body due to the axial current $I(s,\rho) = \pi\rho^2 J(s,\rho)$ is given by:

$2\pi p\mu_0^{-1}B(\rho,s) = I_s(\rho,s)$ or $B(\rho,s) = 0.5\rho\mu_0 J_s(s)$

The magnetic field equation can be written as

$$B(\rho,s) = j\pi\rho E_s^{inc}\left(1-\frac{s^2}{h^2}\right)\times 10^{-7} \tag{12}$$

ρ is the radius of the cylinder.

A man in good contact with the earth as shown in Figure 11 can be represented by a cylinder of radius a_1 has a collinear image in the earth. He may have insulated soles with a capacitive impedance Z_L = - j/ ωC between them and their image, or he may be barefooted with Z_L=0. The current in the body in the general case is given by [6]

$$I_Z(Z') = \frac{j2\pi k_0 h'^z E_Z^{inc}}{\zeta_0\psi}\left(1-\frac{Z'^2}{h'^2}+\frac{Z_L}{Z_L+Z_0}\left(1-\frac{Z'}{h'}\right)\right)$$

$$0 \le z' \le h' = 2h \tag{13}$$

where z' = z + h is measured upward from the surface of the earth and h'= 2h is the length of the body (half-length of the body and its image).

$$Z_0 = -\frac{j\varsigma_0\psi}{2\pi k_0 h'_m}, \qquad \psi = 21\ln\frac{2h'_m}{a_m} - 3 \tag{14}$$

where h'_m is the distance from the top of the head at z'= h' to the point of maximum current at z' = z'_m. Z_0 is the impedance of the body referred to the maximum of current at the distance h'_m from the top of the head. z' is the maximum height of human body. z'_m is the point at the maximum current and a_m is the equivalent radius $a_m = (A/\pi)^{0.5}$ where A is the area of the cross section at z'_m. The location of the maximum current is [3]

$$Z'_m = \frac{h'}{2}\frac{Z_L}{Z_0+Z_L} \tag{15}$$

So that

$$h'_m = h'\left(1-\frac{1}{2}\frac{Z_L}{Z_0+Z_L}\right) \tag{16}$$

When (13) is expressed in terms of z and h, it becomes

$$I_Z(Z) = \frac{j2\pi k_0 h^Z E_Z^{inc}}{\zeta_0\psi}\left(1-\frac{z^Z}{h^Z}+\frac{2Z_0}{Z_0+Z_L}\left(1-\frac{z}{h}\right)\right) \tag{17}$$

where z is measured upward from the center of the body and h is its half-length. In (17)

$$Z_0 = -\frac{j\zeta_0\psi}{2\pi k_0 h_m}, \psi = 2\ln\frac{2h_m}{a_m} - 3 \tag{18}$$

where h_m is the distance from the top of the head at z = h to the point of maximum current at z= z_m. Where

$$Z_m = -\frac{Z_0 h}{Z_0+Z_L}, h_m = h\left(1+\frac{Z_0}{Z_0+Z_L}\right) \tag{19}$$

Copyright © 2009 SciRes

Three cases of special interest are:

1) $Z_L = \infty$ this means that the person is far from the surface of the earth.

2) $Z_L = -j/\omega C$ this means that the person is standing on a paved road or sidewalk or directly on the earth with insulating soles, and

3) $Z_L = 0$ this means that the person is barefooted in good contact with the earth.

The first case is given by (8) with s = z. the other two cases are considered as the following: The capacitance C between the soles of the feet and their image is approximately given by (20) and the impedance between the soles of the feet is given by (21). Where A= 0.06 m^2 is the area of the soles, $\varepsilon_r = 2$ is the relative permittivity of the insulating layer of asphalt, cement or rubber and its image, $\varepsilon_o = 8.85\times10^{-12}$ and d is the thickness of the layer and its image [3].

$$C = A\varepsilon_r\varepsilon_0/d \tag{20}$$

$$Z_L = -j/\omega C \tag{21}$$

The electric field, magnetic field, axial current in the human body model, power density, electric and magnetic field due to axial current are calculated for the three cases as:

1) The human is grounded then $Z_L=0$ this means that the person is barefooted in good contact with the earth. With $Z_L=0$, h'=1.75 m, $k_0h'=2.2\times10^{-6}$, $h'_m = h$, $a_m = 0.138$, $\psi=3.47$, and $Z_0 = -j0.79\times10^8$. From (13) takes the form:

$$I_Z(z') = j2.22\times10^{-8} E_z^{inc}\left(1-\frac{z'^Z}{h'^Z}\right), 0 \le z' \le h' \tag{22}$$

2) The human is standing on a paved road or sidewalk or directly on the earth with insulating soles:-consider the first layer is consisting of 13cm of asphalt and 1.5cm of rubber, i.e. the thickness of the layer and its image of two layers is d=29cm, From (20) C = 3.66 $\times10^{-12}$ F, $Z_L = -j8.69\times10^8\ \Omega$ is calculated using (21) where f equals 50 Hz. At $a_m = (A/\pi)^{0.5} = (0.06/\pi)^{0.5} = 0.138$, for maximum current at $z_m = 0.117$ m then h_m=0.992m. From (14) it is found that $Z_0 = -j9.34\times10^7\Omega$ is calculated. The axial current from (17) is calculated by the following equation:

$$I_Z(z) = j8.26\times10^{-9} E_z^{inc}\left(1-\frac{z^Z}{h^Z}+0.194\left(1-\frac{z}{h}\right)\right)$$

$$h \le z \le h \tag{23}$$

3) For a human stand directly on moist earth with rubber soles of 1cm thick, d = 2cm, C = 53.1×10^{-12} F, $Z_L = -j0.6\times10^8\ \Omega$, $z'_m = 0.165h' = 0.289$m, h'm = 0.835h' = 1.461m, $\psi = 3.11$ and $Z_0 = -j0.847\times10^8\ \Omega$. The axial current is calculated as:

$$I_Z(z') = j2.47\times10^{-8} E_Z^{inc}\left(1-\frac{z'^Z}{h'^Z}-0.415\left(1-\frac{z'}{h'}\right)\right)$$

$$0 \le z' \le h' \tag{24}$$

The electric and magnetic fields, the total current, and power densities in the interior of a human body when the body is exposed to 10^4 V/m in the three cases are determined and graphed as shown in Figures 13 to 16.

4. Conclusions

1) The electromagnetic field near a high voltage transmission line is determined in analytical form. Cylindrical model is used in calculating the electric and magnetic fields, the total axial current, and power densities in the interior of a human body are determined when the human is standing on the ground under or near the line .

2) Analytical method is used for calculating the interior currents and power densities of human body when the human body is grounded, isolated by soles and isolated in moist soil.

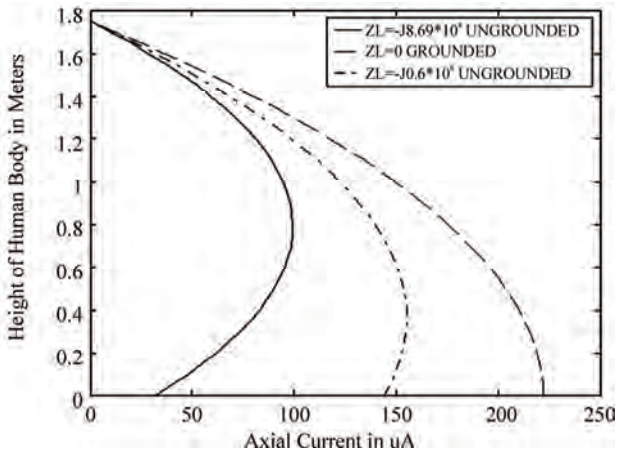

Figure 13. Total axial current in grounded and ungrounded human model; σ=0.5 S/m, $E_z^{inc} = 10^4$ V/m and f =50 Hz

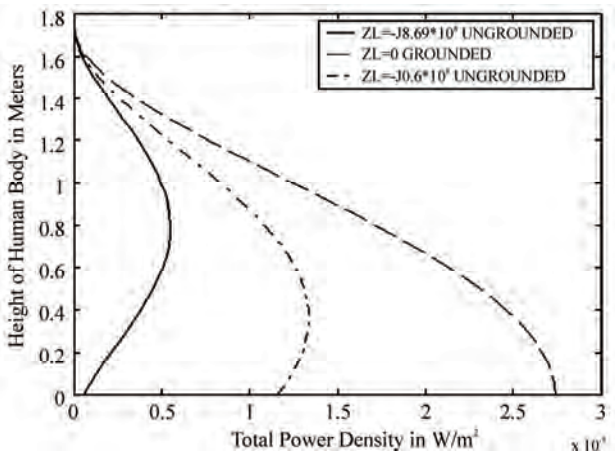

Figure 14. Total power density in grounded and ungrounded human model; σ=0.5 S/m, $E_z^{inc} = 10^4$ V/m and f =50 Hz

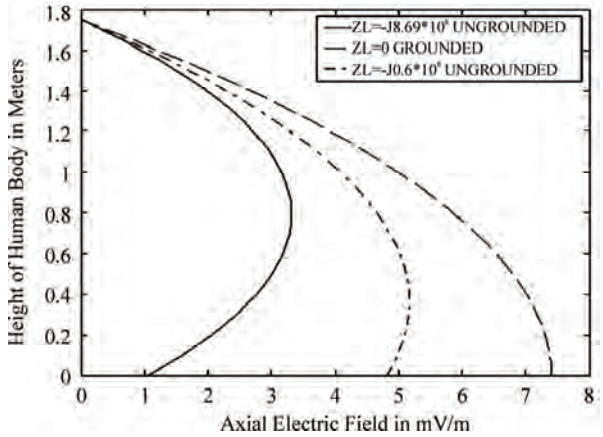

Figure 15. Total axial electric field in grounded and ungrounded human model; σ=0.5 S/m, E_z^{inc} = l0^4 V/m and f =50 Hz

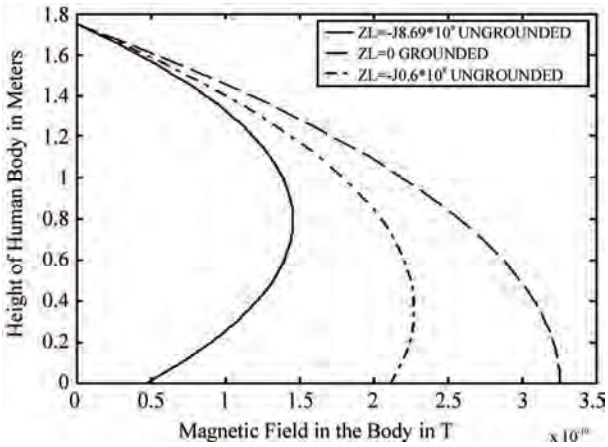

Figure 16. The magnetic field in the body due to axial current in grounded and ungrounded human model; ρ = 0.14m, σ=0.5 S/m, E_z^{inc} = l0^4 V/m

REFERENCES

[1] A. H. E. Manders and N. S. Van Nielen, "The magnetic field surrounding high tension lines in the Netherlands and their influence on humans and animals," Elektrotechniek, Vol. 59, No. 7, 1981.

[2] R. Hauf, "Non-ionizing radiation protection," Copenhagen, World Health Organization Regional Office for Europe, WHO Regional Publications, European Series No. 10, 1982.

[3] R. W. P. Kinga and T. T. Wu, "The complete electromagnetic field of a three-phase transmission line over the earth and its interaction with the human body," Journal of Applied Physics, Vol. 78, No. 2, 1995.

[4] D. Margetis, "Electromagnetic fields in air of traveling-wave currents above the earth," Journal of mathematical physics, Vol. 39, No. 11, pp. 5870–5893, 1998.

[5] F. Barnes and B. Greenebaum, "Book of bioengineering and biophysical aspects of electromagnetic fields," 2006.

[6] J. Jin, "The finite element method in electromagnetics," Wiley, New York, 1993.

[7] D. M. Sullivan, D. T. Borup, and O. P. Gandhi, "Use of the finite-difference time-domain method in calculating EM absorption in human tissues," IEEE Transactions on Bioengineering, Vol. BME-34, pp. 148–157, February 1987.

[8] R. W. P. King, "Fields and currents in the organs of the human body when exposed to power lines and VLF transmitters," IEEE Transactions on Biomedical Engineering, Vol. 45, No. 4, pp. 520–530, April 1998.

[9] D. G. Wu, "Numerical analysis of interactions between fields and human bodies," Ph.D. Thesis, University of Houston, May 2006

[10] A. Barchanski, M. Clemenc, H. De Gersem, and T. Weiland, "Efficient calculation of current densities in the human body induced by arbitrarily shaped, low frequency magnetic field sources," Journal of Computational Physics, Vol. 214, pp. 81–95, 2006.

Copyright © 2009 SciRes

Energy and Power Engineering, 2009, 72-80
doi:10.4236/epe.2009.12011 Published Online November 2009 (http://www.scirp.org/journal/epe)

Wind-Solar Hybrid Electrical Power Production to Support National Grid: Case Study - Jordan

Ghassan HALASA[1], Johnson A. ASUMADU[2]
[1]*Electrical Engineering Department, University of Jordan, Amman, Jordan*
[2]*Electrical and Computer Engineering Department, Western Michigan University, Kalamazoo, USA*
Email: *halasa@ju.edu.jo, johnson.asumadu@wmich.edu*

Abstract: The paper presents the next generation of power energy systems using solar- and wind-energy systems for the country of Jordan. Presently with the oil prices are on the rise, the cost of electrical power production is very high. The opportunity of a large wind and solar hybrid power production is being explored. Sights are chosen to produce electricity using the wind in the Mountains in Northern Jordan and the sun in the Eastern Desert. It is found that the cost of windmill farm to produce 100 - 150 MW is US$290 million while solar power station to produce 100 MW costs US$560 million. The electrical power costs US$0.02/kWh for the wind power and US$0.077 for the solar power. The feasibility for using wind and solar energies is now when the price oil reaches US$ 100.00 per barrel. The paper also discusses different power electronics circuits and control methods to link the renewable energy to the national grid. This paper also looks at some of the modern power electronics converters and electrical generators, which have improved significantly solar and wind energy technologies.

Keywords: solar energy, wind energy, hybrid energy system

1. Introduction

The concept of solar and wind energies dates back to nearly 7,000 years ago [1]. However, in the late 1800s the Danes developed the first wind turbines to produce commercial electricity [1–4]. In the early 1900s small-scale wind turbines became more widely used around Europe especially in the rural areas for producing electricity using old car generators and carved rotors. The wind power brought electricity to the rural areas and the electrical power was used to charge batteries to run radios and to draw water from deep wells [2]. Except in Denmark where wind power production and research continued, wind power did not play any major role in the generation of electricity until the late 1900s.

The rapid growth of solar and wind powers is due in part to favorable global political climate towards these energies, efforts to reduce carbon dioxide (CO_2) and greenhouse gases (GHG) and other power plant pollutants, global awareness of climate changes, and the urgency to develop renewable energy sources. Other factors such as lucrative tax incentives and legislation mandating national renewable energy standards have accelerated the march towards solar and wind energies. For example in the US, some states have enacted "renewable portfolio standard (RPS)" law that requires utilities to sell a certain percentage of the energy from sustainable energy sources within reasonable stipulated times. Even though Europe and North America have the largest installed capacity of wind turbine capacity, China, India, and developing world have the biggest potential for wind power [5].

This paper examines the capacity and potential for electricity-generating solar- and wind-turbines installed In the Eastern and Northern part of Jordan. The Jordan Meteorological Department (JMD) has histological data on wind speeds and sunshine days in areas of the country that can be used to assess the potential for solar and wind energies, and other applications. Jordan has excellent sunshine covering more than 80% of the country (on the average of 330-day in a year). The average wind speed in Jordan is 7 m/s (at 10 meters height above any obstacles within 100 meters) in some parts of the country. Presently, the total renewable energy power generation capacity is about 1% of power generation in Jordan. It is expected that the share of renewable energy in electrical power production will be 15% in the future. Wind Solar alternatives are essential for growth, finance, and the political environment. The cost of wind power has reduced from the cost of power production from US$ 0.09.5 per kilowatt-hour to less than US$0.02 for wind energy production and to US$0.076 cents for solar power production. This is very significant because developing countries, which depend on external sources to finance major energy projects, may be able to finance small scale solar and wind energies projects from their own re-

Copyright © 2009 SciRes

sources and faster. In this paper the electrical and power calculations for solar and wind utilization to support the national grid in Jordan will be analyzed. This paper also looks at some of the modern power electronics converters and electrical machines, which have improved significantly solar and wind energy technologies to make them acceptable and embraced as cost effective and renewable energy.

2. The Existing Jordan's National Grid

Jordan is interconnected in one national grid. The grid covers most of the populated areas of the country from Aqaba, on the far south to Irbid in the far north. Overhead transmission line link Syria in the north, Palestine in the west, while undersea cable links Egypt in the south. Future countries to be connected to the Jordan national grid include Lebanon, Iraq and Turkey.

The major generation centers are the Aqaba Thermal Power Station in the far south, Al-Hussein Thermal Power Station in Zarka near Amman, and Al-Risha near the Iraqi border. The Aqaba Power Station uses gas supplied through pipelines from Egypt. The pipeline extends to Amman. Future expansion of this gas line is expected to go to Syria and eventually Turkey. Al-Hussein power station uses fuel oil imported from Iraq. Al-Risha power station uses locally produced gas. There are several small units scattered in different districts belonging to older utilities. These units are used during peak demands.

The oldest and the highest power production plant in Jordan is the Al-Hussein Thermal Power Station. It is the most expensive because it uses imported oil and also uses air-cooling systems, that consume quite amount of energy, to cool the turbines. A small pilot plant uses biogas produced by sewerage treatment plant. Another pilot plant uses wind energy near the sight proposed in North Jordan. Aqaba Power Station uses Egyptian gas supplied by gas pipeline. This pipeline already extended to Amman. Future expansion of this gas line is expected to go to Syria, and eventually Turkey. Al-Hussein power station uses fuel oil imported fro Iraq. Al-Risha power station uses locally produced gas. There are several small units scattered in different districts belonging to older utilities. These units are used in peak demands.

3. Conventional Electrical Production Cost

The Kingdom of Jordan is considered an emerging country in the Middle East; it has almost no natural resources. The country imports most of its oil needs from neighboring countries at market prices. Oil and gas imports are huge burden on the country's national economy. Electricity is generated by burning imported gas and oil, limited generation from hydro, windmills, and biogas. When oil prices rose to extremely high levels last summer, Jordanians experienced continuous increases in electricity prices. It is now urgent and essential to deploy other alternatives for electrical generation, which is the use of solar and wind energy for electrical generation.

As shown in Table 1, Jordan in 2007 produced a total of 13,001 GWh of electrical energy and consumed 10,553 GWh. The average per capita electricity consumption in Jordan in 2007 was 2277 kWh as compared to 2075 kWh in 2006, resulting in annual growth rate of 9.7%. Table 1 shows generating capacity and electrical energy production by type of generation for 2007.

The state-owned utility National Electric Power Company (NEPCO) currently carries out almost all electricity production in Jordan. Al-Hussein Power Plant (with capacity of 400 MW) and the Aqaba Power Plant (with capacity of 650 MW) are the country's two main power generation facilities.

Jordan has modest reserves of natural gas of 230 billion cubic feet and has developed one gas field–at Al-Risha in the eastern desert near the Iraqi border. The current output of this field is around 30 million cubic feet per day. Al-Risha field is used to fuel one nearby power plant, which generates about 10% of Jordan's electricity. For several years, Jordan has been exploring the option of importing natural gas from Egypt. In 1999, a decision was made to delay imports until a more thorough evaluation of reserves at Al-Risha field was completed. When

Table 1. Energy production in 2007 by generation type [6]

Fuel Type	Generating Plants Capacity (MW)	Electrical Production (GWh)
Steam Units	1013	6,904
Gas Turbines/Diesel	193	45
Gas Turbines/Natural Gas	310	916
Diesel Engines	43	1
Hydro Units	12	61
Windmills	1.4	3
Biogas	4	10
Combined Cycle	600	5,061
Total Generation	2176.4	13,001

Table 2. Fuel consumption in 2007 for electrical generation [6]

Fuel Type	Consumption in Thousands Tons Oil Equivalent
Heavy Fuel	621
Natural Gas	2,396
Diesel	9
Total	3,026

Copyright © 2009 SciRes

this review showed that quantities available were not sufficient to meet the country's needs, Jordan decided to reopen talks on imports from Egypt. A pipeline was constructed and completed in 2006. Aqaba thermal power station, a major generating center, currently uses Egyptian gas. Jordan imports about 150,000 barrels of oil per day mostly from Iraq and Saudi Arabia. The Zarka refinery near Amman, the only refinery in the country, refines the imported oil. Table 2 shows electrical generation fuel consumption in 2007. Gas and oil imports pose a huge burden on the national economy. It is evident that the country is in need for renewable energy projects.

According to 2007 data supplied by NEPCO [6], electrical production cost is US$0.073 per KWh: out of which fuel cost is US$ 0.0386 per KWh. This figure is considered expensive as compared to production cost in other countries. As the oil prices surged to more than double in the summer of 2008, accordingly the production cost increased to US$0.11 per kWh. If it is assumed that the true value of oil price is $100 per barrel, the production cost would be about US$0.095 per kWh. This figure will be used in cost comparison.

4. Assessment of Wind and Solar Energies

In Jordan electricity demand grew at the rate of 9.7% in 2007. The Jordanian government has been seeking ways to attract foreign capital to fund additional capacity. Wind and solar energies as main source of electricity generation are currently set as government priorities. The government implemented the following actions [7]:

- Developing new wind and solar maps for Jordan.
- Developing a legal framework for renewable energy.
- Developing incentives for renewable energy projects.
- Securing appropriate funding to implement the first commercial wind energy project in Jordan.
- Secure appropriate funding to implement the feasibility study of the hybrid solar power plant.

Because of the government enthusiasm to promote renewable energy, a thorough investigation has been conducted to study the possibility for a hybrid system of windmills and solar arrays for electricity generation. Data collected over many years by the JMD [8] has helped in locating the sights for both windmills and solar arrays.

The wind farm location was set in the area of Ras-Munif where the annual wind speed average is 5.5 meters/sec according to data collected by the Meteorological Department in Jordan. With the exception of the months of September and October, where the wind speed is low, the other 10 months the speed varies from 6 to 6.5 meter/sec. This speed represents the village ground level speed. If the windmills are sighted at higher elevation and in the valley curvature between mountains running west to east where wind tunnel effect exists, the average wind speed might rise to comfortable levels where windmills run near full capacity. The windmill tower height of 100 meters also increases wind speed to levels close to the 7-9 meter/sec [9], which might bring the wind turbine power output to 1.0 MW or more. Experience indicates that wind speed tend to be higher during the nighttime. Therefore, during the daytime the deficiency in windmills' power output can be augmented by solar cells. The average sunshine hours throughout the year are 8.5 hours per day. In the summer months, May through September**,** the average sunshine hours are more than 10 hours per day. In winter months, November through February, the average sunshine hours are about 6 hours per day. This means that the solar arrays can supplement the wind turbines daily for 10 hours in the summer and 6 hours in the winter months. The solar arrays can be scattered between the windmill towers.

5. The Windmill-Solar Hybrid System

5.1. Proposed Windmill-Solar Hybrid

The proposed non-conventional electrical generation should supply 100-150 MW. As it was pointed out earlier, the sight is chosen in a high valley curvature in the mountainous range where wind tunnel effect exists when continuous high-speed wind prevails all year round. An array of 100 windmills was chosen for this work. Each unit has a capacity 1.5 MW. Several windmill suppliers were investigated and the choice was set on SAIP Electric Group [10]. Figure 1 shows the windmill chosen for this project. Since the average annual wind speed characteristics at location is 6 meter/sec and might average about 8-9 m/sec as was pointed out in Section 5.0 above.

The cut-in wind speed is 3 m/sec, which is way above the annual average wind speed guaranteeing continuous

Figure 1. The 1.5 MW windmill

Copyright © 2009 SciRes

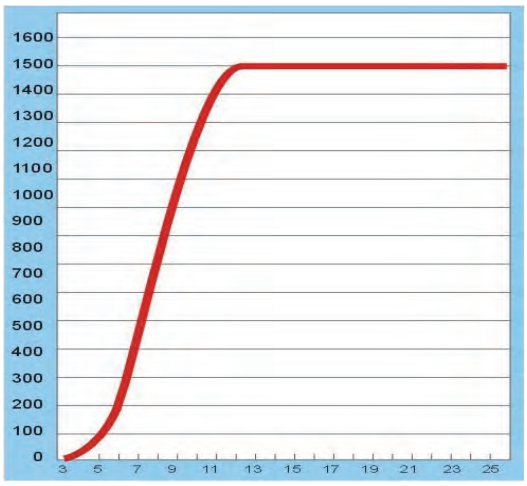

Figure 2. The power-wind speed characteristics

power output. The cutout speed is 25 meter/sec where this average is over 10 minutes on the average. In that location wind speeds never reach that high. Figure 2 indicates that the windmill average power output would be about 1.0 MW for year round.

This power may increase up to 1.5 MW, which is the maximum power output of the generator. Therefore, the proposed windmills farm may produce a continuous power output between 100-150 MW. The blade length is 37.5 m, making the windmill side clearance 75 m, and at a height of 100 m. Leaving additional side clearance of 100 m so that windmills do not form wind obstacles between each other. Therefore, the wind farm array farm should be about 2 km long. Land appropriation for this sight would be about 200,000 m^2.

In case the windmills power output is reduced, solar cells array may be an alternative for additional support and reliability. Experience had told us that whenever the wind speed drops means a fair weather where the sunshine is a maximum.

Table 3 shows the solar array type specifications to be used. The decision was to install solar array to produce 100MW to support the windmill array. A total of 500,000 arrays are needed to supply the required power of 100 MW. The array will be installed in the lower area in the flat planes.

Table 3. Solar module specifications

Maximum power (Wp)	***200W***
Maximum power voltage (V)	42
Maximum power current (A)	5.24
Open circuit voltage (V)	50
Short circuit current (A)	5.7
Number of cells (Pcs)	91(7x13)
Size of module (mm)	1702x945x45
Weight per piece (kg)	19

Since Ras-Munif, the location of the windmills is mountainous area, is also suitable for solar arrays but limited because it can also be used for agricultural plantations. A better location of the solar modules is in the Easter Jordanian Desert. In the desert, land is readily available and the yearly average daily sunshine is 9.3 hours. By installing east-west sun tracing system, a full 8 hours daily average maximum power output can be obtained. Accounting for modules surface area and spaces between modules, the solar installation requires land appropriation of 1.0 km^2.

Location for the solar power station is chosen to be near Al-Risha Power Station currently in operation in the Eastern Jordanian Desert. The sight is chosen for easier link to the national grid. Al-Risha is located at 32˚ latitude. This requires the modules to be installed inclined toward the South at 32˚ with the horizontal; facing southward Modules inclination adjustments of ±15˚ are needed to track the sun's seasonal variations. East-west tracking motors may be used to increase full capacity power production to 9 hours per day.

The proposed hybrid wind-solar installation is needed to supply Jordan with low cost renewable electric power. These two installations are capable of supplying 10% of the country's electricity peak demand needs for the year 2009.

5.2. Cost Estimation

The cost of one windmill is US$ 1.85 million [10]; additional 20% of the price may cover shipping and installation. In addition, US$200,000.00 per unit for controllers and other supporting equipment may be needed for grid link. The total cost per unit ready to supply the grid may be set around US$2.4 million. Another 10% for maintenance, 6% for capital investment, and 5% for administration to be added to the US$2.4 million; results in net cost of US$2.9 million per unit. A total of US$290 million are needed for the wind farm installation to produce 100–150 MW of electrical power. The average lifetime of the windmill is 20 years. Simple calculations, after the assumption that the full wind power output is for 20 hours per day, result in electrical production cost of US$0.02/kWh.

As for the solar power station, the cost of 500,000 modules needed to produce 100 MW is US$370 million. This cost includes the controllers for the ground link. In addition to the US$370 million solar modules cost, 20% for installation, 10% for the sun tracking, 6% capital investment, and 5% for administration, bringing the total cost for the solar power station to US$560 million. The high percentage for installation is to cover the cost of frames upon which the modules will be installed. Remembering that the power production is for 8 hours per day and the lifetime of the solar cells is 25 years; the production cost will be US$0.077/kWh. This production

Copyright © 2009 SciRes

cost is almost the same as the present conventional cost but lower than the projected cost of US$0.09/kWh when the price of oil reaches US$100 per barrel.

Comparing the wind and solar power production costs, it seems that wind power production cost is lower than the solar power production. Therefore, wind energy production is feasible now even with oil prices at US$40 per barrel. In the future when oil prices rise, even with the high cost of solar energy, solar power is important for power floe reliability.

6. Ras-Munif – Village of ‘Ebelin Hybrid Power Project

Ras-Munif, located in the province of Ajloun, is one of the highest mountains in Jordan: about 1198 m above sea level. The villages of ‘Ebelin are also located in the province of Ajloun and 4.9 km from the city center of Ajloun, directly below Ras-Munif, see Figure 3. Land terrain, wind characteristics, solar sunshine days, and politics are considered important issues for the location of wind and solar farms. It is clear that the wind speed and sunshine days data mined by JMD make Ras-Munif an ideal location for wind and solar farms.

6.1. Wind Energy

Wind energy depends mostly on wind speed and kinetic energy of the air mass even though wind speed is also affected by air density, air temperature, air barometric pressure, altitude, and local terrain. Wind generators are practical where the average wind speed is greater than 4.5 m/s and with constant flow rate at minimum turbulence and minimum powerful wind bursts. The Figure 4 shows best wind turbine locations on mountainous terrain.

JMD has kept data of wind speeds and directions at different locations in Jordan; wind speed and direction are very important factors for location of wind farms. Ras-Munif, one of highest mountains in Jordan, is very rich in wind speeds with an average wind speed of 5.5 m/s reaching a maximum value of 6.37 m/s during winter.

Figure 3. Area view of Ras Munif and ‘Ebelin

Site 1:
Ideal – Wind is in all directions

Site 2:
Poor – Wind direction is poor

Site 3:
Good – Wind in two directions

Figure 4. Terrain location of wind turbines

Table 4. Kyocera (kc130gt) solar panel rating

Price Per Panel	431.87JD	Short Circuit Current	8.02 A
Rated Power	130 W	Area of Panel	0.929 m^2
Rated Voltage	17.6 V	At 70% Peak Load	5385
Rated Current	7.39 A	Cells Per Panel	36 Polycrystalline Cells
Open Circuit Voltage	21.1 V	Cost Per KW	US$4681.34/KW

6.2. Solar Energy

Solar energy depends on the amount of direct sunlight even though clouds, blue patches, shades, and rain also affect direct sunlight. Solar panels are located at areas with best sun exposure. Solar panels are practical where the average sunshine is greater than 5 hours a day. The solar panels must be kept cool with minimum clouds (equivalent to approximately 50% peak sun), minimum blue patches and shades (shading even one cell of the panels can reduce the output of an entire array), and less rain (equivalent to approximately 20% peak sun).

JMD has kept data on sunshine hours at different locations in Jordan. Ras-Munif is very rich in sunshine due to its elevation [7–8] with average sunshine of 8.5 hours per day and reaching a maximum of 12.3 hours/day during summer.

6.3. Hybrid Power System

In addition to the present conventional power system, the hybrid power system of Ras-Munif consists of solar panel arrays and generators; the hybrid system is tied in to the conventional system. The output voltage of the solar arrays and the wind generators are tied and synchronized together with the conventional power system main bus at the same potential. The voltage at the main bus is kept constant and used to supply the load. The Figure 5 [7–8] shows the location of the hybrid power generation system located at Ras-Munif, and transmission lines from Ras-Munif to ‘Ebelin villages. The power produced at ‘Ebelin is at 230 V. The solar panel selected and built into the solar arrays, is the low cost Kyocera module KC130GT with rating shown in Table 4.

The solar panels are connected in two format arrays – serial and parallel. The solar panels are connected in series to meet the voltage requirements and in parallel to meet the current requirements. The output of the arrays has a DC/DC converter linkage integrated into voltage-source-inverter (VSI) system to hold the voltage at constant value. The solar panels have sun trackers for adjusting the panel tilts during winter and summer according to the following equations [7–8]:

$$\text{Summer Tilt} = \text{Location Latitude} - 15^\circ \quad (1)$$

$$\text{Winter Tilt} = \text{Location Latitude} + 15^\circ \quad (2)$$

The Ras-Munif site selected has “Location Latitude” of 32˚ with the horizontal facing south.

All the wind generator turbines are the horizontal axis wind turbine types because they are low cost and easy to maintain. The smallest wind generator is rated at least 10 KW. The characteristics of a typical generator are shown in Table 5.

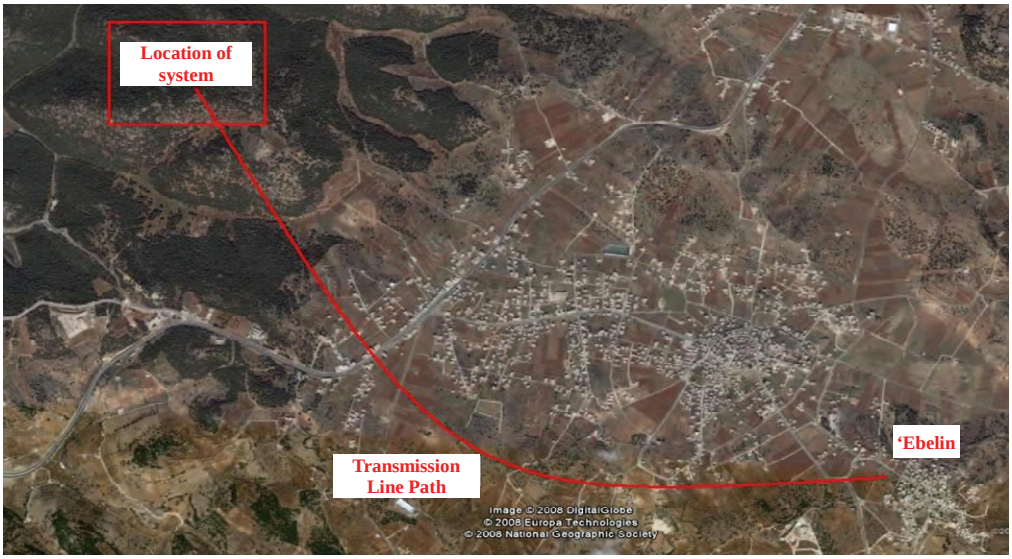

Figure 5. Location of hybrid power system and transmission line path

Table 5. Typical wind turbine characteristics

Power Rating	>10 KW	Blade Material	Fiberglass-reinforced Epoxy
Rated Wind Speed	13 m/s	Yaw Control	Passive Aligned by Tail vane
Cut-in Wind Speed	3 m/s	Rate RPM	25 - 300
Rotor Diameter	> 7 m	Tower Height	12 – 40 m
Number of Blades	3	Weight	Minimum 7540 kg

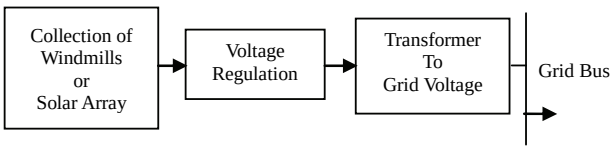

Figure 6. Proposed power system

7. Power Electronics

7.1. Electrical and Power Requirements

The solar- and wind-energy systems must be integrated into the national grid. A block diagram of the proposed is shown in the block diagram of Figure 6.

Papers [11–20] have presented a number of power converter topologies for wind generators for wind energy conversion systems. There are various power electronic converters that have been developed.

Power Electronics converters have been used to extract the maximum power and to allow for variable speed operation of wind turbines. In this project the power electronics converter selected has the following properties: 1) the maximum power obtained from control system of the converter is compared with the maximum power point tracking (MPPT) curve [18–21] at wind speeds/sun shine levels, 2) the converter must provide the required residential/commercial voltage, 3) the converter must provide frequency to within the specified error, and 4) the efficiency for small scale power must be met. A permanent magnetic synchronous generator (PMSG) and a supply-side voltage source inverter (VSI) are selected for the wind-energy for lower cost and higher power output. The DC/DC–VSI combination is capable of handling weak sun AC systems. There are various control strategies for the VSIs including *d*-axis and *q*-axis PI controllers and use of space vector modulation (SVM) to achieve a better modulation index. Even though PMSGs have initial higher cost (price of magnets) and may be demagnetized (high temperatures, overloading, and short circuits), they are flexible, have high output power without the need to increase size of generator, have lower maintenance costs (no carbon brushes, bearings, etc.), have lower losses, have very high torque at low speeds, are self-exciting machines, and do not need cooling systems. A major advantage of using PMSG is that they do not require external excitation and simple diode rectifier circuit may be used at the generator terminals. Figure 7 shows the block diagram of the solar- and wind-energy system.

The solar system includes a boost converter for the MPPT. A DC/DC converter linkage is integrated into the VSI and solar systems 1) to control the generator-side DC-generator for both the solar and wind systems, 2) to maintain the desired DC-voltage for the inverter-side, 3) to eliminate certain harmonics, and 4) to provide more flexible control. The wind-generator output power is maximized using MPPT control systems and algorithms. The *p-q* theory [22] is used to control the active and reactive power, and the power factor.

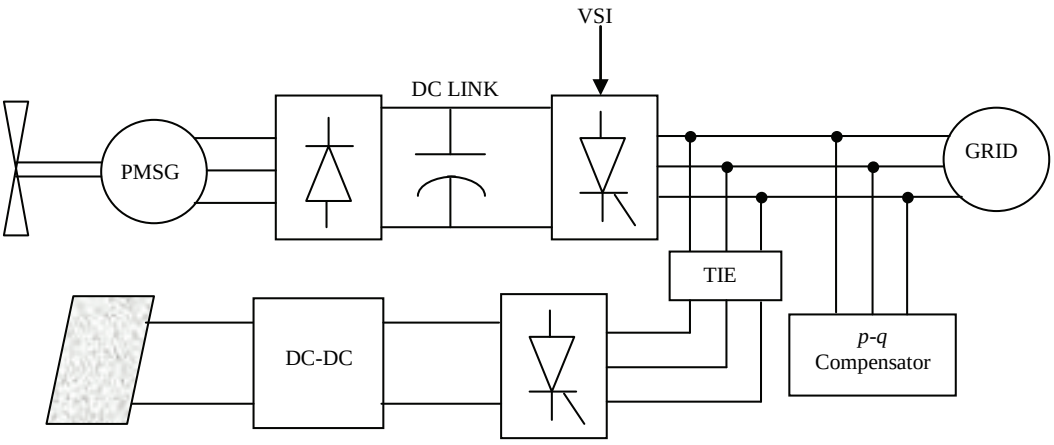

Figure 7. Hybrid solar- and wind-energy power system

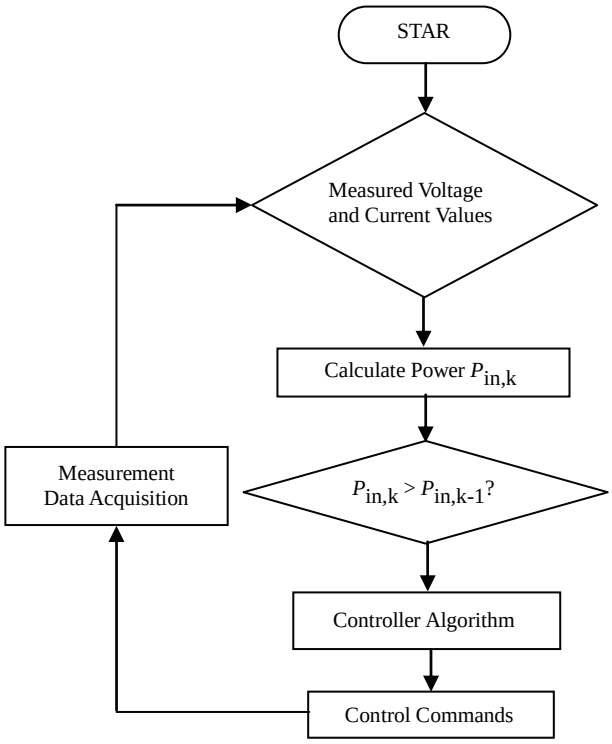

Figure 8. MPPT control algorithm process

The MPPT can be used to achieve optimal operation mode of the solar-and wind-generator power conversion system. The MPPT does not require knowledge of optimal power characteristics or measurement of wind speed, does not depend on the rotor-speed rating of the wind-generator, and does not depend on the power rating of the DC-DC converter. The required voltage and current signals are measured using sensors such as Hall Effect or linear electro-magnetic (LEM) sensors through analog-to-digital (ADC) converters.

The Figure 8 shows a generic representative flowchart of an MPPT control algorithm. In the flowchart the MPPT battery system is not taken into consideration. The error signals are obtained by comparing the reference control signals and corresponding measured values.

The MPPT algorithm is then applied to the error signals. The duty-cycle ratio change command is then implemented.

8. Conclusions

Jordan has high electric production cost that is directly linked with oil prices. An alternative is renewable wind and solar electric power production. The possibility was thoroughly investigated. The result is to install windmill farm in the mountainous area in the north, where wind speed proved to be viable, while the eastern desert is suitable to install solar power station. The cost for the windmill farm to produce 100 – 150 MW for 20 hours per day is US$290 million. The cost of the solar power station to produce 100 MW for 8 hours per day is US$560 million. The production cost is US$0.02/kWh for the windmill and US$0.077/kWh for the solar. The conventional production cost is US$0.095/kWh projected when the price of oil is US$100 per barrel. For reliable energy system, hybrid power production is essential.

The features of the generator-converter are considered to meet the requirements for the wind and solar systems. The solar- and wind-generator power outputs can be maximized using MPPT control systems and algorithms. The *p-q* theory is used to control the active and reactive power, and the power factor.

REFERENCES

[1] N. Kodama, T. Matzuzaka, and N. Inomita, "power variation control of a wind turbine using probabilistic optimal control, including feed-forward control for wind speed," Wind Engineering, Vol. 24, No. 1, pp. 13–23, January 2000.

[2] L. L. Freris, "Wind energy conversion systems," Englewood Cliffs, NJ, Prentice-Hall, pp. 182–184, 1990.

[3] E. Koutroulis and K. Klaitzakis, "Design of a maximum power tracking system for wind-energy-conversion applications," IEEE Transaction on Industrial Electronics, Vol. 53, No. 2, pp. 486–494, April 2006.

[4] E. Muljadi and C. P. Butterfield, "Pitch-controlled variable-speed wind turbine generation," IEEE Transaction on Industry Applications, Vol. 37, No. 1, pp. 240–246, January 2001.

[5] W. Lin, H. Matsuo, and Y. Ishizuka, "Performance characteristics of buck-boost type two-input DC-DC converter with an active voltage clamp," IEICE Technique Report, Vol. 102, No. 567, pp. 7–13, January 2003.

[6] http://www.nepco.com.jo/showImageTC.aspx?imageURL=Statistics_files/Englishalbums/2/, Retrieved on 2/3/2009.

[7] http://www.ren21.net/iap/commitment2.asp?id=93, Retrieved 3/3/2009

[8] The Hashimite Kingdom of Jordan, Meteorological Department, Climate Division, Jordan Climatic Data, 2007.

[9] E. W. Peterson and J. P. Hennessey Jr., "On the use of power laws for estimates of wind power potential, Journal of Applied Meteorology, Vol. 17, 1978.

[10] SAIP Electric Group Limited, Huifeng Road, Luishi Industrial Zone, Wenzhou, Zhejiang, 325604, China.

[11] J. A. Baroudi, V. D. Dinavahi, and A. M. Knight, "A review of power converter topologies for wind generators," Renewable Energy 32, Science Direct, pp. 229–238, January, 2007.

[12] Z. Chen and E. Spooner, "Current source thyristor inverter and its active compensation system," Proceedings of IEE Generation, Transmission, and Distribution, Vol. 150, pp. 447–454, July 2003.

Copyright © 2009 SciRes

[13] K. Tan and S. Islam, "Optimum control strategies in energy conversion of PSMG wind turbine system without mechanical sensors," IEEE Transaction on Energy Conversion, Vol. 10, pp. 392–399, 2004.

[14] Z. Chen and E. Spooner, "Grid power quality with variable speed wind turbines," IEEE Transaction on Energy Conversion, Vol. 16, 2001, pp. 148–154.

[15] Z. Chen and E. Spooner, "Wind turbine power converters: A comparative study," Proceedings of IEE Seventh International Conference on Power Electronics and Variable Speed Drives, pp. 471–476, September 1998.

[16] S. H. Song, S. Kang, and N. Hahm, "Implementation and control of grid connected AC-DC-AC power converter for variable speed wind energy conversion system," Proceedings of IEEE AIPEC'03, Vol. 1, pp. 154–158, February 2003.

[17] Y. Higuchi, N. Yamamura, M. Ishida, and T. Hori, "An improvement of performance of small-scaled wind power generating with permanent magnetic type synchronous generator," Proceedings of IEEE IECON'00, Vol. 2, pp. 1037–1043, October 2000.

Copyright © 2009 SciRes

Energy and Power Engineering, 2009, 81-84
doi:10.4236/epe.2009.12012 Published Online November 2009 (http://www.scirp.org/journal/epe)

Biomass Production of Poplar Plantation Ecosystem in Yangtze River Beach Land

Jianfeng ZHANG[1], Qixiang SUN[2,*], Jinxing ZHOU[2], Qihua SHAN[1], Lixun WU[3]
[1]*Institute of Subtropical Forestry, Chinese Academy of Forestry, Fuyang, China*
[2]*Institute of Forestry, CAF, Silvicultural Laboratory of SFA, Beijing, China*
[3]*Forestry Academy of Hunan, Changsha, China*
[*]*Author for corresponding, Email*: *sunqixiang@263.net*

Abstract: Currently, China is home to more than four million hectares of oil plants nationwide, and 154 kinds of energy trees could produce seeds containing more than 40 percent of oil, with total production of the seeds totaling five million tons. Another 57 million hectares of waste land are available and suitable for planting trees for the production of forest-based bioenergy, of which there is 630,000 hm^2 beach land in the middle and lower reaches of Yangtze River where is suited for poplar growing. In order to approach the potential of poplar biomass production, the test was conducted in the paper. The result indicated that in the poplar forest ecosystem the herbaceous biomass production was 15.554 t/hm^2. While biomass production for trees was 43.164 t/hm^2, totally in the poplar plantation ecosystem biomass production reached 58.718 t/hm^2. As well, poplars growing added incomes for local farmers.

Keywords: biomass production, poplar plantation, Yangtze River

1. Introduction

Based on abundant information from the National Bureau of Statistics and listed companies, in 2007, China's fuel ethanol output reached 1.6 million tons, of which 80% used corn as raw materials. Based on the proportion 1:3.3, more than four million tons of corn was consumed. It is estimated that China's annual fuel ethanol output will reach five million tons in 2010 and utilization rate of ethanol gasoline will be more than 50%. Moreover, corn-based ethanol has stopped expanding production capacity, as government policies have clearly restricted the development of grain-based ethanol. Therefore, developing non-grain ethanol has become an inevitable trend [1]. It is forecasted that China's biodiesel output will reach two million tons in 2010.

China's biological energy power generation has developed rapidly and the total installed capacity has reached 2.2 million kW, of which 1.7 million KW was from Bagasse co-generation and 500,000 KW was powered by agriculture and forestry wastes, methane, direct-burning of rubbish and landfill gas. Generally speaking, efforts made to develop biological energy are still limited, therefore, China's bioenergy has a huge potential for future development.

China has sufficient raw materials resources for production of biomass. Only the agricultural wastes can be converted into energy, which is equivalent to 500 million tons of standard coal and 350 million tons of crude oil (about 2.5 billion barrels).

There is 630,000 hm^2 beach land in the middle and lower reaches of Yangtze River, including island-type beach, the continent beach, the lake beach, etc. three kind of types. This is the extremely important natural resource in view of much more population and faster urban expansion there [2]. But because natural vicissitude, mainly the human factor disturbance, the beach land ecosystem is received the enormous destruction, cannot display the ecological function, the economic benefits and the social efficiency which it should have.

On the other hand, planting poplar tree in the beach, not only fully uses the natural resource, increases the incomes for local people, moreover the poplar tree also has the function of biomass production. Therefore, the development of poplar forest in the beach could improve the local ecological environment along the middle and lower reaches of Yangtze River, and promote regional socio-economic processing as well [3].

2. Experimental Location and Methods

2.1. Experimental Location and Natural Conditions

Experimental location lied at Dongting lake region in Yueyang, Hunan Province, among the north latitude

The research is funded by State Tenth Five-year Plan of Science & Technology Project (2006BAD03A15)

Copyright © 2009 SciRes

29º31′40″ and east longitude 112º51′34″. It is of the subtropics moist monsoon climate characteristic, much rainfall in the summer, while in the autumn much drought, in the winter & spring severely cold. Annually mean precipitation 1200.7~1414.6mm, yearly average relative humidity 80%. The annual mean temperature 16.5 ~ 17.0 ℃, accumulative temperature over 10 ℃ is 5254.1 ~ 5529.2 ℃, extreme lowest temperature -13.7 ℃, extreme highest temperature 39.3 ℃. Frost-free period 263.7 ~ 276.6d, yearly sunshine time 1644.3 ~ 1813.8h [4].

The observation point is located at Junshan district, the terrain is smooth, and its elevation equally is 31m. The soil layer fertility is higher, the vegetation is luxuriant. Dongting Lake's flood season appears usually in June-August. The flooding time yearly is 20 ~ 50d, the longest may reach 130d.

Poplar species mainly belong to Euro-American ones, the clones include: poplar 2KEN8 (*P. deltoides* ' 2KEN8 '), poplar 55/65 (*P. deltoides* ' 55/65 '), poplar NL-80121 (*P.* ' nanlin 80121 ') and so on. Experimental stands were planted in 2000, the density is 495/hm^2, spacing is 4m×5m, average DBH approximately 14cm, average tree height approximately 16m. Under the forest the herb coverage is 70-80%, the main species include: *Cynodon dactylon*, *Oenanthe Javanica*, *Ranunculus sieboldii*, *Leonurus Artemisia*, *Rumex Japonicus*, *Carex spp*, *Paederia scandens*, *Cirsium Japonicum*, *Erigeron annuus*, *Achyranthes aspera*, *Triarrhena Iutariori Paria* and so on.

2.2. Research Methods

The research on biomass production of poplar plantation ecosystem is through measuring firstly the biomass of trees including above- and underground parts according to the method of standard stand inventory, then for herb's biomass production is the alike.

3. Results and Analysis

3.1. Biomass Production of Poplar Trees

The measurement was done at 5-year poplar stand performed separately in December 2005 and November 2006. Firstly stand sample was chosen, then conducted inventory. According standard stock was selected. The indicators were shown at Table 1.

Table 1. Survey of poplar stocks

Measure date	DBH (cm)	Height (m)	Stem height (m)	Mean crown area (m^2)
December 2005	16.54	13.58	4.28	4.63
November 2006	17.54	14.87	4.22	4.67

Table 2. Dry biomass of poplar tree unit: g

items	Biomass(dry weight)
Stem	45 578.87
Branches	16 395.17
Leaves	1 307.13
Bark	8 275.78
Roots	13 487.21
Litter	2 155.44
Total	87 199.61

Table 3. Investigation of herbs in poplar stands in June

Species	Mean height (m)
Oenanthe javanica	62
Artemisia iavandulaefolia	56
Alternanthera philoxeroides	31
Carex spp.	35
Ranunculus sieboldii	27
Leonurus artemisia	48
Clinopodium gracile	24.7
Polygonum Iapathifolium	18
Rumex japonicus	43.5
Poa Faberi rendle	10
Clinopodium chinense	27
Achyranthes aspera	42.5
Cirsium japonicum	108.57
Erigeron annuus	14.6
Hemistepta iyratae	60
Clinopodium repens	50
Hemarthria altissima	5
Paederia scandens	51.67
Triarrhena Iutarioriparia	75
Galium aparine var．tenerum	10
Cynodon dactylon	42.5

In order to study the stock biomass production, different parts such as stem, root, branch, leaf were collected and measured. For underground one, survey area was 4 m×5m, i.e. nutrition area of the tree, roots were graded into several classes such as <lcm、1—5cm、5—10cm、>10cm according to root diameter. The results were given out in Table 2.

From Table 2 it was shown that the dry biomass of the average single standard stock was 87 199.61g. The density of the stand is 495/hm^2, therefore in this ecosystem biomass production of poplar trees is 43.16 t/hm^2.

Copyright © 2009 SciRes

Table 4. Investigation of herbs in poplar stands in October

Species	Mean height (m)
Leonurus artemisia	20
Polygonumi apathifolium	19
Alternanthera sessilis	10
Oenanthe decimhens	6
Viola betonicifolia	8
Achyranthes aspera.	18
Carex spp.	20
Cnidium monnieri	2
Rumex japonicus	4
Cynodon dactflon	16
Hemarthria altissima	7
Ranunculus sieboldii	3
Phragmites australis	40
Paederia scandens	4
Calystgia sepium	4

3.2. Biomass Production of Herbs

For herbs and litters biomass production the research method is the alike with trees. The survey was carried out in June and October, 2006. Since in June it was in flooding season, in October not, so that vegetation species and life stage were various. The survey results were shown as Table 3 and Table 4.

It indicated that the plant community in different season is varied from Table 3 and Table 4. Accordingly biomass production of herbs and litters should be the sum of the two inventories.

In the Yangtze River flood season, the understory herb growing in spring and summer all submerges submarine [5]. After the water draws back, the forest land basically did not have the vegetation growing. Hence the vegetation investigated after October all was newborn biomass. Therefore the biomass of herbs should be sums of the two investigations.

In June the herbaceous biomass investigation demonstrated that the understory herb biomass was 10.11t/ hm^2, the underground root system biomass occupies always about 40% of the aboveground one, i.e. 4.044 t/ hm^2. Hence in June the herbaceous biomass production amounted to 14.154t/ hm^2.

In October the herbaceous growth situation sees Table 4. Compared with Table 3, it is discovered that the amount of species reduced; moreover the average height obviously was lower than before. Through 12 samples which area covers 1m×1m investigation, the herbaceous biomass demonstrated that the understory herb biomass was 1.00t/ hm^2. As discussed above, the underground root system biomass was 0.40 t/ hm^2. In October the herbaceous biomass production amounted to 1.40 t/ hm^2.

Generally spoken, in the poplar forest ecosystem the herbaceous biomass production is 15.55 t/hm^2. While biomass production for trees is 43.16 t/hm^2, totally in the poplar plantation ecosystem biomass production reached 58.72 t/hm^2, of which trees accounting for 73.51% of the total, and herbs taking 26.49%.

4. Conclusions and Discussions

China has been anxious to boost its use of alternative energy in recent years as its heavy reliance on burning coal to meet energy needs has caused serious environmental problems. The government plans to reduce the percentage of coal in consumption to 66.1 percent by 2010 from 69.1 percent in 2005, while improve renewable energy usage, excluding hydropower, to 0.4 percent from 0.1 percent.

The country plans to produce more than six million tons of forest-based biodiesel and will increase the installed capacity of renewable, biomass-based power generation by more than 15 million kilowatts by 2020. The potential of the country's forest-based bioenergy would thus be equivalent to 200 million tons of coal, the utilization of which would reduce the consumption of fossil energy by 10 percent. Ultimately, biomass can be used in carbon-negative energy systems, and reduce carbon dioxide emissions even further.

In this research, through above mentioned measurement and analysis, it was shown that in the 5-year poplar forest ecosystem biomass production reached 58.72 t/hm^2, of which trees accounted for 73.51% of the total, and herbs took 26.49%. This fact indicates that the beach poplar forest has the very big biomass production and carbon sequestration function.

According to the State Forestry Administration, China will establish 13.33 million hectares of forests by 2020 to produce liquid and solid biofuels for power generation and transport. The hectarage will rise from a planned 833,33 hectares in 2010 and provide enough biomass to produce over 6 million tonnes of biodiesel a year and power generators with capacity of 15 gigawatts. The energy forests will contribute massively to China's already successfull attempts aimed at reducing desertification.

In view of the current situation, the research is significant.

REFERENCES

[1] J. F. Zhang, J. M. Jiang, and Q. H. Shan, "Research on the black locust (Robinia pseudoacacia) forest as biomass energy resources in Yellow River delta region," In: the Proceedings of Asia-Pacific Power and Energy Engineering Conference, 2009.

[2] Z. H. Jiang, "Selected papers on snail control and schistosomiasis prevention through forestry ecological engineering (in Chinese)," China Forestry Publishing House, Beijing, pp. 105–164, 1995.

[3] Q. X. Sun, Z. H. Peng, and Z. M. Kang, "Research on species selection based on sites in beach land," Journal of Anhui Agricultural College (in Chinese), Vol. 25, No. 1, pp. 18–22, 1998.

[4] L. X. Wu, Z. H. Cheng, and S. F. Xu, "Research on the relation between afforestation in beach land with snail control and schistosomiasis prevention," Hunan Forestry Science and Technology (in Chinese), Vol. 23 No. 1, pp. 10–18, 1996.

[5] Y. Wang, "Research on carbon & water flux and carbon sequestration of poplar forest ecosystem in middle and lower reaches of Yangtze River (in Chinese)," Ph. D. Thesis, Chinese Academy of Forestry, Beijing, pp. 5–120, 2006.

Copyright © 2009 SciRes

Energy and Power Engineering, 2009, 85-89
doi:10.4236/epe.2009.12013 Published Online November 2009 (http://www.scirp.org/journal/epe)

Heat Transfer by Natural Convection from a Vertical and Horizontal Surfaces Using Vertical Fins

H. R GOSHAYESHI[1], F. AMPOFO[2]
[1]*Department of Mechanical Engineering, Azad University of Mashhad (IAUM), Mashhad, Iran*
[2]*Department of Mechanical Engineering, School of Engineering System and Design, London South Bank University, London, UK*

Abstract: Natural convective heat transfer from a heated horizontal and vertical surfaces directly exposed into air which vertical fins, attached to a surface, project vertically downwards has been numerically studied. It has been assumed that the fins are everywhere at the temperature of the surface. The governing equations, written in dimensionless form, have been solved using the finite element procedure. The results show that vertical plate with vertical fins gives the best performance for natural cooling.

Keywords: natural convection, horizontal and vertical plate, fins, Nusselt number

1. Introduction

The vertical and horizontal plate configurations are the most common geometry for a naturally cooled heat sink. The configuration has been studied by number of researchers. The most commonly used predictive equation for convection was derived by Barcohen, S. & Rohsenow W [1] and Kruaus, A. D & Bar-Dohen [2]. This situation has been considered for free convective heat transfer from a heated horizontal and vertical surface directly exposed to air with a free surface to vertical fins attached to surface that project vertically downward into the air has been studied by Smith, H. [3] and Magyaro, L and pep, H [4]. Unlike the well-study vertical/vertical configuration very few research papers have been written on the horizontal/up configuration. The most comprehensive experimental interrogation was performed by Fuji, V. & Magata, B, [5] but they did not derive an accurate equation which matched the full range of their experimental data. This work compares horizontal plate heat sinks with vertical plate heat sink for natural cooling application. As shown in Figure 1, three different configurations will be discussed: 1) vertical plate with vertical fins 2) horizontal plate with fins facing up 3) vertical pate with horizontal fins. Figure 1 gives some quick guideline on the merits of the different configurations.

2 Governing Equations and Solution Procedures

It has been assumed that flow is steady, laminar and two-dimensional and that the air properties are constant except for the density change with temperature which gives rise to the buoyancy forces, this being treated using the goussinesq approach. The following dimensionless variables have then been defined:

$$\varphi = \varphi' / \alpha, \omega = \omega' H'^2 / \alpha, x = x' / H', y = y' / H', T = (T' - T'c) / (T'_H - T'_C) \tag{1}$$

where T is the temperature. T_H is the temperature of the hot wall and T_C is the temperature of the fin. The prime (') denotes a dimensional quality .

In terms of these dimensionless variables, the governing equations are:

$$\frac{\partial^2 \varphi}{\partial x^2} + \frac{\partial^2 \varphi}{\partial y^2} = -\omega \tag{2}$$

$$\frac{\partial \varphi}{\partial y}\frac{\partial \omega}{\partial x} - \frac{\partial \varphi}{\partial x}\frac{\partial \omega}{\partial y} - \Pr\left(\frac{\partial^2 \omega}{\partial x^2} + \frac{\partial^2 \omega}{\partial y^2}\right) = Ra\frac{\partial T}{\partial x} \tag{3}$$

$$\frac{\partial \varphi}{\partial y}\frac{\partial T}{\partial x} - \frac{\partial \varphi}{\partial x}\frac{\partial T}{\partial y} - \left(\frac{\partial^2 T}{\partial x^2} + \frac{\partial^2 T}{\partial y^2}\right) = 0 \tag{4}$$

Here Ra is the Rayleigh number based on the height,

$$Ra = \frac{\beta g (T'_H - T'_C) H'^3}{\nu \alpha} \tag{5}$$

The above dimensionless equations, subject to the boundary conditions, have been solved using the fin element procedure. The mean heat transfer rate across

Copyright © 2009 SciRes

the enclosure has here been expressed in terms of a mean Nusselt number, Nu, based on the height, H', the mean heat transfer rate from the lower surface, q'_m and on and the overall temperature difference, $(T'_{High} - T'_{Low})$.

3. Results and Discussion

The computer program shows that $h_{convection}$ for horizontal backplane fin channel is lower than $h_{convection}$ for vertical/vertical fin channels. For a given heat sink volume, there exits an optimal fin spacing. The optimum value occurs when two trends are balanced.

If the fins are closely spaced, the heat transfer coefficient (h) is lower because mixing of the boundary layer occurs (the fills up with warm air). The graph if Figure 3 clearly shows that the heat transfer coefficient decreases as the gap between fins decreases. However, if the fins are closely spaced, there is also more dissipating surface area (more fins for a given volume). The additional surface area can counteract the reduced heat transfer coefficient. This can be seen by examining the graph of total wattage dissipated in Figure 4. For the 150 mm X 150 mm vertical/vertical heat sink shown in the graph, the spacing of 7.5 mm provided the optimal combination of heat transfer coefficient and dissipating surface area.

Figure 4, presented above, shows the wattage dissipated for an entire 150 mm X 150 mm heat sink, including end fins and radiation (emissivity = 0.1, typical of a bare extruded surface). When a horizontal baseplate heat sink is sinks in not square, there will be two possible orientations for the fin channel. As shown in Figure 5, the fins should be oriented to provide the shortest channel depth. For a baseplate which 100 mm X 50 mm, the proper channel orientation will provide 15% better performance.

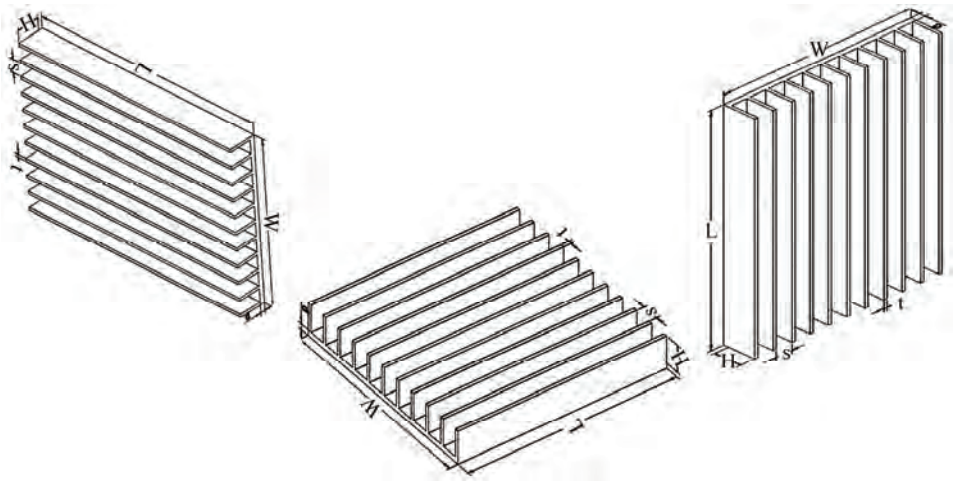

Figure 1. Fin configurations for natural (Free) cooling

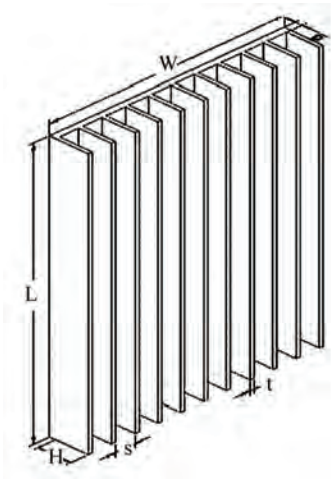

Figure 2. Primary air flow pattern for the vertical/vertical configuration

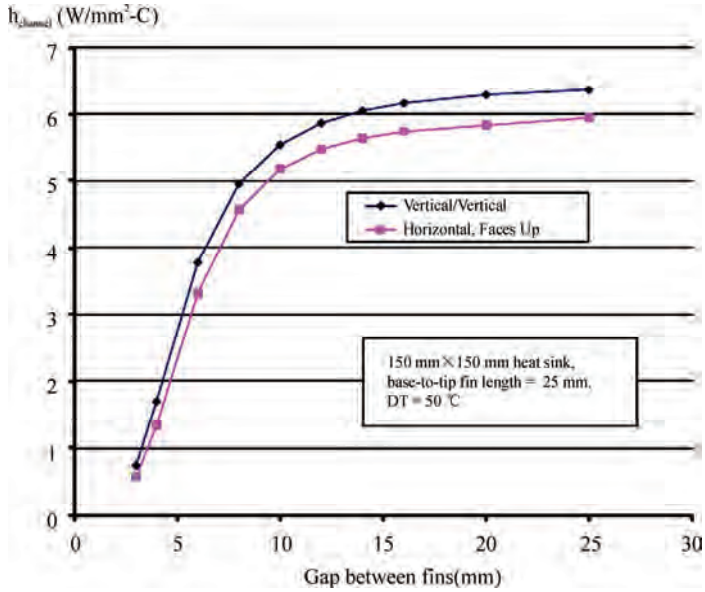

Figure 3. h $_{channel}$ for vertical and horizontal 150 mm * 150mm heat sinks

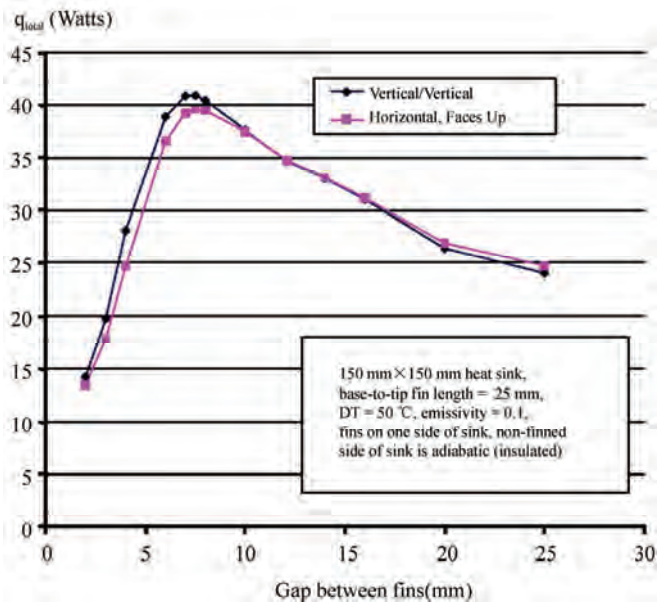

Figure 4. q $_{channel}$ for vertical and horizontal 150 mm X 150mm heat sinks

4. Conclusions

The primary airflow pattern for the vertical/vertical configuration is shown in Figure 6. Air enters nears the bottom of the fin channels and there will be some air flow from the fin tips. Air is heated within the fin channels and exit at the top. With this air flow path, the vertical/ configuration delivers the best performance for free or natural cooling. The final heat sink configuration to be discussed is the vertical baseplate/horizontal fin channel geometry shown in Figure 6.

Figure 7 shows a comparison between vertical/vertical heat sink and a vertical/horizontal heat sink.

As the Figure 7 illustrates, vertical fin channels are better. However it should be mentioned that the vertical/ horizontal sink is certainly better than a flat wall. With a fin length of 25 mm the vertical/horizontal heat sink provides roughly twice the wattage dissipated, an appreciable improvement. Also, the fins allow for an additional conduction where it is logical to use vertical/horizontal heat sinks. Figures 8 to 10 show the fins configuration by Fluent.

Copyright © 2009 SciRes

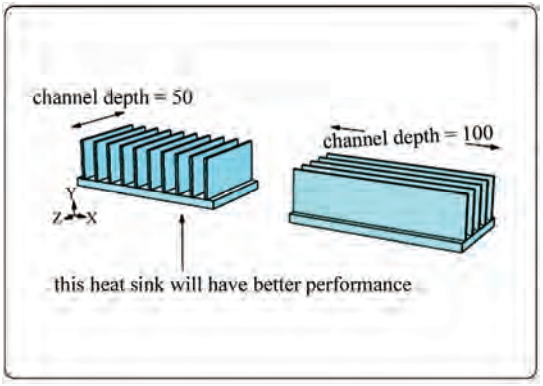

Figure 5. Proper fin channel orientation for horizontal heat sink

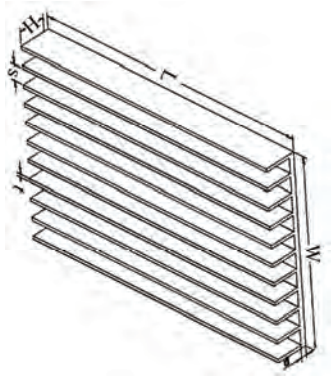

Figure 6. Vertical plate/horizontal fin configuration

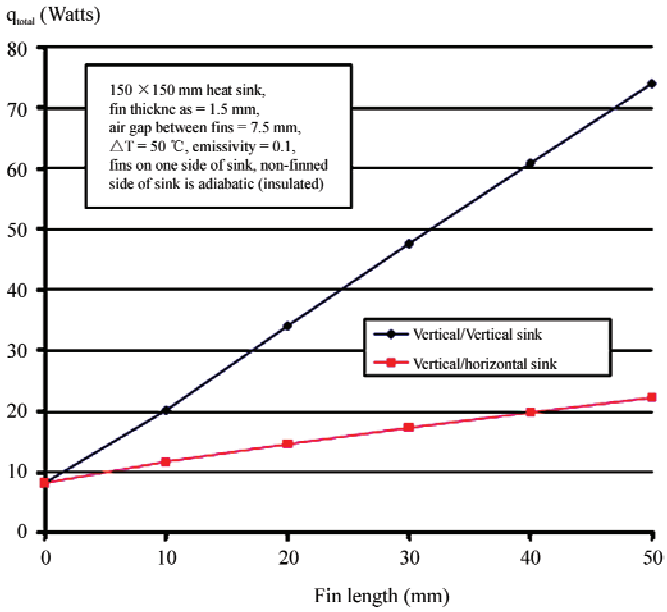

Figure 7. Comparing vertical/vertical and vertical/horizontal heat sinks

The results of the present study indicate that:

- Vertical plate with vertical fins gives the best performance for natural cooling.
- The fin spacing at which the maximum mean heat transfer rate occurs decreases with increasing Rayleigh number varying approximately as $1/Ra^{0.25}$.
- As the fin spacing is decreased, the mean heat transfer rate, provided that the Rayleigh number is high enough for convective motion to occur, initially rises before passing through a maximum and then falling to the pure conduction value.

5. Nomenclature

G' = distance between bottom of fin and the bottom wall.

$G = G'/W'$

H' = depth of liquid .

$H = H'/W'$

Nu = Nusselt number based on H'

Ra= Rayleigh number based on H'

T' = temperature

T'_C = temperature of top surface

T'_H = temperature of bottom surface

T = dimensionless temperature

W' = half-gap between fins

$W = W'/H'$

x = horizontal coordinate

x' = dimensionless horizontal coordinate

y' = vertical coordinate

y = dimensionless vertical coordinate

φ' = stream function

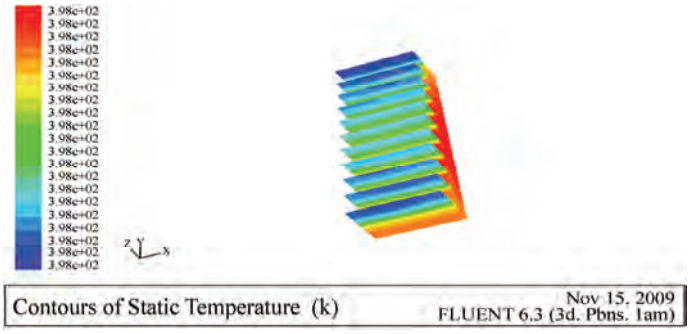

Figure 8: Fin configurations for vertical pate with horizontal fins by Fluent

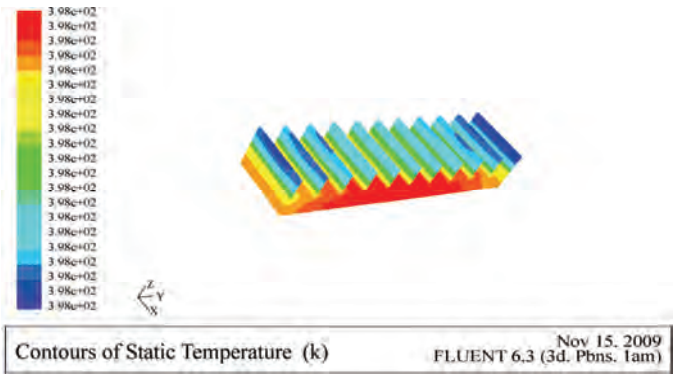

Figure 9: Fin configurations for horizontal plate with fins facing up by Fluent

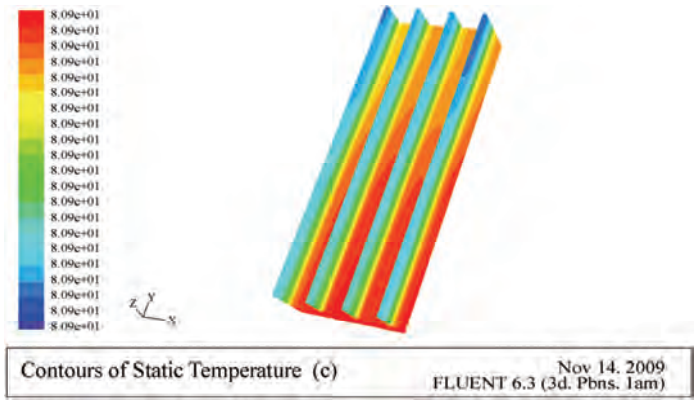

Figure 10: Fin configurations for vertical pate with horizontal fins by Fluent

φ = dimensionless stream function

ω' or u= Velocity

ω = dimensionless velocity

REFERENCES

[1] S. Barcohen and W. Rohsenow, "Thermal optimum spacing of vertical natural convection cooled parallel plates," Journal of Heat Treansfer, Vol. 106, pp. 116–123, 1984.

[2] A. D. Kruaus and Bar-Dohen, "A design and analysis of heat sink," John Wiley and Sons, New York, pp. 305–320, 1995.

[3] H. Smith, "Combined heat and mass transfer effect in free convection," Electricity Research Laboratories, Leatherhead, Surrey, February 2006.

[4] L. Magyaro and H. Pep, "Free convection flow pass an infinte vertical plate," ASME Modelling B, Vol. 72, No. 3, 2007

[5] V. Fuji and B. Magata, "MHD unsteady free convection flow through a prous media, Energy Research, Vol. 7, pp. 89–109, 2004.

Copyright © 2009 SciRes

Energy and Power Engineering, 2009, 90-93
doi:10.4236/epe.2009.12014 Published Online November 2009 (http://www.scirp.org/journal/epe)

Modeling of the Unburned Carbon in Fly Ash

Weiping YAN, Jun LI
Key Laboratory of Condition Monitoring and Control for Power Plant Equipment of Ministry of Education, North China Electric Power University, Baoding, China
Email: *lj*2110271@163.*com*

Abstract: Numerical simulation of the content of unburned carbon in fly ash on the 300MW tangentially pulverized coal fired boiler is performed by the numerical simulation software COALFIRE, which is based on international advanced TASCFLOW software platform. Firstly, take the result of calculation of number value as the sample, and then set up the support vector machine model of unburned carbon content on the boiler. The relative error between the predicted output and measured value is 0.00186%, which proves the modeling is good for the unburned carbon in fly ash predict.

Keywords: numerical simulation, unburned carbon content, support vector machine

1. Introduction

The unburned carbon in fly ash is the important data which reflects the combustion efficiency of the coal fired boiler in thermal power plant, but the content of unburned carbon in fly ash of the coal fired boiler is influenced by so many kinds of factors which are difficult to be measured in real time [1–3].

At present, there are lots of the researches about the monitor of the content of unburned carbon in fly ash in real time in domestic and international. Most of them are concentrated on the technology of the measurement equipment and software [4–6]. The equipment of the content of unburned carbon in fly ash has many problems, such as the block of sample tube, complicated extra equipment, many influence factors about the precision of the measurement, high cost of the fabrication and the high request of maintain, etc. Moreover, the traditional soft measurement technology is almost all used the artificial neural network method to build the model, because the study algorithm of the neural network adopts the experience risk and minimizes the principle, lacks of quantitative analysis and theory result with complete mechanism. At the same time, for the reason of it is limited in quantity to survey samples, it will cause the question of overstudying and the ability of generalization badly, etc. Therefore, there is very great limitation exist in the measurement of the content of unburned carbon in fly ash based on the artificial neural.

As a kind of new statistics learning method, support the vector machine (Support Vector Machine, SVM) uses the principle of the structure risk minimize (SRM), which solved the problem of generalization in the theory of machine studying effectively. The goal function of the structure risk minimize (SRM) has suppressed the phenomenon of owed and passed studying effectively, and it can get the good ability of generalization. The algorithm is turned into a secondary programming and gets optimum point of global. It has solved local minimum problem in the neural network. Its topological structure only relates to support the vector and has reduced the calculating amount. The computational speed is fast, which is suitable for online application. The method is suited to study in little sample. Support vector machine has already become the important research means between the pattern-recognition and the data excavate field at present [7,8].

In the limited sample studying system [9], because it has the wild value in the sample, the statistics study theory of V. N. Vapnik thinks it has caused the reducing of minimum guaranteed risk value. It also caused low category precision in the category questions. Regression will have the phenomenon of “over fitted” or “over trained”, and the ability of generalization of the study drops greatly too. On the condition of training samples is limited, the selection of training collection influences the ability of generalization of study machine obviously. That is to say, the ability of generalization not only relates to the study algorithm, but also relates to the selection of training collection. When choosing the model sample, the existing method always uses the unburned carbon in fly ash of the boiler hot condition as training the sample [4–6]. Because the combustion operating mode in the pulverized coal fired boiler is very complicated, involving the course in many aspects of burning, flowing, conducting heat etc, receives such as the influence in proportion, nature of the coal, density and fineness of coal flow, wind velocity, load of boiler, etc. Additionally, these factors often influence each other and interweave each other, which have

Copyright © 2009 SciRes

increased the complexity of the combustion process even more, thus it causes changeable of the unburned carbon in fly ash. Adding the restriction of the on site condition, it is more difficult to get the intact sample of unburned carbon in fly ash from the operating mode of the boiler.

Using the method of numerical simulation to calculate the content of unburned carbon in fly ash of the boiler has satisfied accuracy, whose variation tendency predicted can meet the need of combustion adjustment for operation actually. However, its amount of calculation will consume much time. It will consume a large amount of time even used for optimize design off line. It makes it difficult to use in monitoring and optimizing online directly.

To the question of appealing, this paper adopts the coal-fired pulverized boiler furnace numerical simulation software COALFIRE, to calculate the content of unburned carbon in fly ash off-line under many kinds of burning operating modes of the boiler. Regard the result of calculation of number value in advance as the training sample of the model of vector supporting machine. It makes the model not only has the precision of the numerical simulation, but also can applies the result in the online system of content of unburned carbon in fly ash monitoring and optimizing.

2. Pre-Numerical Calculation

2.1. Object of Simulation

Object of the simulation is the boiler of DG1025/18.2-Ⅳ, which was made by the Don Fang boiler factory in China.

2.2. The Method of Numerical Simulation

It chooses the calculate area between the bottom of the furnace hopper and the angle of flame diverter on the top of the furnace. It takes the width of the furnace as the X direction, the depth of the furnace as the Y direction, the height of furnace as the Z direction. Divide 160 unit areas, 508896 mesh altogether. The numerical simulation adopts the three-dimensional stable state to calculate. Adopt standard k–ε equation model to simulate the turbulent gaseous phase of flow; use the particle track model at random to solve the solid particle phase problem; adopt P1 radiate models to solve the radiation Conduct heat; adopt the single step response model to the release of the coal pulverized volatile matter; have adopted the motive force model of spreading to the burning of the coke; adopt the PDF model of conservation scalar to simulate the non-premixed combustion and the non-cross mesh SIMPLE method to solve the flowing field of the gaseous phase. Having identified the convergence by the residual, all of the relative error of the calculating amounts (for instance, the relative error that u, v, w, ε, etc.) must be smaller than the value of 1.0×10^{-4}. Take it as the convergence criterion.

2.3. The Operating Mode of Calculation

Consider the change of unburned carbon in fly ash with the change of the nature of coal, coal fineness, boiler load, distribution of secondary air, withdrawal or input of tertiary air, etc.

2.4. Comparison and Analysis of Results of the Unburned Carbon in Fly Ash

The unburned carbon content in fly ash of outlet of furnace can be received through the numerical simulation. The actual measurement value of unburned carbon also can get by the online monitoring system of carbon content of unburned carbon in fly ash which located in front of the air pre-heater at the same time. The result of calculating simulation and hot surveying value of unburned carbon content in fly ash are as Figure 1 shows. Figure 1 shows that the actual measurement value is higher than the result of numerical simulation, the greatest relative error is 0.07% after revising and the minimum relative error is 0.02%. Considering the error of the surveying value, the result of calculation of number value and hot operating mode surveying value are identical better.

3. The Model of Unburned Carbon in Fly Ash Based on Support Vector Machine

3.1. The Introduce of Support Vector Regression

The basic problem of regression is to find a function $f \in F$ (F—Union of function) and make the expected risk function as follow minimum [10–15].

3.2. Unburned Carbon Content in Fly Ash Model Based on Support Vector Machine

- The choice of input and output parameter of the model

According to the condition of the pre-numerical simulation in advance, adopt the flowing as parameter of inputting, include the boiler load, rate of powder quality,

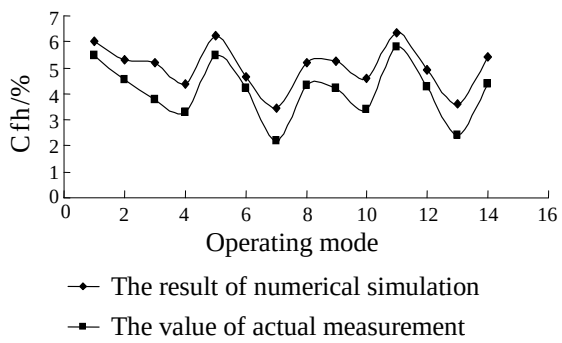

Figure 1. The unburned carbon content under various operating conditions

fineness of pulverized coal, wind velocity of secondary air and tertiary air, tilt angle of burner, net calorific power, volatile, ash content and moisture content of coal. The amount of adjustable parameter is 22. Regard carbon content of flying ash as the parameter of outputting, and use the supporting vector machine to set up the carbon content characteristic model of flying ash.

- Selecting of kernel function

Selecting of kernel function influences the regression analysis of support vector machine obviously, but does not have a ripe theory about it at present yet [16]. The paper selected the radial kernel function [17].

- Constitution of sample union and the selecting of algorithm parameter

The sample union is structured by the result of pre-calculation in different operating condition of boiler. Taking the result of 1~2、4~8、10~14 operating condition as the training sample, the result of 3、9 operates condition as test sample. Adopting the radial kernel function to regression analysis, the precision of model ε is 0.0001.

- The result and the analysis

The trained result shows as follows: the relative error of the output of predicting is 0.00186%. The predicting output and the relative error of the test sample of operating condition 3 and 9 show as Table 1. It is indicating that the output error of support vector machine model is very small, and its identical degree of data is quite good. It is proved that this model has gotten the correct corresponding behavior between the input and output. This proves that the modeling of the unburned carbon in fly ash based on numerical simulation and support vector machine algorithm on the 300MW tangentially pulverized coal fired boiler is successful.

4. Conclusions

The unburned carbon content in fly ash of tangentially pulverized coal is influenced by so many factors. The factors also influence each other. Therefore, it is difficult to predict and control the unburned carbon content in fly ash. By the pre-calculating, the precision result of unburned carbon content in fly ash can be gotten. After it is fixed by the practice measurement in different boiler operating condition, it can be taken as the training test sample of the support vector machine model. The simulating result shows that the predict result and the result of practice measurement of unburned carbon content in fly ash of boiler concordances are better. It provides the effective method for applying the numerical simulation result for the online monitor of boiler burn state parameter, whose character is to get accurate result but consume enormous time during computational process. If combining the overall situation seeking excellent algorithm, it can make the boiler reach optimum operating mode, and improve security and economy of the boiler.

Table 1. The comparison between the predict value of support vector machine model and pre-calculation value of unburned carbon content in fly ash

Operating condition	The result of Numerical simulation (%)	The result of model of support vector machine (%)	The absolute value of relative error (%)
3	5.18	5.152	0.541
9	5.23	5.214	0.306

REFERENCES

[1] M. H. Fan and R. C. Brown, "Precision and accuracy of photo acoustic measurements of unburned carbon in fly ash [J]," Fuel, Vol. 80, No. 11, pp. 1545–1554, 2001.

[2] K. Styszko-Grochowiak, J. Golas, H. Jankowski, *et al.*, "Characterization of the coal fly ash for the purpose of improvement of industrial on-line measurement of unburned carbon content [J]," Fuel, Vol. 83, No. 13, pp. 1847–1853, 2004.

[3] A. K. Ouazzane, J. L. Castagner, A. R. Jones, *et a1.*, "Design of an optical instrument to measure the carbon content of fly ash [J]," Fuel, Vol. 81, No. 15, pp. 1907–1911, 2002.

[4] H. Zhou, H. B. Zhu, T. H. Zeng, *et a1.*, "Artificial neural network modelling on the unburned carbon in fly ash from utility boilers [J]," Proceedings of the CSEE, Vol. 22, No. 6, pp. 96–100, 2002. (in Chinese)

[5] X. T. Fang and N. Y. Ye, "A system forpredicting the anburned carbon of the fly ash from utility boilers based on BP artificial neural netwoks [J]," Jouunal of Huazhong Uruversity of Science & Technology, Nature Science Edition, Vol. 31, No. 12, pp. 75–77, 2003. (in Chinese)

[6] M. Sebastia,I. F. dez Olmo, and Angel Irabien, "Neural network prediction of unconfined compressive strength of coal fly ash cement mixtures [J]," Cement and Concrete Research, Vol. 33, No. 8, pp. 137–145, 2003.

[7] G. Y. Zhang and J. Zhang, "Fuzzy SVM-based multilevel binary tree classifier for fault diagnosis of hydroturbine speed regulating system [J]," Proceedings of the CSEE, Vol. 25, No. 8, pp. 100–104, 2005. (in Chinese)

[8] Y. C. Li, T. J. Fang, and E. K. Yu, "Study of support vector machines for short-term load predicting [J]," Proceedings of the CSEE, Vol. 23, No. 6, pp. 55–59, 2003. (in Chinese)

[9] Y. Wang, Z. H. Zhou, and A. Y. Zhou, "The apply of machine study [M]," The Publish House of Tsinghua University, Beijing, pp. 1–27, 2006.

[10] A. Smola and B. Scholkopf, "A tutorialon support vector regression [R]," Royal Holoway College, London,1998.

[11] V. N. Vapnik, "The nature of statistical learning theory [M]," Springer, New York, 1999.

[12] G. Z. Li, M. Wang, H. J. Zeng (translate), N. Cristianini,

J. Shawe-Taylor (write), "Introduction of support vector [M]," The Publish House of Electric Industry, Beijing, 2004.

[13] X. G. Zhang (translate), Vapnik (write), "Theory of statistic study [M]," The Publish House of Electric Industry, Beijing, 2004.

[14] X. G. Zhang, "Introduction to statistical learning theory and support vector machines [J]," ACTA Automatica Sinica, Vol. 26, No. 1, pp. 32–43, 2000.

[15] X. D. Wang and J. Q. Wang, "A survey on support vector machine traing and testing algorithms [J]," Computer Engineering and Applications, Vol. 40, No. 13, pp. 75–78, 2000.

[16] S. S. Keerthi and C. J. Lin, "A symptotic behaviors of support v machines with Gaussian kernel [J]," Neural Computation, pp. 1667–1689, 2003.

[17] C. L. Wang and H. Zhou, *et a1*., "Support vector machine modeling on the unburned carbon in fly ash [J]," Proceedings of the CSEE, Vol. 20, No. 25, pp. 72–76, 2005. (in Chinese)

Copyright © 2009 SciRes

Energy and Power Engineering, 2009, 94-99
doi:10.4236/epe.2009.12015 Published Online November 2009 (http://www.scirp.org/journal/epe)

A New Multi-Method Combination Forecasting Model for ESDD Predicting

Haiyan SHUAI, Qingwu GONG
[1]*School of Electrical Engineering, Wuhan Technical College of Communications, Wuhan University, Wuhan, China*
[2]*School of Electrical Engineering, Wuhan University, Wuhan, China*
Email: *wdshy@126.com, whdxgqw@163.com*

Abstract: Equal Salt Deposit Density (ESDD) is a main factor to classify contamination severity and draw pollution distribution map. The precise ESDD forecasting plays an important role in the safety, economy and reliability of power system. To cope with the problems existing in the ESDD predicting by multivariate linear regression (MLR), back propagation (BP) neural network and least squares support vector machines (LSSVM), a nonlinear combination forecasting model based on wavelet neural network (WNN) for ESDD is proposed. The model is a WNN with three layers, whose input layer has three neurons and output layer has one neuron, namely, regarding the ESDD forecasting results of MLR, BP and LSSVM as the inputs of the model and the observed value as the output. In the interest of better reflection of the influence of each single forecasting model on ESDD and increase of the accuracy of ESDD prediction, Morlet wavelet is used to construct WNN, error backpropagation algorithm is adopted to train the network and genetic algorithm is used to determine the initials of the parameters. Simulation results show that the accuracy of the proposed combination ESDD forecasting model is higher than that of any single model and that of traditional linear combination forecasting (LCF) model. The model provides a new feasible way to increase the accuracy of pollution distribution map of power network.

Keywords: equal salt deposit density, multivariate linear regression, BP neural network, least squares support vector machines, combination forecasting, wavelet neural network

1. Introduction

Exposed to dirty environment, surfaces of insulators will be polluted. After being wetted, the polluted layers will deduce insulators' insulation capability which often invites pollution flashover. According to the operation experiences of power sectors, pollution flashover is one of the main factors causing power accidents. In recent years [1,2], there have happened several large area pollution flashovers in some locals or the whole country, which resulted in large area power blackout. Among all the causes resulting in pollution flashover, the lag and the inaccuracy of pollution distribution map of power network is a primary one. Equal Salt Deposit Density (ESDD) is the equivalent amount of NaCl that would yield the same conductivity at complete dilution [3], which is the dominant factor to classify contamination severity and draw pollution distribution map. At present, the methods of ESDD forecasting are mainly traditional multivariate linear regression (MLR) technique [4,5], back propagation (BP) neural network [6,7], and least squares support vector machines (LSSVM) [8,9]. Combination forecasting integrates the useful information of all single forecasting models and generally considers each forecasting result; hence it can more systemically and comprehensively reflect the changes of an object than a single model does. J. M. Bates and C. J. W. Granger proved the combination of two or more than two agonic single forecasting models can produce the result better than that of each single model, which showed combination forecasting method can increase prediction accuracy [10].

To improve ESDD forecasting accuracy, a nonlinear combination forecasting model based on wavelet neural network (WNN) for ESDD is proposed. The model is a WNN with three layers, whose inputs are the forecasting results of the three ESDD forecasting models mentioned above, i.e., MLR, BP and LSSVM, and outputs are the observed values of ESDD. For the sake of better reflection of the influence of each single forecasting model on ESDD and increase of the accuracy of ESDD prediction, Morlet wavelet is used to construct WNN and error backpropagation algorithm is adopted to train the network. Simulation results show that the accuracy of the proposed combination ESDD forecasting model is higher than that of any single model and also higher than that of

Copyright © 2009 SciRes

traditional linear combined forecasting (LCF) model. The model provides a new doable way to boost the precision of pollution distribution map of power network.

2. Brief Introductions of MLR, BP, LSSVM, and LCF

2.1. MLR Model

If y is a random variable predicted through $x_1, x_2, \cdots, x_p$ and there is a linear relationship between them, then a p-variable linear regression equation can be constructed as follow [11]:

$$y = \beta_0 + \beta_1 x_1 + \cdots + \beta_p x_p + \varepsilon \tag{1}$$

where p is the number of independent variables.

Considering the n groups of data observed are as followings respectively:

$$(x_{i1}, x_{i2}, \cdots, x_{ip}; y_i) \quad i = 1, 2, \cdots, n$$

Put $(x_{i1}, x_{i2}, \cdots, x_{ip}; y_i)$ $i = 1, 2, \cdots, n$ into (1), one can get

$$\begin{cases} y_1 = \beta_0 + \beta_1 x_{11} + \beta_2 x_{12} + \cdots + \beta_p x_{1p} + \varepsilon_1 \\ y_2 = \beta_0 + \beta_1 x_{21} + \beta_2 x_{22} + \cdots + \beta_p x_{2p} + \varepsilon_2 \\ \vdots \\ y_n = \beta_0 + \beta_1 x_{n1} + \beta_2 x_{n2} + \cdots + \beta_p x_{np} + \varepsilon_n \end{cases} \tag{2}$$

where $\beta_0, \beta_1, \cdots, and\ \beta_p$ are the $(p+1)$ parameters being estimated, called overall regression parameters; $\varepsilon_1, \varepsilon_2, \cdots, and\ \varepsilon_n$ are random errors independent with each other, and $\varepsilon_i \sim N(0, \sigma^2)$ .The task of multivariable linear regression is to solve the following three problems according to (2).

1) Determine $\hat{\beta}_0, \hat{\beta}_1, \cdots, and\ \hat{\beta}_p$ and the regression equation.

2) Carry out significant test to the regression equation. If the equation is representative, it is significant and can be used; otherwise, it can not be adopted.

3) Use the regression equation to predict or control the dependent variable under significant condition.

2.2. BP Model

BP [6,7] is a kind of feed forward neural network. Supposing a BP network has m layers, and each layer has several neurons. The neuron j of layer k has such an input-output relationship being described as:

$$x_j^k = f_j^{(k)}\left[\sum_{i=1}^{n_{k-1}} \omega_{ij}^{(k)} x_i^{(k-1)} - b_j^{(k)}\right] \tag{3}$$
$$(j = 1, 2, \cdots, n_k; k = 1, 2, \cdots, m)$$

where $\omega_{ij}^{(k)}$ is the connection weight between neuron i of layer $(k-1)$ and neuron j of layer k; $b_j^{(k)}$ is the threshold of neuron j; the activation function $f_j^{(k)}$ is a sigmoidal function, i.e., $f_j^{(k)}(x) = \dfrac{1}{(1+\exp(-x))}$; and n_k is the number of neurons of layer k.

2.3. LSSVM Model

LSSVM [12,13] is described as following:

Considering a given training set of m data points $\{x_k, y_k\}_{k=1}^m$ where $x_k \in R^n$ is the kth input vector and $y_k \in R$ is the kth output. In the feature space SVM models take the form:

$$y(x) = \boldsymbol{\omega}^T \varphi(x) + b \tag{4}$$

where the nonlinear mapping $\varphi(\cdot)$ maps the input data into a higher dimension feature space. The term b is a bias term. In least squares support vector machines for function estimation the following optimization problem is formulated:

$$\begin{aligned} &\min_{\omega, b, e} \mathbf{J}(\boldsymbol{\omega}, e) = \frac{1}{2}\boldsymbol{\omega}^T\boldsymbol{\omega} + \frac{1}{2}\gamma\sum_{i=1}^m e_k^{\ 2} \\ &s.t. \quad y_k = \boldsymbol{\omega}^T \varphi(\mathbf{x}_k) + b + e_k \quad k = 1, ..., m \end{aligned} \tag{5}$$

where γ is a positive real constant and should be considered as a tuning parameter in the algorithm.

The Lagrangian is given by

$$\mathbf{L}(\boldsymbol{\omega}, b, e, \alpha) = \mathbf{J}(\boldsymbol{\omega}, e) - \sum_{k=1}^m \alpha_k \left\{\omega^T \varphi(\mathbf{x}_k) + b + e_k - y_k\right\} \tag{6}$$

where α_k are Lagrange multipliers, which can be either positive or negative due to the equality constraints as from the Kuhn-Tucker conditions.

The conditions for optimality are

$$\begin{cases} \dfrac{\partial \mathbf{L}}{\partial b} = 0 \to \sum_{k=1}^m \alpha_k = 0 \\ \dfrac{\partial \mathbf{L}}{\partial e_k} = 0 \to \alpha_k = \gamma e_k \qquad k = 1, 2, 3..., m \\ \dfrac{\partial \mathbf{L}}{\partial \alpha_k} = 0 \to \boldsymbol{\omega}^T \varphi(\mathbf{x}_k) + b + e_k - y_k = 0 \quad k = 1, 2, 3, ...m \\ \dfrac{\partial \mathbf{L}}{\partial \boldsymbol{\omega}} = 0 \to \omega = \sum_{i=1}^m \alpha_k \varphi(\mathbf{x}_k) \end{cases} \tag{7}$$

After elimination of ω and e , one can get

$$\begin{bmatrix} 0 & \mathbf{y}^T \\ \mathbf{y} & \mathbf{Z}\mathbf{Z}^T + \gamma^{-1}\mathbf{I} \end{bmatrix} \begin{bmatrix} b \\ \boldsymbol{\alpha} \end{bmatrix} = \begin{bmatrix} 0 \\ \mathbf{1}_m \end{bmatrix} \tag{8}$$

where

$$\mathbf{y} = [y_1, y_2, ..., y_m], \mathbf{1}_m = [1, 1, ..., 1], \boldsymbol{\alpha} = [\alpha_1, \alpha_2, ..., \alpha_m],$$
$$\mathbf{z} = [\varphi(\mathbf{x}_1), \varphi(\mathbf{x}_2), ..., \varphi(\mathbf{x}_m)]$$

Copyright © 2009 SciRes

From application of the Mercer condition one can obtain $\mathbf{\Omega} = K(\mathbf{x}_i, \mathbf{x}_j) = \varphi(\mathbf{x}_i)^T \varphi(\mathbf{x}_j),\ i, j = 1, 2, ..., m$. This finally results into the following LS-SVM model for function estimation

$$y = \sum_{k=1}^{m} \alpha_k K(\mathbf{x}, \mathbf{x}_k) + b \tag{9}$$

2.4. LCF Model

Linear combination forecasting model [14] takes the form:

$$\begin{cases} g_t = k_1 g_{1t} + k_2 g_{2t} + k_3 g_{3t} \\ k_1 + k_2 + k_3 = 1 \quad (k_i \geq 0,\ i = 1, 2, 3) \end{cases} \tag{10}$$

where g_t is the value of the linear combination forecasting model; g_{1t}, g_{2t} and g_{3t} are the forecasting values of the single forecasting models respectively, namely, MLR, BP and LSSVM; and k_1, k_2 and k_3 are the weighted coefficients of the three single models respectively. To the linear combination forecasting method, its main task is to adopt optimization measures to obtain the optimal weighted coefficients which can make the error sum of squares of the combined forecasting be least.

3. WNN Combination Forecasting Model for ESDD Predicting

Supposing z_{1i}, z_{2i} and z_{3i} are the *ith* ESDD predicting values of MLR, BP and LSSVM respectively, h_i is the *ith* measured value. One can use z_{1i}, z_{2i} and z_{3i} to construct a nonlinear combination function [15]

$$\hat{h}_i = \varphi_i(Z) = \varphi_i(z_{1i}, z_{2i}, z_{3i}) \tag{11}$$

where, φ is the nonlinear function and $\hat{h}_i$ is the combined forecasting value. In this paper, WNN is used to design the nonlinear function φ.

It is known the nature of wavelet transform [16] is an integral transform between different parameters.

$$w_{ab}(a, b) = \int_{-\infty}^{+\infty} f(x) g(a, b, x) dt \tag{12}$$

where, $g(a,b,x) = \frac{1}{\sqrt{|a|}} g(\frac{x-b}{a})$ is called wavelet basis and $g(x)$ called mother wavelet. a and b are termed as scaling factor and translation factor of $g(a,b,x)$ respectively. To $f(x)$, the resolution of its local structure can be realized through adjusting a、b, namely, gearing the scale and position of wavelet basis window.

WNN [17] is a model which, based upon wavelet analysis, possesses neural network thread. In other words, WNN adopts nonlinear wavelet basis to replace common-used Sigmoid function in traditional neural network. Through linear superposition of nonlinear wavelet basis selected, the combination of the ESDD data of all single forecasting models is realized. The nonlinear combination function in (11) can be fitted as follow, by adopting wavelet basis $g(a,b,x)$:

$$\hat{h}_i = \varphi_i(Z) = \sum_{k=1}^{m} \omega_k g(\frac{\sum_{j=1}^{L} v_{jk} z_{ji} - b_k}{a_k}) \tag{13}$$

where $\varphi_i(Z)$ is the ESDD value of nonlinear combination forecasting corresponding to the measured one h_i; z_{ji} expresses the *ith* prediction value of the *jth* model, $L = 3$; $Z = (z_{1i}, z_{2i}, z_{3i})$; ω_k、v_{jk}、b_k、a_k are the weighted coefficient between output terminal and the *kth* hidden layer node, the weighted between the *jth* input and the *kth* hidden layer node, the translation factor and scaling factor of the *kth* wavelet basis respectively; the number of wavelet basis m is 7, according to the empirical formula $2n+1$. Considering Morlet wavelet possessing relatively good localization and smoothness, it will be selected in (13).

$$g(x) = \cos(1.75x)\exp(-\frac{x^2}{2}) \tag{14}$$

Figure 1 shows the structure of WNN. There are 3 input nodes- z_{1i}, z_{2i}, z_{3i} and one output node- $\varphi_i(Z)$.

The objective of using WNN to carry out regression analysis is to determine the network parameters- ω_k、v_{jk}、b_k and a_k by which $\varphi_i(Z)$ can be fitted optimally with h_i. ω_k、v_{jk}、b_k and a_k can be optimized via Minimum Mean Square Error (MMSE) energy function as follow.

$$E = \frac{1}{2}\sum_{i=1}^{I} [\sum_{k=1}^{m} \omega_k g(\frac{\sum_{j=1}^{L} v_{jk} z_{ji} - b_k}{a_k}) - h_i)]^2 \tag{15}$$

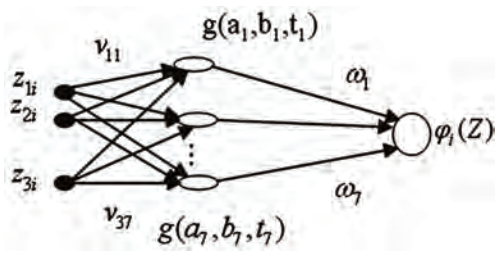

Figure1. The structure of WNN

where, I is the number of training samples and h_i is the ith observed value.

To gain the optimal ω_k、v_{jk}、b_k and a_k is to minimize (15). In this article, gradient descent algorithm is used as WNN learning principle. The details are as followings:

1) Set the objective error function value;

2) Initialize ω_k、v_{jk}、b_k and a_k between [−1,1] by using Genetic Algorithm [18];

3) Select randomly a training mode, and input the learning samples z_{ji} and corresponding output h_i;

4) Work out the predicting value of the network $\hat{h}_i$, the followings are the details:

a) Calculate the gradient of each parameter;

Let $z^* = \sum_{j=1}^{L} v_{jk} z_{ji}$, $S = \frac{z^* - b_k}{a_k}$, then the gradients of (15) are respectively:

$$\frac{\partial E}{\partial \omega_k} = -\sum_{i=1}^{I} [\varphi_i(Z) - h_i] g[\frac{z^* - b_k}{a_k}]$$

$$\frac{\partial E}{\partial v_{jk}} = -\sum_{i=1}^{I} [\varphi_i(Z) - h_i]\omega_k [-\cos(1.75S)\exp(-\frac{S^2}{2})\frac{S}{a_k} - 1.75\sin(1.75S)\exp(-\frac{S^2}{2})\frac{1}{a_k}] z_{ji}$$

$$\frac{\partial E}{\partial b_{jk}} = -\sum_{i=1}^{I} [\varphi_i(Z) - h_i]\omega_k [\cos(1.75S)\exp(-\frac{S^2}{2})\frac{S}{a_k} + 1.75\sin(1.75S)\exp(-\frac{S^2}{2})\frac{1}{a_k}]$$

$$\frac{\partial E}{\partial a_k} = -\sum_{i=1}^{I} [\varphi_i(Z) - h_i]\omega_k [\cos(1.75S)\exp(-\frac{S^2}{2})\frac{S^2}{a_k} + 1.75\sin(1.75S)\exp(-\frac{S^2}{2})\frac{S}{a_k}]$$

b) Introduce momentum factor α to amend each parameter;

$$\omega_k(t+1) = \omega_k(t) - \eta\frac{\partial E}{\partial \omega_k} + \alpha \triangle \omega_k(t)$$

$$v_{jk}(t+1) = v_{jk}(t) - \eta\frac{\partial E}{\partial v_{jk}} + \alpha \triangle v_{jk}(t)$$

$$b_k(t+1) = b_k(t) - \eta\frac{\partial E}{\partial b_k} + \alpha \triangle b_k(t)$$

$$a_k(t+1) = a_k(t) - \eta\frac{\partial E}{\partial a_k} + \alpha \triangle a_k(t)$$

where, η is the learning ratio and α is the momentum factor.

c) Compute current output of WNN: put current parameters into (13) to get current output of the network;

d) Numerate error function value. When the error is less than the set one, the learning process is terminated; otherwise, turns to step (3).

4. Appraisal of Forecasting

In order to evaluate the prediction effects of the combination model comprehensively, according to the practice and principle, the paper uses relative error δ and average relative error $\bar{\delta}$ to evaluate the accuracy of the prediction.

$$\delta = \frac{|y_i - \hat{y}_i|}{y_i} \times 100\% \tag{16}$$

$$\bar{\delta} = \frac{1}{I}\sum_{i=1}^{I}\frac{|y_i - \hat{y}_i|}{y_i} \times 100\% \tag{17}$$

where y_i are the observed values and $\hat{y}_i$ are the predicted ones. These values reflect comprehensively the prediction results. The smaller δ and $\bar{\delta}$ are, the better the generalization of the model and the corresponding parameters are.

5. Experimental Results

On the basis of the model principles and modeling steps in the text, Matlab 7.0 is adopted to write the ESDD prediction programs based on WNN. References [4–7,9] show there is a close relationship between insulators ESDD and meteorological factors. So, for each single model, 120 samples of the historical meteorological data and ESDD data provided by "Optical Sensor System for the ESDD Monitoring of Transmission Equipment" (developed by Wuhan High Voltage Research Institute and Wuhan Kangpu Changqing Software Company) installed on the ESDD monitoring spot of Qingshan District, Wuhan ,from April to June in 2006, are regarded as training set and forecasting set, where 90 samples belong to training set, and the rest 30 samples to test set. Table 1 shows the comparisons between WNN combination forecasting model and LCF, MLR, BP and LSSVM.

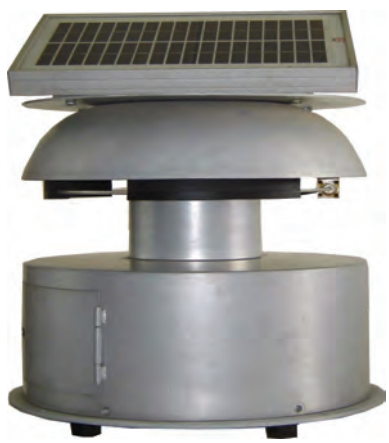

Figure 2. Optical sensor system for the ESDD monitoring of transmission equipment

Table 1. Comparison of forecasting results of ten ESDD

Times	Combination forecasting							Single forecasting			
	WNN			LCF		MLR		BP		LSSVM	
	Actual (mg/cm^2)	Forecasting (mg/cm^2)	δ(%)	Forecasting (mg/cm^2)	δ(%)	Forecasting (mg/cm^2)	δ(%)	Forecasting (mg/cm^2)	δ(%)	Forecasting (mg/cm^2)	δ(%)
2006.4.8	0.0268	0.0278	3.73	0.0252	5.97	0.0286	6.72	0.0249	7.09	0.0284	5.97
2006.4.16	0.0263	0.0271	3.04	0.0276	4.94	0.0291	10.65	0.0247	6.08	0.0286	8.75
2006.4.21	0.0390	0.0381	2.31	0.0375	3.85	0.0412	5.64	0.0421	7.95	0.0363	6.92
2006.5.3	0.0353	0.0362	2.55	0.0367	3.97	0.0331	6.23	0.0334	5.38	0.0342	3.12
2006.5.8	0.0232	0.0244	5.17	0.0244	3.61	0.0248	6.45	0.0251	8.19	0.0247	6.47
2006.5.13	0.0264	0.0255	3.41	0.0251	4.92	0.0239	9.47	0.0292	10.61	0.0244	7.58
2006.5.21	0.0487	0.0497	2.05	0.0517	6.16	0.0534	9.65	0.0527	8.21	0.0460	5.54
2006.6.1	0.0432	0.0414	4.17	0.0421	2.55	0.0463	7.17	0.0410	5.09	0.0455	5.32
2006.6.9	0.0459	0.0442	3.70	0.0481	4.79	0.0491	6.97	0.0427	6.97	0.0482	5.01
2006.6.18	0.0467	0.0484	3.64	0.0491	5.14	0.0411	11.99	0.0488	4.50	0.0451	3.43
$\bar{\delta}$(%)			3.377		4.590		8.094		7.007		5.811

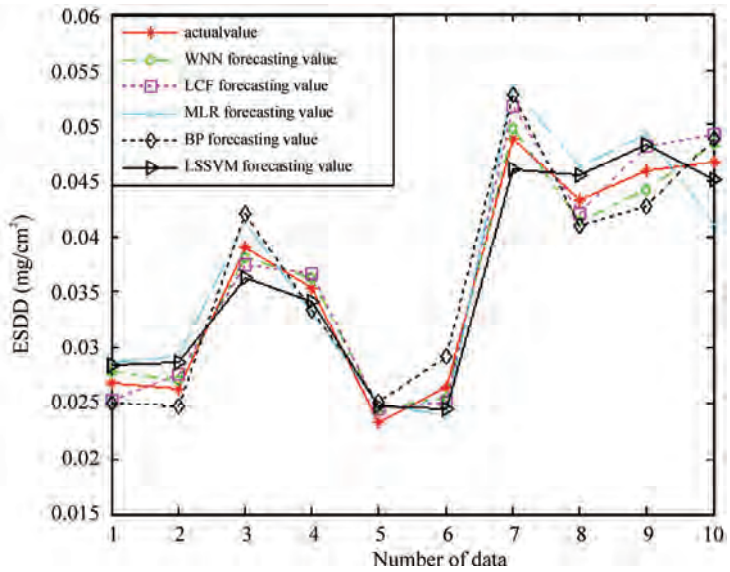

Figure 3. Comparison between the predicted and the measured

From Table 1, it can be seen that the average relative error of MLR is 8.094% which is the biggest one among those of the five forecasting models, and that of WNN is 3.377%, the least one , and each relative error of WNN is less than 6%. The average relative error of LCF is 4.590% which is only bigger than that of WNN. Besides, the maximum relative error of LCF, MLR, BP and LSSVM are 6.16%, 11.99%, 10.61% and 7.58% respectively; while that of WNN is only 5.17%. This indicates that the prediction accuracy of combination model is higher than that of each single model, and compared with linear combination model, WNN combination model presented in the paper is more stable and practical, and can improve efficiently forecasting precision. Using the ESDD predicted by WNN combination forecasting model to divide pollution area can effectively increase the accuracy of pollution distribution map.

6. Conclusions

ESDD is a main factor to classify contamination severity and draw pollution areas map of power network, hence its accuracy directly influences the precision of pollution

distribution map, and further affects the insulation capability of power system.

The WNN combination forecasting model combined with multivariable linear regression technique, BP neural network and least squares support vector machines avoids the limitations of linear combination model and single forecasting model, so it can boost the forecasting accuracy, especially deduce maximum relative error, in other words, it can decline predicting risk. The simulation results in Table 1 show in the five models, the prediction accuracy of WNN combination model is the highest one, namely, the values of WNN are closest to the observed ones. The ESDD values produced by WNN combination forecasting model can better meet the request of drawing pollution distribution map of power network. The model proposed by the paper is an effective and doable way for ESDD forecasting and provides a new thinking for the computerization of drawing pollution distribution map.

REFERENCES

[1] Y. Hu, "The analysis of '2.22 pollution flashover of network' and measure for anti-pollution flashover," High Voltage Engineering, Vol. 27, pp. 30–32, April 2001.

[2] Y. Liu and J. K. Wang, "Analysis of large area pollution flashover occurred in Shaanxi power network on Dec.18, 2000 and preventative measures for similar accidents," Power System Technology, Vol. 26, pp. 82–85, June 2002.

[3] Pollution Classification and External Insulation Selection for Electrical Power System, State Grid Standard Q/GDW152-2006, December 2006.

[4] A. S. Almad, H. Ahmad, M. A. Salam, and Saad Ahmad, "Regression technique for prediction of salt contamination severity on high voltage insulators," in Annual Report Conference on Electrical Insulation and Dielectric Phenomena, pp. 218–221, 2000.

[5] A. S. Almad, H. Ahmad, M. A. Salam, T. Tamsir, Z. Buntat, and M. W. Mustafa, "Prediction of salt contamination on high voltage insulators in rainy season using regression technique," Proceedings of TENCON, Vol. 3, pp. 184–189, 2000.

[6] M. A. Salam, S. M. Ai-Alawi, and A. A Maqrashi, "Prediction of equivalent deposit density of contaminated glass plates using artificial neural networks," Journal of Electrostatics, Vol. 66, pp. 526–530, May 2008.

[7] A. S. Almad, P. S. Ghosh, H. Ahmad, and S. A .K. Aljunid, "Assessment of ESDD on high-voltage insulators using artificial neural network," Electric Power System Research, Vol. 72, pp. 131–136, December 2004.

[8] S. B. Jiao, D. Liu, G. Zheng, and Q. Zhang, "Forecasting the ESDD of insulator based on least squares support vector machine," Proceedings of the CSEE, Vol. 26, pp. 149–153, January 2006.

[9] F. H. Shu and W. X. Zhang, "A prediction model for insulator's ESDD based on least square support vector machine," High Voltage Apparatus, Vol. 44, pp. 420–423, October 2008.

[10] J. M. Bate and C. W. J. Granger, "The combination of forecastings," Operational Research Quarterly, Vol. 20, pp. 451–468, 1969.

[11] Y. Liu. "Mathematical model of multivariable linear regression," Journal of Shenyang Institute of Engineering, Vol. 1, pp. 128–129, Junuary 2005.

[12] J. A. K. Suykens and J. Vandewalle. "Least squares support vector machine classifiers," Neural Process Letters, Vol. 9, pp. 293–300, 1999.

[13] J. A. K. Suykens, L. Lukas, P. Van Dooren, B. Demoor, and J. Vandewalle, "Least squares support vector machine classifiers: A large scale algorithm," ECCTD'99 European Conference on Circuit Theory and Design, pp. 293–300, 1999.

[14] Y. K. Ma and X. W. Tang, "Research on the problem of optimizing linear combination forecasting model," System Engineering – Theory & Practice, Vol. 9, pp. 110–123, September 1998.

[15] X. H. Wen and M. J. Niu, "A new nonlinear combined forecasting method on the basis of neural networks," System Engineering-Theory & Practice, Vol. 12, pp. 66–72, December 1994.

[16] S. X. Li, "Wavelet transform and its applications," Higher Education Press, Beijing, pp. 11–15, 1997.

[17] Q. X. Cuo and L. Liu, "Driving force prediction for inclusion complexation of 2-cyclodextrim with benzene derivatives by a wavelet neural network," Chemical Physics Letters, Vol. 290, pp. 514–518, 1998.

[18] H. F. Liang, G. Y. Tu, and H. W. Tang, "Application of genetic algorithm neural network for short term load forecasting of power system," Power System Technology, Vol. 25, pp. 49–53, January 2001.

Copyright © 2009 SciRes

Energy and Power Engineering, 2009, 100-109
doi:10.4236/epe.2009.12016 Published Online November 2009 (http://www.scirp.org/journal/epe)

Power Management Integrated Circuit with 90Plus Efficiency Used in AC/DC Converter

Yanfeng JIANG
Microelectronic Center, College of Information Engineering, North China University of Technology, Beijing, China
Email: *yanfeng_jiang@yahoo.com*

Abstract: Recently, resonant AC/DC converter has been accepted by the industry. However, the efficiency will be decreased at light load. So, a novel topology with critical controlling mode combined with resonant ones is proposed in this paper. The new topology can correspond to a 90 plus percent of power converting. So, a novel topology of an state of-art integrated circuit, which can be used as power management circuit, has been designed based on the above new topology. A simulator which is specific suitable for the power controller has been founded in this work and it has been used for the simulation of the novel architecture and the proposed integrated circuit.

Keywords: integrated circuit, power management, resonant

1. Introduction

Energy consumption has become one of the primary concerns in electronic design due to the recent popularity of portable devices and environmental concerns related to desktops and servers.[1] The battery capacity has improved very slowly (a factor of 2 to 4 over the last 30 years), while the computational demands have drastically increased over the same time frame.

The resonant controller of AC/DC output mainly uses series resonant as the main structure, it is categorized into two operating zone for load curve [2]. SRC is operated on the resonant point (operated in the inductor load area); LLC is operated below the resonant point and between the second resonant point (operated at the inductor load area). Figure 1 (SRC) and Figure 2 (LLC) below gives further explanation.

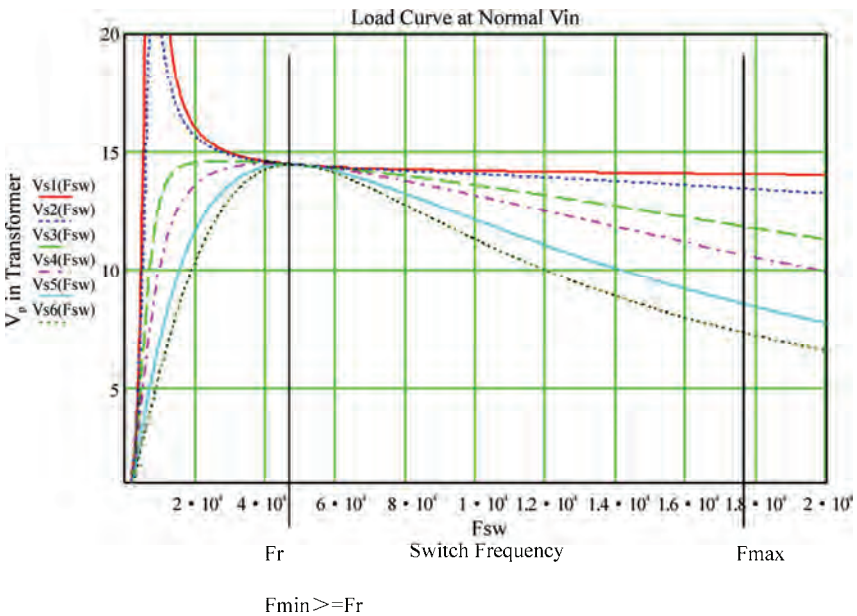

Figure 1. SRC load curve

Copyright © 2009 SciRes

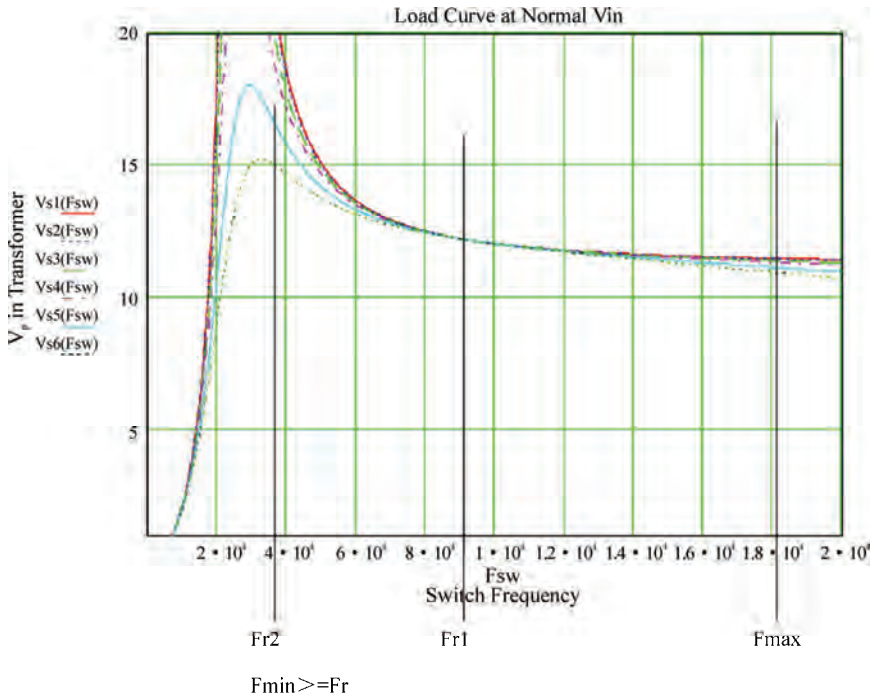

Figure 2. LLC load curve

From Figure 1 SRC load curve, it can be seen that the resonant controller's operating zone, frequency is from Fmin~Fmax. In other words, the switching frequency Fsw operate above the resonant point Fsw>=Fr.[3]

From Figure 1 SRC load curve, it can be seen that the frequency of the resonant controller's operating zone is from Fmin~Fmax. In other words, when operating above the second resonant point and between Fsw>=Fr2~Fr1, at light load the frequency will be Fsw>Fr1. Therefore, comparing the advantage and disadvantage when designing SRC and LLC, LLC is by far more difficult to design compared to SRC. It is difficult to design if load curve is not simulated, so SRC is much easier to design because it only needs to design on a single resonant point. There will not be design issues even if simulation is not done. So, as to the serial resonant controller, there are two operating zone. SRC is the one with switching frequency operated on the resonant frequency while LLC operates between two resonant points, therefore LLC design is comparatively difficult.

For the SRC converter, it can be operated at high efficiency at normal mode, even surplus 90 percent. However, it will be decreased dramatically at light load. So, the total efficiency during the work period is not an ideal one. Authors in this paper have demonstrated that the SRC converter can be combined with different operation modes, CCM and DCM modes. At light load, the converter can be changed into DCM mode. In this way, the novel converter can have an enough high efficiency, even as high as 92%. [4]

2. Design of Critical Switching Mode

Switch Mode Power Supplies (SMPS) can operate in two different conduction modes, each one depicting the level of the current circulating in the power choke when the power switch is turned on. As will be shown, the properties of two black boxes delivering the same power levels but working in different conduction modes, will change dramatically in DC and AC conditions. The stress upon the power elements they are made of will also be affected. This article explains why the vast majority of low-power FLYBACK SMPS (off-line cellular battery chargers, VCRs etc.) operate in the discontinuous area and present a new integrated solution especially dedicated to these particular converters.

Figure 3a and 3b show the general shape of a current flowing through the converter's coil during a few cycles. In the picture, the current ramps up when the switch is closed (ON time) building magnetic field in the inductor's core. When the switch opens (OFF time), the magnetic field collapses and, according to LENZ's law, [5] the voltage across the inductance reverses. In that case, the current has to find some way to continue its flow and start its decrease (in the output network for a FLYBACK, through the freewheel diode in a BUCK etc.).

If the switch is switched ON again during the ramp down cycle, before the current reaches zero (Figure 3a), we talk about Continuous Conduction Mode (CCM). Now, if the energy storage capability of the coil is such that its current dries out to zero during OFF time, the

Copyright © 2009 SciRes

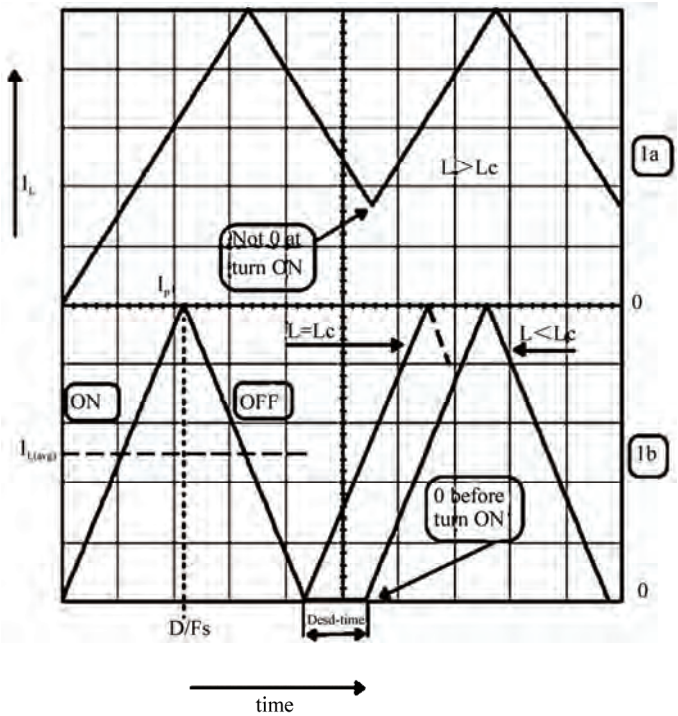

Figure 3. General shape of a current flowing through the converter's coil during a few cycles at different modes (Figure 3a. CCM mode; Figure 3b. DCM mode)

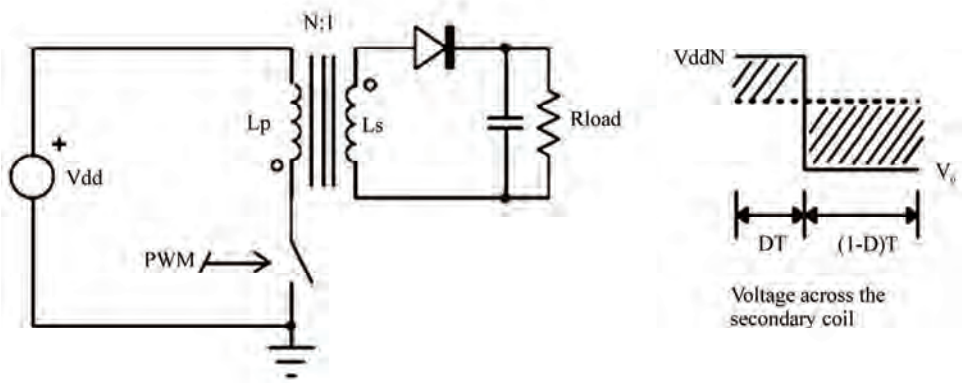

Figure 4. Schematic for determining critical state (Figure 4a. Circuitry schematic of FLYBACK topology; Figure 4b. Voltage wave of Secondary coil)

supply is said to operate in Discontinuous Conduction Mode (DCM), as shown in Figure 3(b). The amount of dead-time where the current stays at a null level defines how strongly the supply operates in DCM. If the current through the coil reaches zero and the switch turns ON immediately (no dead-time), the converter operates in Critical Conduction Mode.

There are three ways you can think of the boundary between the modes. One is about the critical value of the inductance, LC, for which the supply will work in either CCM or DCM given a fixed nominal load. The second deals with a known inductance L. What level of load, RC, will push my supply into CCM? Or what minimum load my SMPS should see before entering DCM? The third one uses fixed values of the above elements but adjusts the operating frequency, FC, to stay in critical conduction. These questions can be answered after a few lines of algebra corresponding to Figure 4's example, a FLYBACK converter:

To help determine some key characteristics of this converter, we will refer to the following

Statements [6]:

Table 1. The poles, zeros and voltage gains in different modes for FLYBACK topology

	DCM mode	CCM mode
The first pole	$\frac{2}{2\times\pi\times R_L\times C_{out}}$	
The second pole		$\frac{(1-D)}{2\times\pi\times\sqrt{L_P\times C_{out}}}$
Left zero	$\frac{1}{2\times\pi\times R_{ESR}\times C_{out}}$	$\frac{1}{2\times\pi\times R_{ESR}\times C_{out}}$
Right zero	$\frac{R_L\times(1-D)^2}{2\times\pi\times L_P\times D}$	$\frac{R_L\times(1-D)^2}{2\times\pi\times L_P\times D}$
$\frac{V_{output}}{V_{input}}$	$N\times D\times\sqrt{\frac{R_L}{2\times L_P\times F_{SW}}}$	$\frac{D}{1-D}\times N$
$\frac{V_{output}}{V_{error}}$	$\frac{V_{input}}{V_{SAW}}\times\sqrt{\frac{R_L}{2\times L_P\times F_{SW}}}$	$\frac{V_{input}}{V_{SAW}}\times(1+\frac{V_{output}}{V_{input}})^2$

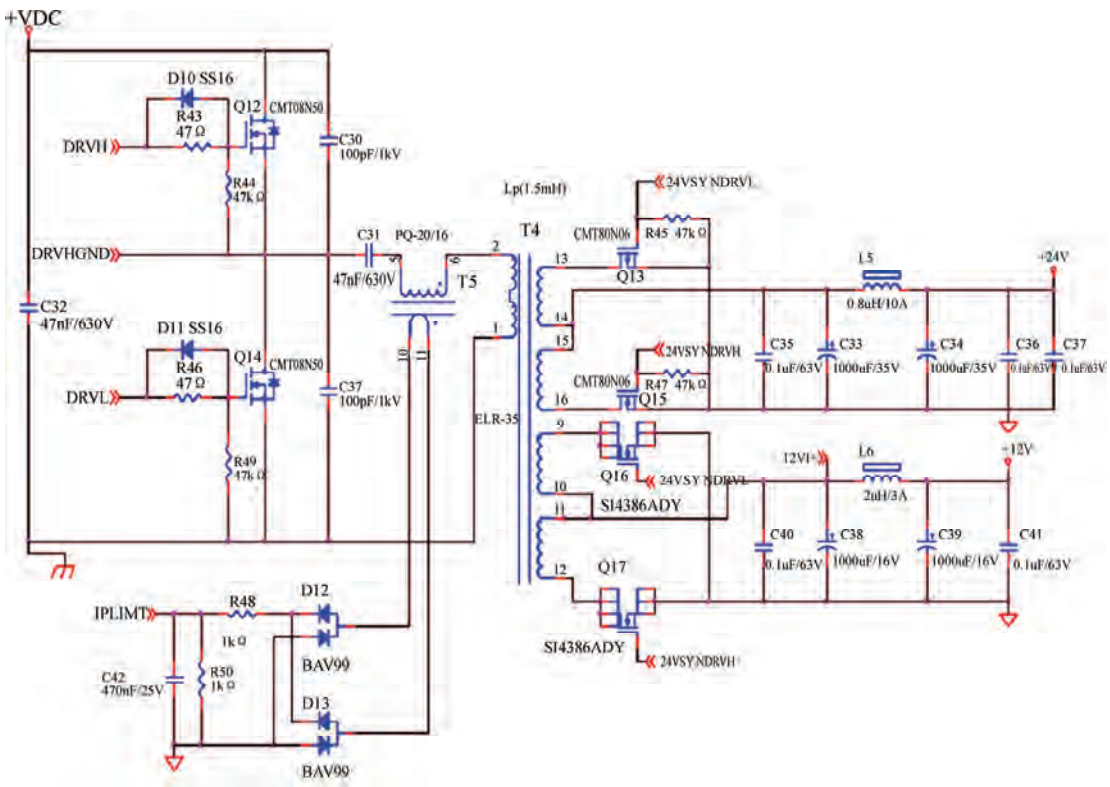

Figure 5. Total architecture of combination of critical mode with resonant ones

1) The average inductor voltage per cycle should be null

2) From figure 1b, when L=LC, IL(avg) = 2xIp

3) An 100% efficiency leads to Pin=Pout

So, the key parameters corresponding to critical mode used in FLYBACK topology converter have been determined. With the same principle, the poles and zeros in DCM and CCM modes can all be deduced, which are shown in Table 1. Additionally, the FLY BACK voltage gain under different modes is included, too.

In Table 1, F_{SW} is switching frequency, V_{SAW} is amplitude of PWM saw wave and L_P corresponds to primary coil.

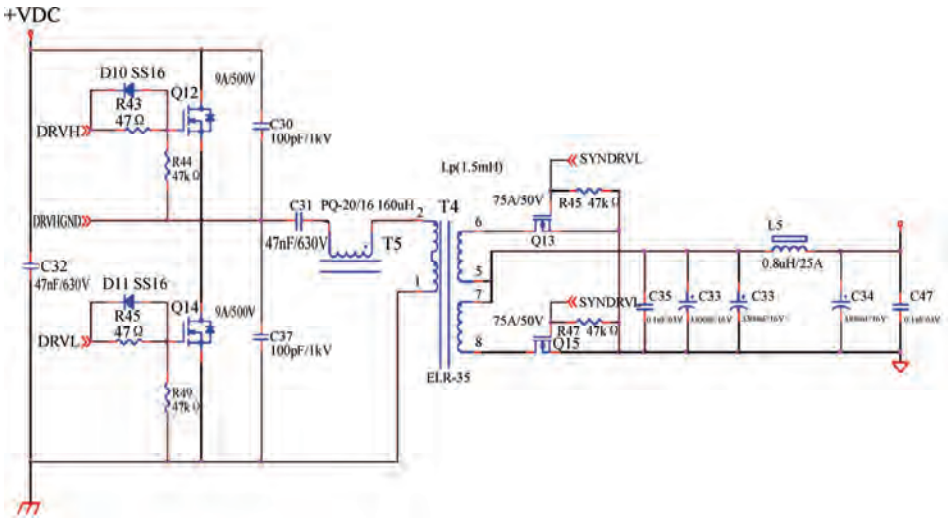

Figure 6. Half bridge circuit

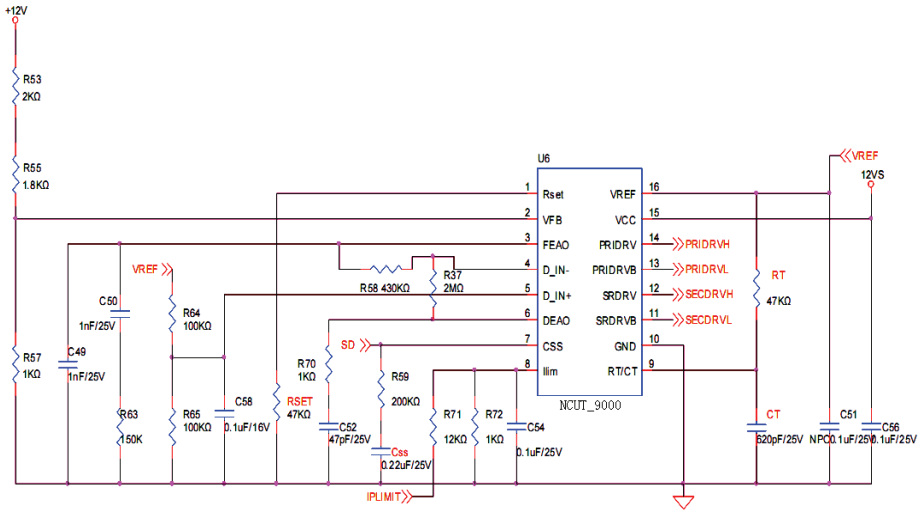

Figure 7. Application diagram of NCUT_9000

3. Total Architecture of Resonant Ones Combined with Critical Controlling Mode

After critical controlling mode be determined, the design process of resonant ones with critical mode is listed below:

1) Input spec (350Vdc ~ 395Vdc)

2) Output spec (normally 5V or 12V/24V)

3) Decide resonant frequency (Fr: normally set at 50 Khz)

4) Decide controller IC (NCUT_9000) Minimum working frequency (same Fmin and Fr)/Maximum working frequency (Fmax normally set at 200Khz)

5) Decide the Q value of resonant frequency (normally set between 0.3 ~ 0.5)

6) Structure Choice (below 500W use half bridge CLASS D, above 500W uses standard half bridge or full bridge).

The total architecture of combination of critical mode with resonant ones is listed in Figure 5.

In Figure 5, the values of key parameters are obtained based on 300W 12V/25A system. Figure 6 is the SRC half bridge circuit.

After the total architecture with 90 plus efficiency has been obtained, we will extract an integrated circuit, which acting as a power management with resonant function and critical mode controller. The circuit is named after our university's abbreviation as NCUT_9000. Its basic function will be introduced in next section. Its application diagram is shown in Figure 7.

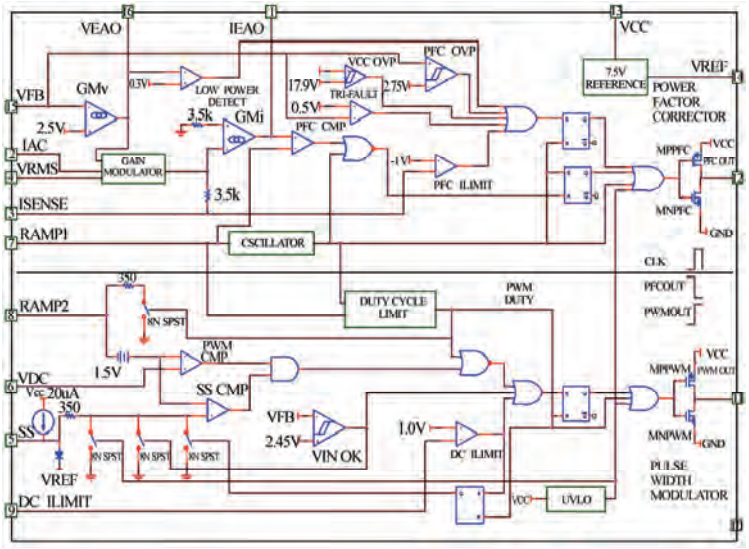

Figure 8. Block diagram of NCUT_9000

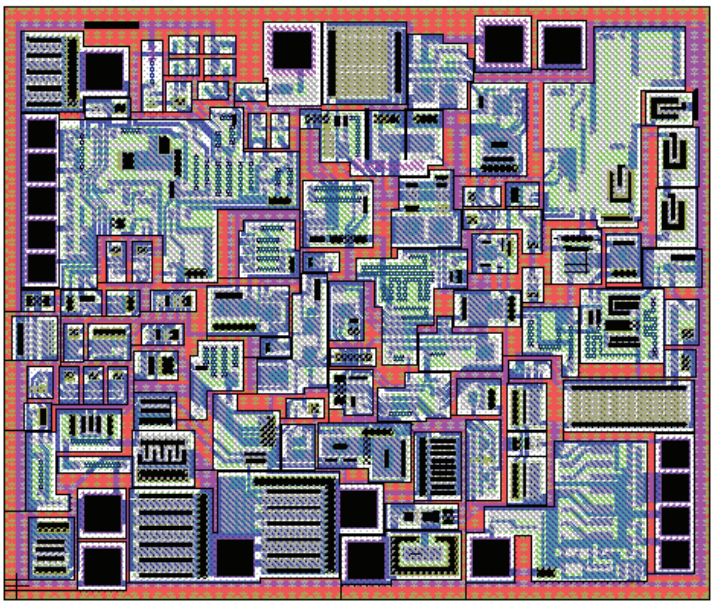

Figure 9. Layout of NCUT_9000, based on TSMC 0.6μm BiCMOS technology

4. Design of NCUT_9000

Based on the above analysis and Figures 5-7, NCUT_9000's block diagram is shown in Figure 8.

The NCUT_9000 is the Green-mode resonant controller in critical mode for Desktop PC and high density AC adapter with 90 plus efficiency. For the power supply, it's input current shaping PFC performance could be very close to the performance of ML4800 leading edge modulation average current topology.

NCUT_9000 offers the use of smaller, lower cost bulk capacitors, reduces power line loading and stress on the switching FETs, and results in a power supply fully compliant to IEC1000-3-2 specifications. This IC includes circuits for the implementation of a leading edge modulation, input current shaping technique "boost" type PFC and a trailing edge modulation current.

This circuit operates at 100kHz. A PFC OVP comparator shuts down the PFC section in the event of a sudden decrease in load. The PFC section also includes peak current limiting for enhanced system reliability.

The layout of NCUT_9000 is shown in Figure 9, based on TSMC 0.6μm BiCMOS technology.

Copyright © 2009 SciRes

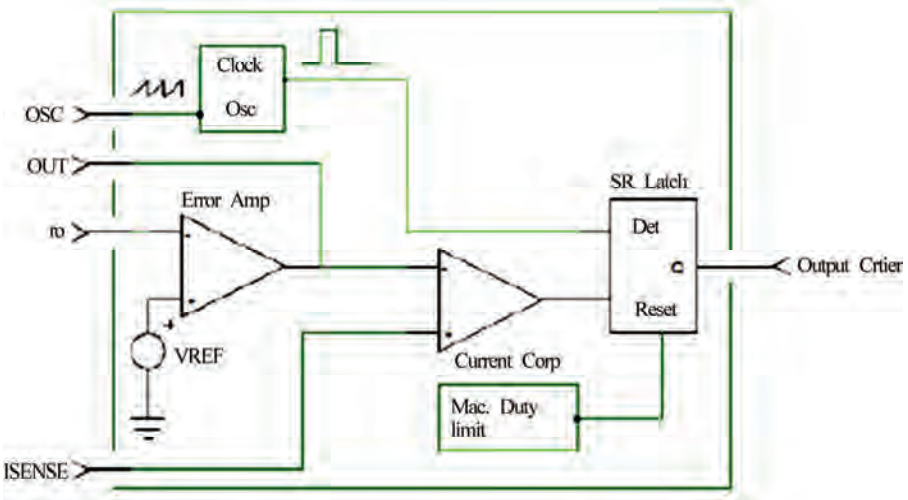

Figure 10. The internal circuitry of a generic single output CCM PWM controller

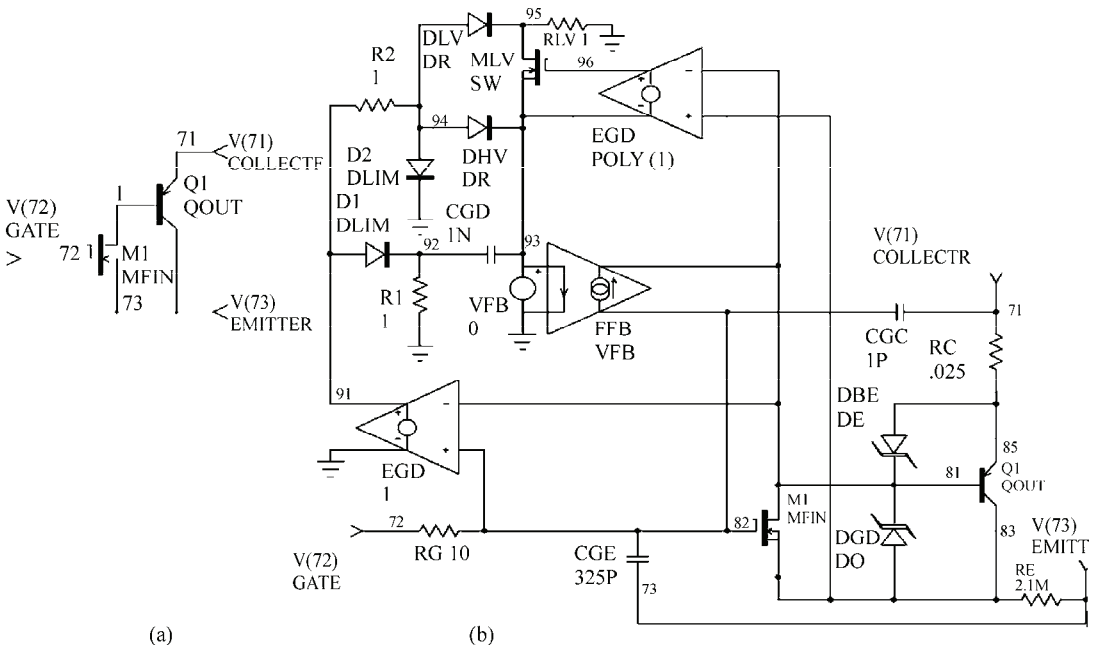

Figure 11. The simplified diagram for IGBT and its macro model (Figure 11(a). The simplified diagram for IGBT; Figure 11(b). The IGBT's macro models)

5. Simulation of Power Supply Controller Combined with Output Power IGBT Device

Power supplies controller is notoriously difficult to simulate as component models in SPICE, due to the inherent instability of oscillator circuits in computer simulator. SPICE can all too often settle into a static mode where the circuit no longer oscillates, or takes so long to converge between time iterations as to make simulation too time consuming to be useful. Simulating the switching behavior of a Switch Mode Power Supply (SMPS) is not always an easy task. This is especially true if the designer wants to use an exact SPICE model for the Pulse Width Modulator (PWM) controller which will be used in the design. The PWM model may exist, but its syntax may be incompatible with your simulator. The solution that is proposed in this part consists of writing your own generic model of the PWM controller and then adapting its intrinsic parameters to comply with the real one you are using. Fixed frequency Current Control Mode (CCM) models will be thoroughly covered in this part. Based on this simulator, Voltage Control Mode (VCM) model can

be done quickly in the same principle. For the power system, there always exist the power driver devices. The biggest stumbling block that engineers run into is turning vendor data sheet specifications into SPICE models that emulate real devices and run without convergence problems. This is especially true for power devices, like IGBTs, where the cost of testing and possibly destroying devices is prohibitive. For the demand to simulate the whole circuit with SMPS controller and power driver device, the macro model for IGBT is extracted and combination has been made on the two models.

Figure 10 shows the internal circuitry of a generic single output CCM PWM controller, which being the most well known architecture. The modelling of such a block consists the below two aspects. One is defining and testing each subcircuit individually. The other should be assembling all of these domino-like circuits to form the complete generic model. All individual blocks should be tested before they are used within larger models.

An IGBT is really just a power MOSFET with an added junction in series with the drain. This creates a parasitic transistor driven by the MOSFET and permits increased current flow in the same die area. The sacrifice is an additional diode drop due to the extra junction and turn-off delays while carriers are swept out of this junction. Figure 11(a) shows a simplified schematic of an IGBT. Note that what is called the "collector" is really the emitter of the parasitic PNP. What we have is a MOSFET driving an emitter follower. Although this model is capable of producing the basic function of an IGBT, refinements are required for more accurate modeling and to emulate the non-linear capacitance and breakdown effects. Figure 11(b) shows the complete subcircuit. The subcircuit is generic in nature, meaning that component values in the subcircuit can be easily recalculated to emulate different IGBT devices. The model accurately simulates, switching loses, nonlinear capacitance effects, on-voltage, forward/reverse breakdown, turn-on/turn-off delay, rise time and fall tail, active output impedance, collector curves including mobility modulation.

Based on the above simulator which has been founded following the above analysis, the simulation results for NCUT_9000 have been listed in Figure 12, Figure 13 and Figure 14. Figure 12 shows the high voltage input load curve. Figure 13 shows the regular voltage input load curve and Figure 14 shows the low voltage input load curve.

Compared the three curves shown in Figure 12 to Figure 14, one can observe the fact that they all work in an apparent resonant mode. The property of the total power converter is less influenced by the load variation. So, the improvement on the property compared with conventional resonant ones can be observed under different load condition.

6. Conclusions

A novel architecture of power converter for AC-DC is proposed in this paper. Based on conventional resonant ones, the critical mode has been added on it. The principle of this architecture has been demonstrated by actual circuit design. The total circuit for the architecture is implemented and an IC circuit extracted from the total circuit is discussed, which named NCUT_9000, denoting the efficiency of this circuit be higher than 90%. As far as authors know, this is the first integrated circuit with intelligent property on power converter's architecture.

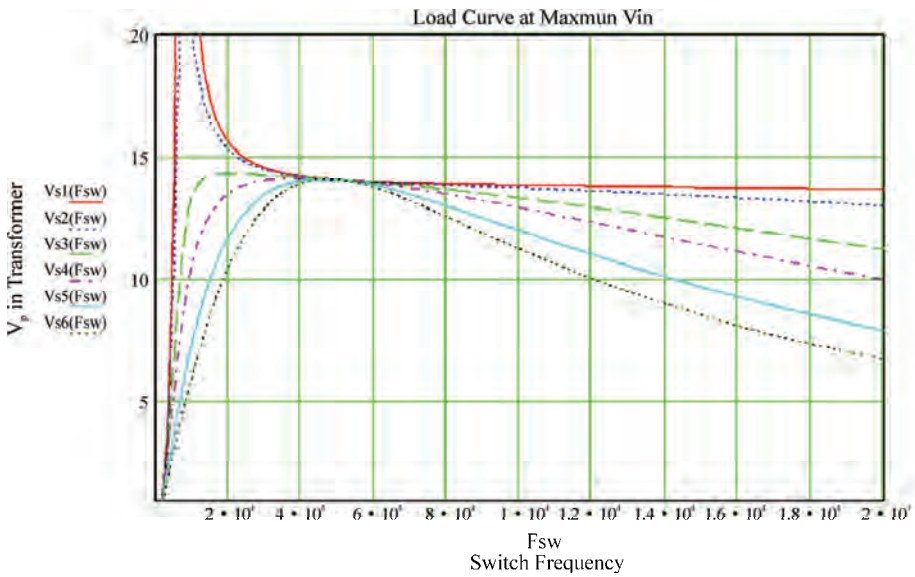

Figure 12. High voltage input load curve

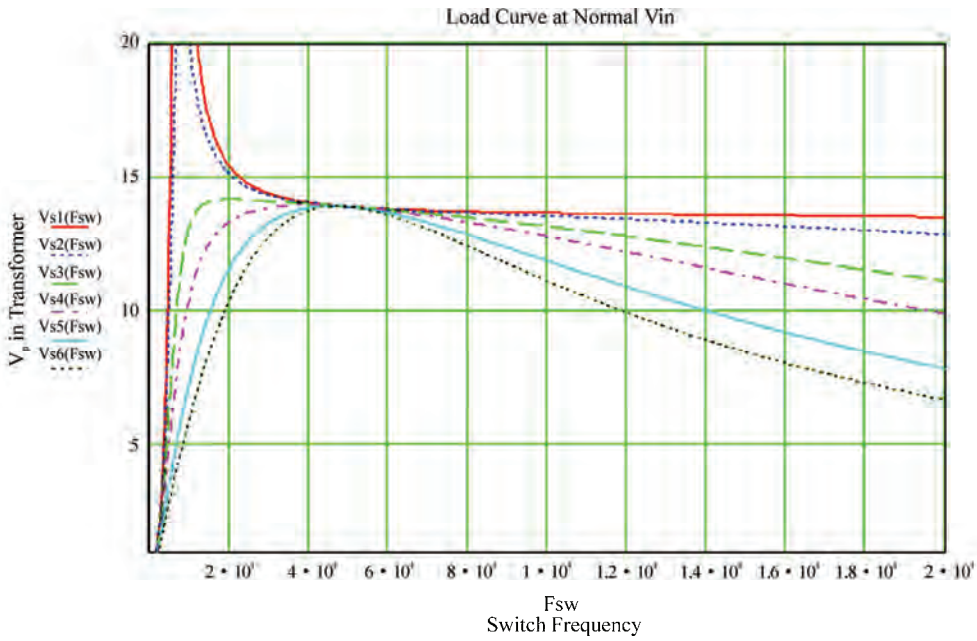

Figure 13. Regular input voltage load curve

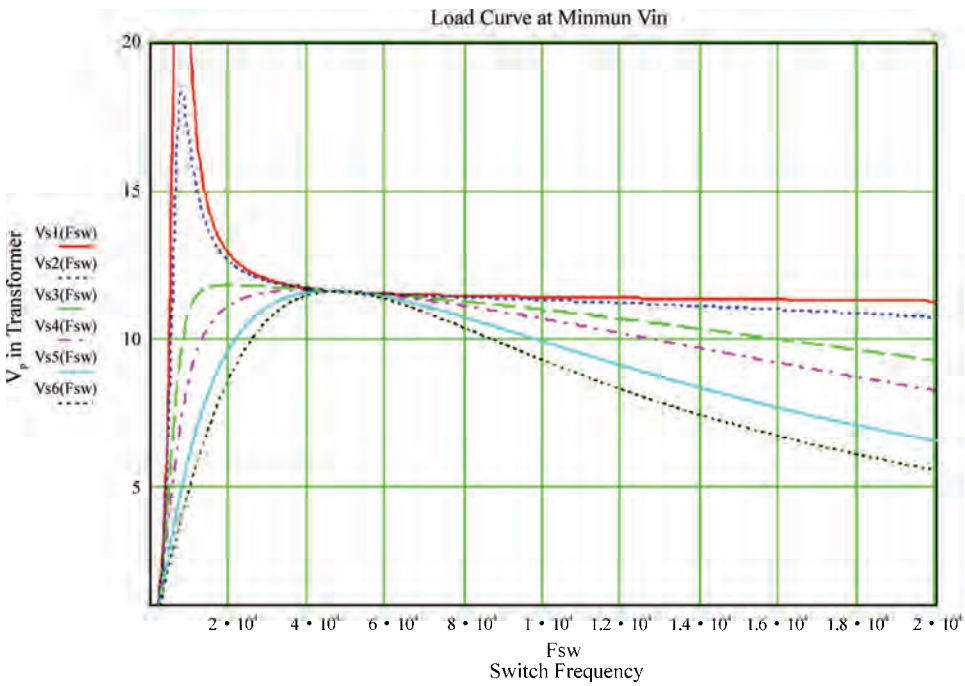

Figure 14. Low input voltage load curve

The properties of IC is discussed. The layout of IC is listed, too. Moreover, a simulator tool, which is suitable for the critical mode circuit, has been founded, which is specific for simulation of power controller. Based on the simulator, the novel architecture and the proposed IC have been demonstrated, which shows that the power efficiency has been improved on light load.

7. Acknowledgement

This work is supported by Natural Science Foundation of China under No.60876078, Funding Project for Academic Human Resources Development in Institutions of Higher Learning Under the Jurisdiction of Beijing Municipality. (PHR(IHLB)) and Beijing Novel Research

Star(2005B01) funded by Ministry of Beijing Science and Technology.

REFERENCES

[1] R. D. Middlebrook and S. Cuk, "A general unified approach to modeling switching converter power stages [J]," IEEE PESC, Vol. 21, No. 1, pp. 18–34, 2005.

[2] Y. F. Jiang and M. X. Xie, "Micro-nano electron devices [M]," Chemical Industry Press, Beijing, 2005

[3] R. Keller, "Closed loop testing and computer analysis aid design of control systems [J]," Electronic Design, Vol. 22, No. 12, pp. 132–138, 1978.

[4] V. Vorperian, "Simplified analysis of PWM converters using the model of the PWM switch, Parts I (CCM) and II (DCM) [J]," Transactions on Aerospace and Electronics Systems, Vol. 26, No. 3, pp. 21–48, 1990.

[5] S. Sandler, "SMPS simulations with SPICE3 [M]," McGraw, 1990

[6] S. Ben-Yaakov, "Average simulation of PWM converters by direct implementation of behavioral relationships [C]," IEEE Applied Power Electronics Conference (APEC'93), pp. 510–516, 1993.

Copyright © 2009 SciRes

Energy and Power Engineering, 2009, 110-115
doi:10.4236/epe.2009.12017 Published Online November 2009 (http://www.scirp.org/journal/epe)

Optimal Performance for Solar Thermal Power System

Jianfeng LU[1], Jing DING[1], Jianping YANG[2]
[1]*School of Engineering, Sun Yat-Sen University, Guangzhou, China*
[2]*Key Laboratory of Enhanced Heat Transfer and Energy Conservation of the Ministry of Education, South China University of Technology, Guangzhou China*
Email: *liujf01@mails.tsinghua.edu.cn*

Abstract: Solar thermal power is currently one of the important trends and research hotspots of solar energy. In present paper, basic physical model is proposed to investigate the solar thermal power, and the operating temperature is optimized to maximize the electricity generating efficiency. When the concentrated energy flux rises, the absorption efficiency of heat receiver will first increase and then decrease, while the increasing of flow velocity can improve the absorption performance. As the working temperature rising, the heat loss of infrared radiation and natural convection increases quickly, so the absorption efficiency obviously decreases, while the Carnot efficiency of the steam turbine cycle will rise. Because of the coupling effects of the heat absorption cycle and turbine cycle, the electricity generating efficiency will reach maximum with the optimal working temperature.

Keywords: solar energy, heat receiver, operating temperature, electricity generating efficiency

1. 引 言

太阳能作为最丰富和可广泛获取的可再生能源形式，对解决能源危机和环境问题有特别重要的作用。太阳能热发电系统主要由聚光系统、吸热传热系统和发电系统构成[1]。太阳能热发电系统的发电系统类似常规电站，其效率受限于 Carnot 循环效率，主要由介质工作温度决定。

吸热器是太阳能光热转化的核心部件，其工作温度和吸热效率直接影响电站的发电效率，因此得到广泛的关注和研究。Fujiwara 等[2]实验研究了空间太阳能热利用系统中热管吸热器的热力学性质。吸热器的能量损失决定系统吸热效率，主要包括自然对流和辐射传热。Clausing[3]分析了腔式吸热器中对流传热引起的能量损失。Dehghan 与 Behnia[4]研究了腔式吸热器中自然对流与辐射的联合作用。通过分析整个热发电系统，研究者对吸热器的构型和操作温度进行了优化。刘志刚等[5]设计一种高效率的新型腔式吸热器，并进行了实验研究。Steinfeld 与 Schubnell[6]研究了腔式吸热器吸热过程的优化尺寸和工作温度。Segal 与 Epstein[7]根据经验关联式提出了热发电系统的优化操作温度。目前，太阳能热发电系统中吸热传热循环与发电循环的耦合及优化性能还有待深入研究。

本文建立太阳能热发电系统的基本物理模型，由此分析系统发电效率并优化工作温度。利用太阳能吸热系统的吸热传热模型，研究吸热管壁面温度与吸热效率的变化特征，特别分析聚光热流密度、流速与工作温度的影响。通过吸热传热循环与发电循环的耦合，分析发电效率最大时的优化温度。

2. 太阳能热发电系统的物理模型

太阳能热发电系统的基本热力学循环如图 1 所示，主要包括吸热传热循环和发电循环，聚光系统产生的高能流辐射可作为吸热器的热边界条件。吸热传热循环中，工作介质首先被泵从低温蓄热器抽入吸热器（进口温度 T_{f0}），然后吸收聚光系统汇聚的太阳光能提高温度并存入高温蓄热器（工作温度 T_{f1}），高温介质与发电循环进行热交换降低温度后流回低温蓄热器。发电循环中，工作介质通过与吸热传热循环进行热交换提高温度，然后利用发电机对外做功并发电。

工作介质在吸热传热循环中起重要作用，常用蓄热传热介质有水/水蒸气，空气与熔融盐等。空气介质具有比较广的工作温度范围，在高温热发电和小型系统

Copyright © 2009 SciRes

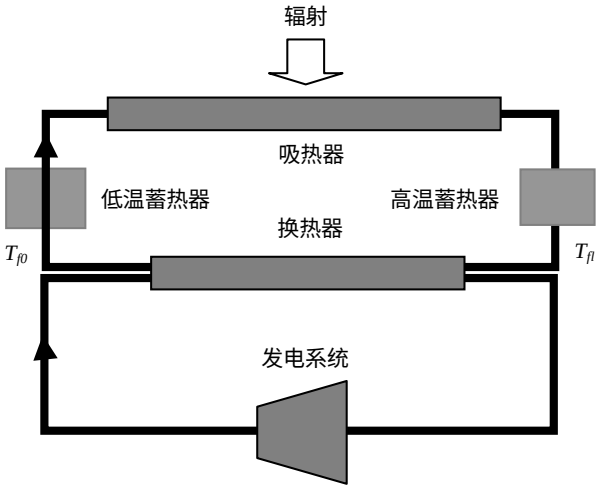

图 1. 太阳能热发电系统
Figure 1. Solar thermal power system

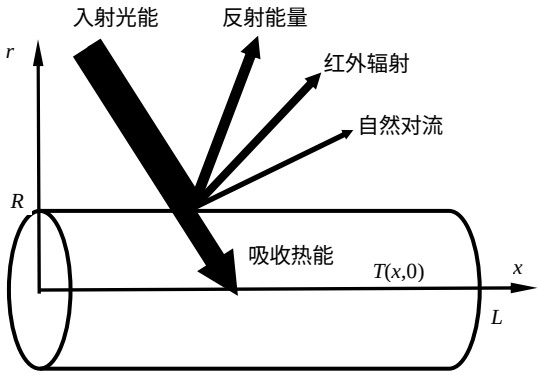

图 2. 吸热管内外的传热过程
Figure 2. The heat transfer process in the heat receiver

中有广泛的应用前景，可以作为研究热发电的理想模型。为降低辐射能量损失，吸热器表面通常涂有太阳能选择性吸收涂层，研究者开发了大量的太阳光谱选择性吸收涂层[8-9]。

相比吸热与发电过程的能量损失，蓄热和传热过程的能量损失相对较小，本文主要分析吸热和发电过程的能量利用效率。为理论简化和分析太阳能热发电系统中的吸热过程，研究轴对称直管道的吸热过程。如图 2 所示，吸热管半径为 R，表面具有太阳能选择性吸收涂层，管壁厚度与热阻忽略。能流密度为 I 的入射光首先被涂层表面反射，涂层反射系数为 $\kappa=1-\alpha$，α 为吸收系数。管外传热引起的能量损失主要包括自然对流与红外辐射，其中自然对流系数为 h_n，红外辐射发射系数为 ε。管内吸收的热能通过强迫对流传递。

由上所述，吸热管壁面吸热传热的能量守恒方程为：

$$I-\kappa\cdot I=\alpha I=h_n(T_w-T_s)+\varepsilon\cdot\sigma T_w^{\ 4}+q_f \tag{1}$$

其中 T_s 为环境温度，T_w 为壁面温度，q_f 为管内对流传热热流密度。

对于管内充分发展流，对流换热可表示为：

$$q_f=h_f\cdot\left(T_w-T_f\right) \tag{2}$$

其中 h_f 为强迫对流换热系数，T_f 为管内流体温度。吸热管内流动通常为湍流，其换热系数可以由实验关联为[10]：

$$h_f=\mathrm{Nu}\cdot\frac{k}{D} \tag{3}$$

$$\mathrm{Nu}=0.0243\,\mathrm{Re}^{0.8}\,\mathrm{Pr}^{0.4} \tag{4}$$

式(2)代入式(1)得

$$\alpha I = h_n(T_w - T_s) + \varepsilon \cdot \sigma T_w^{\ 4} + h_f \cdot \left(T_w - T_f\right) \tag{5}$$

管内沿流向的能量方程为

$$\begin{aligned} q_f \cdot 2\pi R &= \frac{\partial}{\partial x}\int_0^R \rho c_p T u(r) 2\pi r dr \\ &= \rho c_p \frac{\partial T_f}{\partial x}\int_0^R u(r) 2\pi r dr = \rho c_p \frac{\partial T_f}{\partial x} \cdot \pi R^2 u_{\text{av}} \end{aligned} \tag{6}$$

其中 u_{av} 为管内平均流速。

壁面局部吸热效率和吸热管平均吸热效率分别为：

$$\eta_{ab} = \frac{q_f}{I} = \frac{h_f\left(T_w - T_f\right)}{I} \tag{7}$$

$$\overline{\eta_{ab}} = L^{-1}\int_0^L \eta_{ab} dx \tag{8}$$

发电循环中，热力学效率主要由介质工作温度 T_{fl} 决定，初步研究中可简化为 Carnot 循环效率[11]，即

$$\eta_c = \frac{T_{fl} - T_s}{T_{fl}} \tag{9}$$

太阳能热发电系统中，聚光效率主要由聚光系统和辐射条件决定，与系统工作温度无关。对于已经由聚光系统会聚到吸热器的太阳光能，其聚光发电效率可表示为吸热效率与热力循环效率之积，即

$$\eta = \overline{\eta_{ab}}\eta_c \tag{10}$$

以一小型电站为例具体研究太阳能热发电系统的基本性能和优化参数。吸热管管径 R=0.01m，管长 L = 1 m，自然对流传热系数和环境温度分别为 5Wm^{-2}K^{-1} 与 293K。文中计算采用空气的基本热力学性质为，ρ=1.77kgm^{-3}，c_p=1006Jkg^{-1}K^{-1}，Pr=0.743，k=0.0181Wm^{-1}K^{-1}，μ=0.0000134kgm^{-1}s^{-1}。管壁采用 Co-Cd-BT 涂层[12]，其辐射性能吸收系数 α=0.96，发射系数 ε=0.12。

3. 太阳能热发电系统的性能优化

首先研究吸热管的基本吸热性能，图 3 表示不同聚光热流密度下的壁面温度和吸热效率，其中 T_f=473K，u_{av}=5.0m/s。壁面温度随聚光热流密度提高而线性增加，热流密度为 20kWm^{-2} 时壁面温度达到 900K。低聚光热流密度时，随聚光热流密度上升，能量损失缓慢上升，而吸热效率显著提高。高聚光热流密度时，随聚光热流密度上升，能量损失特别是红外辐射能量显著提高，因此吸热效率随之下降。聚光热流密度在最优值 12kWm^{-2} 时，吸热效率达到最大值 60.8%。

图 4 表示不同流速条件下的壁面温度和吸热效率，其中 T_f=473K，I=10kWm^{-2}。随着管内流速的提高，管内换热条件明显改善，壁面温度随着降低，而吸热效率显著提高。流速低于 5 m/s 时，吸热效率低于 60%，严重限制该热发电系统的发电效率。流速高于 15 m/s 时，管内流动换热的热阻较小，吸热效率缓慢增加，但流动的驱动功率将显著提高。根据吸热器的基本性能，热发电系统需要优化聚光热流密度和管内对流流速。

太阳能热发电系统中，吸热传热循环和发电循环的耦合对聚光能量的发电效率起着关键作用，其中最重要的因素为工作温度。工作温度上升时，吸热器表面自然对流和红外辐射的热损失明显增加，由此降低吸热效率，而发电循环效率则随温度升高而提高，因此

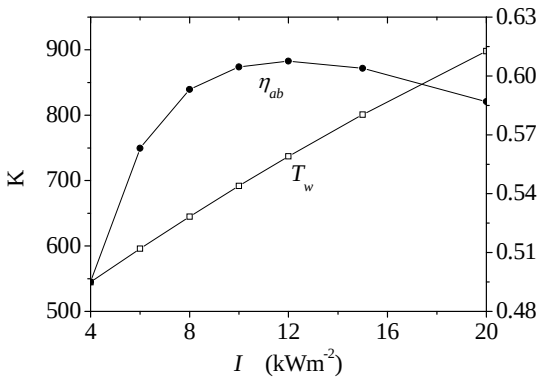

图 3. 不同能流密度下壁面温度和吸热系数分布

Figure 3. The temperature distributions and absorption efficiency under different energy fluxes

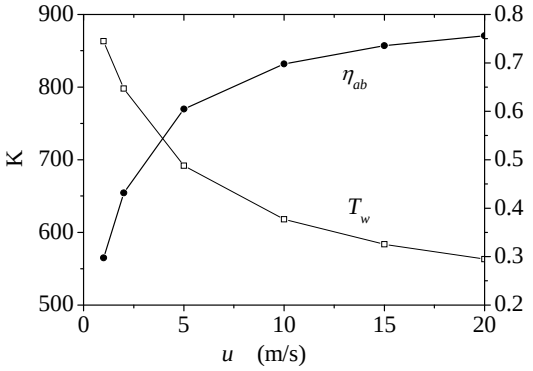

图 4. 不同流速条件下壁面温度分布和吸热系数分布

Figure 4. The temperature distributions and absorption efficiency under different velocities

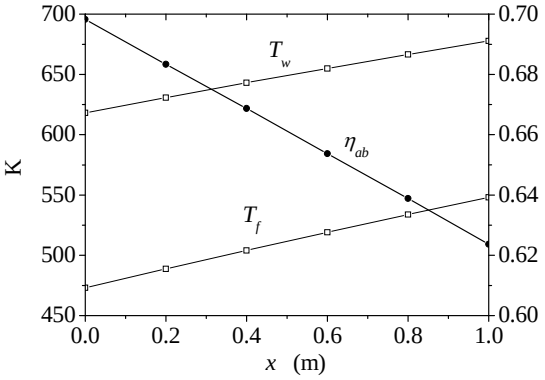

(a) T_0=473K

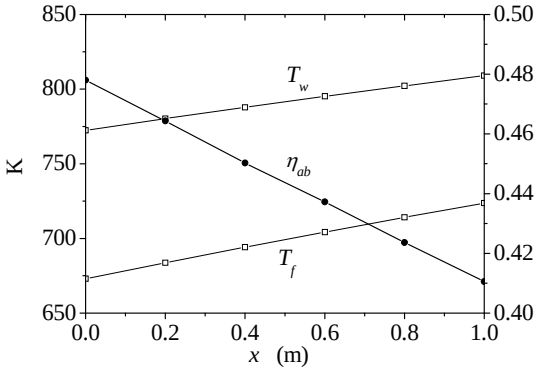

(b) T_0=673K

图 5. 不同进口温度下的壁面温度和吸热系数分布

Figure 5. The temperature distributions and absorption efficiency under different inlet temperatures

存在系统的优化状态。考虑吸热器进口温度分别为 T_{f0}=473K 或 673K，则吸热管沿程壁面温度和吸热效率分布如图 5，其中 u_{av}=10.0m/s，I=10kWm^{-2}。沿着流线方向，壁面温度和主流温度逐渐增加，而吸热效率则逐渐降低。吸热器进口温度与工作温度上升时，吸热器的平均吸热效率显著降低。吸热器进口温度由 473K 提高到 673K 时，吸热器的平均吸热效率由 66.1% 降低至 44.4%，同时其工作温度从 678K 提高到 809K。

由式（6）和（7），吸热管吸热效率和发电循环效率随工作温度的变化情况图 6，其中 u_{av}=10.0m/s，I=10kWm^{-2}。随着工作温度提高，自然对流和红外辐射引起的热损失增加，吸热管吸热效率显著降低，工

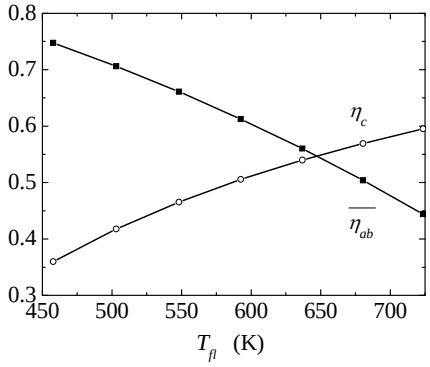

图 6. 不同工作温度下吸热效率和 Carnot 效率

Figure 6. The absorption and Carnot efficiencies under different working temperatures

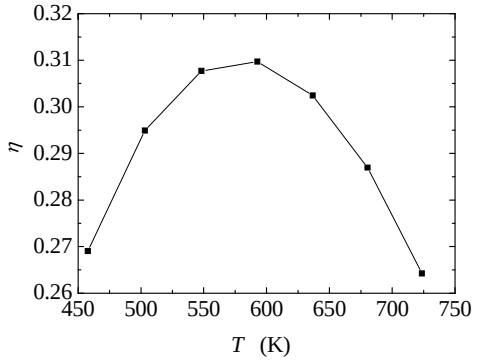

图 7. 不同工作温度下聚光发电效率

Figure 7. The electricity generating efficiency under different working temperatures

作温度由 458K 提高到 724K 时吸热器平均吸热效率由 74.8%降低至 44.4%。另一方面，发电循环效率则随工作温度的提高而显著上升，工作温度由 458K 提高到 724K 时发电循环效率由 36.0%升至 59.5%。

图 7 为太阳能热发电系统聚光发电效率随工作温度变化情况，其中 u_{av}=10.0m/s，I=10kWm^{-2}。工作温度较低时，发电循环效率的提高起主导作用，因此聚光发电效率随工作温度上升而提高。工作温度较高时，吸热器吸热效率随温度升高而下降起主要作用，因此聚光发电效率随工作温度上升而降低。由于发电循环和吸热传热的耦合，优化工作温度为 590K，此时聚光发电效率达最大值 31.0%。由图 3-4，聚光能流密度和流速显著影响吸热效率和壁面温度，因此可以进一步影响优化温度和发电效率。

4. 结 论

本文建立了太阳能热发电系统的基本物理模型，并通过分析吸热传热循环与发电循环的耦合导出优化工作温度。文中首先研究具有太阳能选择性吸收涂层的聚光太阳能吸热管的吸热传热特性。随着入射光能增加，吸热管壁面温度随之线性升高，而吸热效率则先增加后减少。增加流速可以提高吸热管性能，吸热效率随流速增加而减少，而管壁温度则显著下降。随着工作温度提高，自然对流和红外辐射引起的热损失增加，因此吸热管吸热效率显著降低。发电循环效率的变化趋势与吸热效率相反，随工作温度升高而迅速提高。由于发电循环与吸热传热循环的耦合，聚光发电效率在工作温度为优化温度时达最大值。

REFERENCES

[1] S. A. Kalogirou, “Solar thermal collectors and applications,” Progress in Energy and Combustion Science, Vol. 30, pp. 231–295, 2004.

[2] M. Fujiwara, T. Sano, K. Suzuki, *et al*., “Thermal analysis and fundamental tests heat pipe receiver for solar dynamic space system,” Journal of Solar Energy Engineering, Vol. 112, pp. 177–182, 1990.

Copyright © 2009 SciRes

[3] A. Clausing, "Analysis of convective losses from cavity solar central receivers," Solar Energy, Vol. 27, pp. 295–300, 1981.

[4] A. A. Dehghan and M. Behnia, "Combined natural convection conduction and radiation heat transfer in a discretely heated open cavity," ASME Journal of Heat Transfer, Vol. 118, pp. 54–56, 1996.

[5] Z. G. Liu, C. P. Zhang, Y. H. Zhao, and D. W. Tang, "The design and experiments of a new cavity absorber," Acta Energiae Solaris Sinica, Vol. 26, pp. 332–337, 2005. (in Chinese)

[6] A. Steinfeld and M. Schubnell, "Optimum aperture size and operating temperature of a solar cavity-receiver," Solar Energy, Vol. 50, pp. 19–25, 1993.

[7] A. Segal and M. Epstein, "Optimized working temperatures of a solar central receiver," Solar Energy, Vol. 75, pp. 503–510, 2003.

[8] C. E. Kennedy, "Review of mid- to high-temperature solar selective absorber materials," NREL/TP-520-31267, 2002.

[9] Y. Sun, Y. Y. Shi, and F. C. Wang, "Study on thermal stability of solar selective absorbing surfaces with new material," Acta Energiae Solaris Sinica, Vol. 23, pp. 39–42, 2002. (in Chinese)

[10] J. H Lienhard IV and J. H. Lienhard V, "A heat transfer textbook," Phlogiston Press, Chambridge, Massachusetts, U.S.A, 2002

[11] R. T. Stephen, "Thermodynamics: concepts and applications," Cambridge University Press, New York, 2006

[12] L. Cindrella, "The real utility ranges of the solar selective coatings," Solar Energy Materials and Solar Cells, Vol. 23, pp. 1898–1901, 2007.

Copyright © 2009 SciRes

Energy and Power Engineering, 2009, 116-121
doi:10.4236/epe.2009.12018 Published Online November 2009 (http://www.scirp.org/journal/epe)

Study on Lignite-Blended Burning Technology in the 1025t/h Bituminous Boiler

Jinfeng MA[1], Jingxing WU[2], Tianshu ZHOU[2], Jie LENG[2], Chong JIANG[2]
[1]*Shenyang Engineering Institute, Shenyang,China*
[2]*Northeast Electric Power Research Institute Co., Ltd., Shenyang, China*
Email: *majf* 69*@yahoo.com.cn*

Abstract: Due to a serious shortage of the coal in Tonghua, a retrofit solution of mixing warm flue gas extracted from reversing chamber into the coal pulverizing system and cold air into the hot air coal pulverizing system is proposed so as to reduce oxygen content. At the end of the pulverizing system and medium temperature of the conveying system, dual-channel combustion burner is transformed into horizontal bias combustion burner. The measurement results show that 50% ratio of lignite blended in the 1025t/h bituminous boiler is feasibility. It is also an important technology to reduce NO_x pollutant emission.

Keywords: coal pulverizing system, blended coal burning, lignite, warm flue gas, explosion prevention, drying capacity

1. 引 言

为拓宽燃煤范围，国内许多研究单位开展了燃煤掺烧的研究工作[1-3]。为实现在中储式制粉系统烟煤锅炉中大比例掺烧褐煤，文献[4,5]采用在锅炉转向室抽取中温炉烟掺入制粉系统的改造技术，在 200MW 机组烟煤锅炉上成功实现了大比例掺烧褐煤。

目前通化地区煤源供应严重不足，浑江发电责任有限公司 2×1025t/h 机组锅炉原设计煤种属于劣质烟煤，挥发分和热值均较低，如果直接掺烧褐煤，制粉系统爆炸和燃烧器烧损问题最为突出。为最大限度掺烧褐煤，本文采取在转向室抽吸中温炉烟掺入制粉系统、热风送粉系统中加入调温风的改造方案，以降低制粉系统末端氧量以及送粉系统介质的温度，提高制粉系统防爆和干燥能力；将双通道煤粉燃烧器改造为水平浓淡燃烧器，保护燃烧器不被烧损，并进行了改造试验研究。

2. 设备概况

浑江发电责任有限公司 1 号锅炉为亚临界压力自然循环固态排渣炉，型号为 SG-1025/17.5-M889。采用中储式热风送粉制粉系统，配置 4 台钢球磨煤机。采用四角切圆燃烧方式，双通道煤粉燃烧器布置有 4 层，其中 3 层设有大油枪。

炉膛宽度为 12800mm，深度为 11890mm，炉顶管中心线标高 58000mm。过热器由包墙过热器、低温过热器、分隔屏、后屏及高温过热器组成。再热器由低温再热器和高温再热器组成。后烟井为并联双烟道，后烟井前部为低温再热器烟道，后烟井后部为低温过热器烟道。在低温再热器和低温过热器的烟道下方布置有省煤器受热面。尾部竖井烟道中交错布置着上级省煤器、上级空气预热器、下级省煤器和下级空气预热器。过热蒸汽调温采用Ⅰ、Ⅱ级喷水减温方式，再热器的调温采用烟气挡板调温方式。

3. 改造方案

3.1 制粉系统改造方案

在中储式制粉系统中增加中温炉烟系统，送粉系统中加入由送风机出口引入的冷风作为调温风，如图 1 所示。中温炉烟管分左右 2 路引至炉前，再分 2 路进入 4 台磨煤机，管材为 12Cr1MoV。

根据相关试验结果，当制粉系统末端终端氧量低于 16%时，任何条件下霍林河褐煤都不发生爆炸。煤粉水分的选取直接影响制粉系统干燥能力，参考其它电厂掺烧褐煤的试验数据，将煤粉水分选取为 6%，送粉系统计算时选取为 5%。设计煤质与掺烧 50%褐煤的混配煤质特性示于表 1，中温炉烟系统及送粉系

Copyright © 2009 SciRes

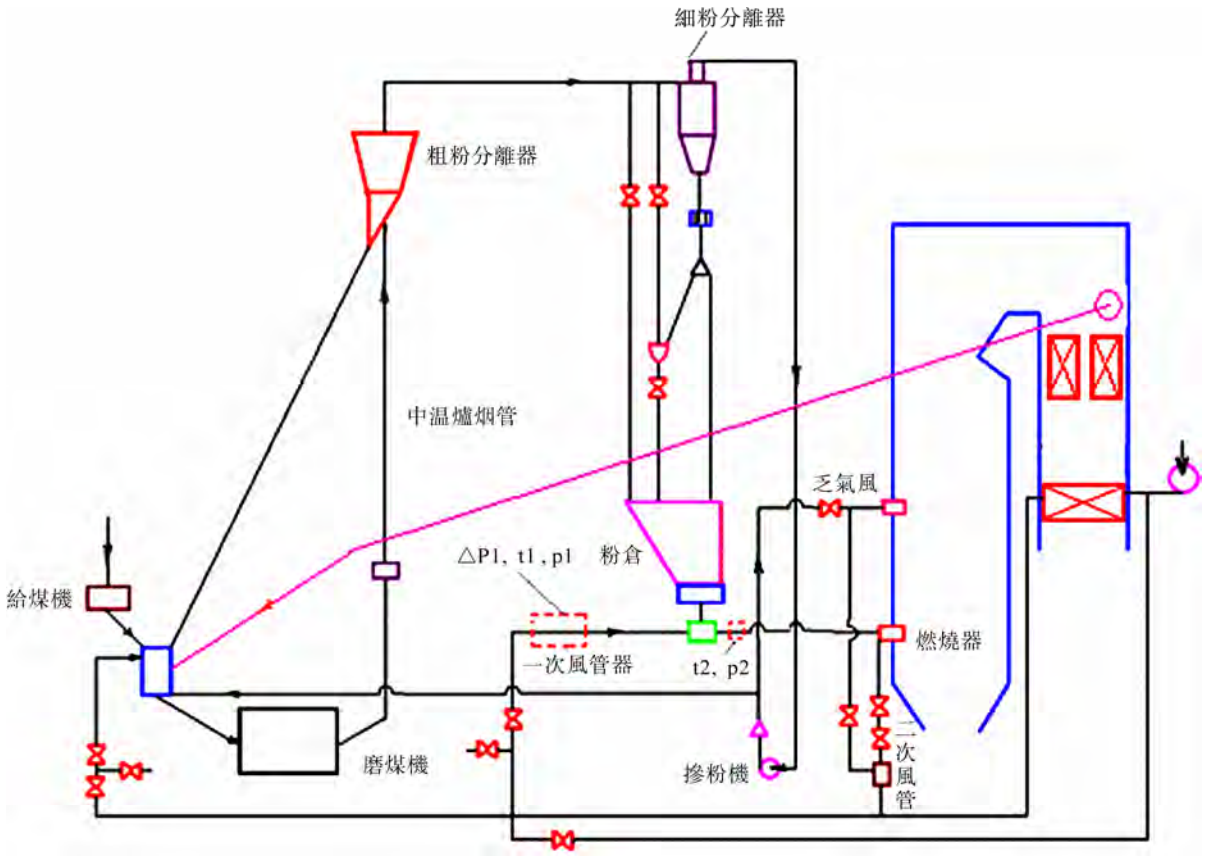

图1. 中温炉烟系统示意图

Figure 1. Piping arrangement diagram of warm flue gas system

表 1. 煤质主要特性表

Table 1. main characteristics of the coal

名 称	设 计 烟 煤	霍林河 褐 煤	混 配 煤 种
C_{ar}/%	43.38	35.75	39.67
H_{ar}/%	2.49	2.63	2.6
O_{ar}/%	5.3	9.67	7.76
N_{ar}/%	0.7	0.71	0.71
S_{ar}/%	0.41	0.34	0.37
M_{ar}/%	6.02	29.29	17.66
A_{ar}/%	41.7	21.61	31.23
V_{daf} /%	27.38	45.9	38.91
$Q_{ar,net}$/ kg · kg^{-1}	16200	12780	14530

统部分理论计算结果示于表 2，锅炉热力计算部分结果示于表 3。

由表 3 计算结果可知，在 BMCR 条件下锅炉计算效率将会降低 2.24%。而在实际运行时，制粉系统满负荷下通常只采用 2~3 套运行，很少采用 4 套同时运行，这样送粉系统所用冷风量会减少；掺烧褐煤后混煤燃尽率将会提高，机械未完全燃烧损失将会减少，实际运行中锅炉效率将会进一步提高。

Copyright © 2009 SciRes

表 2. 中温炉烟系统及送粉系统计算结果

Table 2. Calculation results of warm flue gas system and conveying system

名 称	计算结果
烟煤、褐煤比例	1:1
煤粉细度(R_{90})/ %	16
抽取点过量空气系数	1.27
一次风率/ %	23
空气干燥基水分/ %	5
煤粉水分/ %	5
实际燃料消耗量/ $t \cdot h^{-1}$	205
理论干空气量/$Nm^3 \cdot h^{-1}$	3.97
磨煤机最佳通风量/ $m^3 \cdot h^{-1}$	145779
中温炉烟占总烟气量的质量分额/%	5.4
制粉系统末端氧容积份额/%	13.9
系统阻力/ Pa	659
送粉系统气粉混合物温度/℃	90

表 3. 热力计算结果

Table 3. Thermal calculation results

项 目	四台磨投运 设计煤种 BMCR	四台磨投运 掺烧 50%褐煤 BMCR	磨煤机全停 掺烧 50%褐煤 BMCR	三台磨投运 掺烧 50%褐煤 ECR
空气预热器入口烟气量/ $t \cdot h^{-1}$	1339.2	1451.5	1406.3	1312.4
排烟温度（未修正）/℃	149	180	141	171
排烟温度（修正）/℃	139	171	133	161
低温过热器进口烟温/℃	648	660	652	643
锅炉热效率/%	90.80	88.56	90.96	89.08
计算燃料量/ $t \cdot h^{-1}$	178.5	202.5	196.2	183.1
实际燃料量/ $t \cdot h^{-1}$	182.9	207.5	201.0	187.6

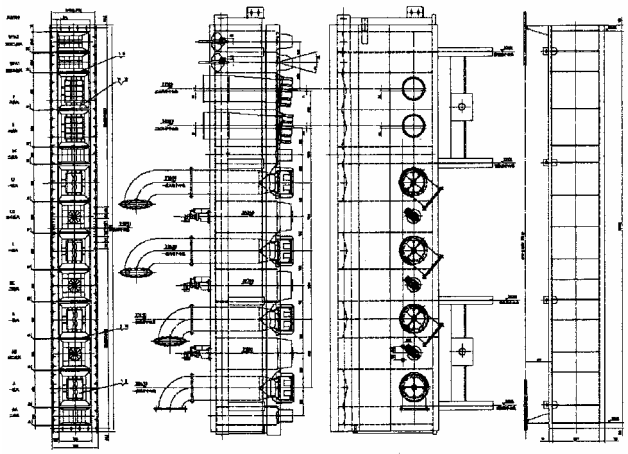

图 2. 煤粉燃烧设备示意图

Figure 2. Diagram of combustion burner

3.2. 燃烧器改造方案

燃烧器原设计采用大速差双通道煤粉燃烧器，一次风喷口布置相对集中。掺烧褐煤的混配煤质着火性能和燃尽性能提高，同时结焦倾向也增加，因此将燃烧器改为均等配风布置。燃烧器四角的安装角度不变，燃烧器水冷套不变，燃烧器各层风室重新分配（调整风室高度），调整全部一、三次风标高，调整二层刚性梁标高等。同时改变设计参数，如提高一次风率和风速等。燃烧设备示意图如图 2 所示。

该燃烧器设计特点如下：

(1) 采用中温炉烟+热风+冷风+再循环送粉系统。

(2) 一次风设计采用成熟的WR水平浓淡燃烧器。一次风喷嘴中装有 V 型钝体，在 V 型钝体前方形成稳定的回流区卷吸高温烟气，起到稳燃作用。燃烧器的一次风喷嘴采用均等布置，三次风喷嘴集中布置。

(3) 二次风设计按“加强混合，分级燃烧”的原则进行，既有利于着火、稳燃和燃烬，又减少 NO_x 的生成量。在燃烧器顶部设置 2 层燃烬风，为手动摆动喷嘴，其余喷嘴均为固定喷嘴。射流旋转方向与其余的一、二次风射流旋转方向相反，以减少锅炉水平烟道左右两侧的烟温偏差。

4. 中温炉烟系统投运试验

4.1. 抽热炉烟试验结果

为验证本次改造的实际效果，现场设备安装完成后，进行了磨煤机额定出力下抽吸中温炉烟试验。试验过程中炉烟调节挡板保持全开，通过改变磨煤机入口负压调整中温炉烟量以及制粉系统末端氧量。磨煤机入口负压与制粉系统末端含氧量、抽取烟气量的关系曲线如图 3、图 4 所示。

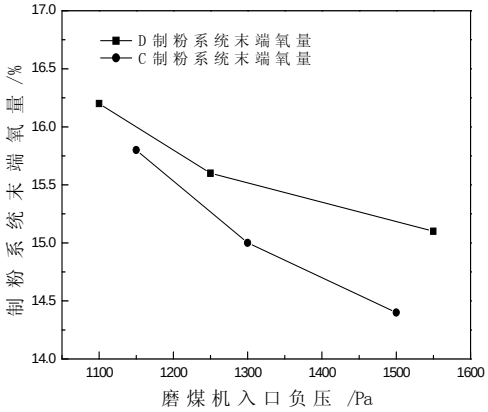

图 3. 磨煤机入口压力与制粉系统末端含氧量关系图

Figure 3. Interrelation between oxygen content at the end

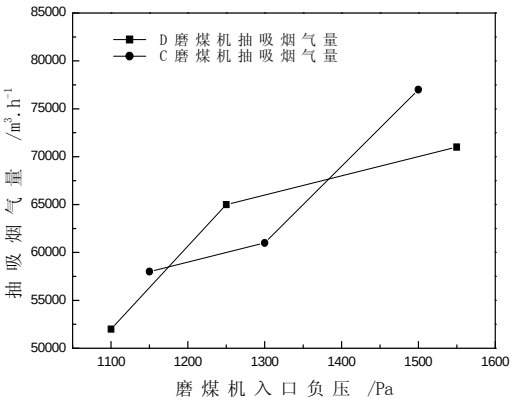

图 4. 磨煤机入口压力与抽取烟气量关系图

Figure 4. Interrelation between flue gas flow rate

表 4. NOx 排放量测试结果
Table 4. The NOx emissions results

名 称	测 试 数 据			
	33%比例褐煤		50%比例褐煤	
	不投运	投运	不投运	投运
机组负荷/ MW	209	211	213	211
空气预热器出口烟气含氧量/%	6.5	6.2	6.8	6.5
空气预热器出口 NOx 的体积浓度/ppm	199.4	183	227	195.3
折算后的预热器出口 NOx 的体积浓度/ ppm	205.6	186	239.8	202.2
空气预热器出口 NOx 的质量浓度/ mg · Nm^{-3}	421.5	381.2	491.6	414.5
降低幅度/%	9.6		15.7	
中温炉烟再循环率/%	6		7	

图 3 的试验数据表明，制粉系统末端含氧量随着磨煤机入口负压的增加呈现递减趋势。C、D 两套制粉系统正常运行时入口负压经常保持在 1300Pa 左右，末端含氧量低于 16%，满足了制粉系统的防爆要求。图 4 的试验数据表明，随着磨煤机入口负压的提高，抽取的中温炉烟量逐渐增加，磨煤机出口温度升高，制粉系统干燥出力增强，三个试验工况下磨煤机出口温度均能控制在 60℃以上。可见，改造后锅炉的防爆和干燥能力提高。

4.2. 低 NO_x 排放试验结果

燃煤电站低 NO_x 排放技术主要包括空气分级燃烧技术、燃料再燃烧技术、烟气再循环以及烟气处理 SNCR 和 SCR 方法[6-10]。在锅炉转向室抽取中温炉烟掺入制粉系统实现了烟气再循环利用，将双通道煤粉燃烧器改造为水平浓淡燃烧器实现了分级燃烧。

本文在浑江发电责任有限公司 1 号锅炉上进行了改造后 NO_X 排放试验，测点设在空气预热器出口处。表 4 为掺烧 33%和 50%比例褐煤时 NO_X 排放测试结果。

表 4 中的测试结果表明，改造后 NO_x 排放质量浓度均低于文献[11]中第 3 时段规定的最高允许排放质量浓度（450 mg · Nm^{-3}）。锅炉掺烧 33%比例褐煤、两套中温炉烟系统投运前后 NOx 排放质量浓度分别为 421.5 mg · Nm^{-3} 和 381.2 mg · Nm^{-3}，后者比前者降低了 9.6%。锅炉掺烧 50%比例褐煤、两套中温炉烟系统投运前后 NOx 排放质量浓度分别为 491.6 mg · Nm^{-3} 和 414.5 mg · Nm^{-3}，后者比前者降低了 15.7%。这是由于掺烧褐煤后，由于混煤水分增加，炉膛火焰温度有所降低，减少了热力型 NO_X 的生成；中温炉烟作为一次风进入燃烧器区域后，降低了燃烧器区域的氧气浓度，抑制煤粉燃烧中燃料型 NO_x 的形成。同时，双通道煤粉燃烧器改造为水平浓淡燃烧器，进一步减少了燃料型 NO_x 的形成，从而减轻了对大气环境的污染。

5. 结 论

（1）在锅炉转向室抽取中温炉烟掺入制粉系统、在送粉系统加入冷风作为调温风的改造技术，增强了 1025t/h 锅炉中储式制粉系统的防爆能力和干燥能力；双通道煤粉燃烧器改造为水平浓淡燃烧器，解决了燃烧器烧损问题，达到了劣质烟煤锅炉中大比例掺烧褐煤的预期目标。

（2）由于水平浓淡燃烧技术与烟气再循环利用的双重影响，降低了 NOx 的排放量，因此中储式制粉系统烟煤锅炉掺烧褐煤的改造技术同样是一种重要的减排技术。

REFERENCES

[1] J. W. Shu, F. B. Meng, Q. L. Huang, *et al*., “The calculation and selection of drying agents in connection with the change of fuel for a boiler from brown coal to bituminous coal,” Journal of Engineering for Thermal Energy and Power, Vol. 7, pp. 453–456, 2001.

[2] J. Guo, R. Jiang, and H. C. Zeng, “Formation of NOx during blended coals combustion process and it’s computer simulation,” Power System Engineering, Vol. 10, No. 2, pp. 55–60, 1999.

[3] Y. H. Li, H. W. Chen, J. Z. Liu, *et al*., “Numerical simulation of blending coals combustion of 800 MW boiler,”

Proceedings of the CSEE, Vol. 22, No. 6, pp. 101–104, 2002.

[4] J. X. Wu, H. G. Chen, J. F. Ma, *et al*., "Feasibility study on the hot flue gas mixture in coal pulverizing system of 200MW boiler," Electric Power, Vol. 39, No. 3, pp. 22–25, 2006.

[5] J. F. Ma, J. X. Wu, T. S. Zhou, *et al*., "Study on lignite blended burning technology in the bin and feeder coal pulverizing system," Journal of Power Engineering, Vol. 28, No. 1, pp. 14–18, 2008.

[6] S. Miyamae, T. Kiga, H. Ikebe, K. Makino, *et al*., "Low NO_x pulverized coal combustion technology for large utility thermal power plant," Coal Combustion Science and Technology of Industrial and Utility Application, Hemisphere Publishing Corporation, New York, 1988.

[7] M. Berg and H. Bering, "Development of a low-NO_x burner for pulverized- coal combustion and retrofitting of a full-scale power plant boiler," Proceedings of the 2nd International Symposia on Coal Combustion, China Machine Press, Beijing, 1991.

[8] E. Troconi, L. Lietti, P. Forzatti, *et al*., "Experimental and theoretical investigation of the dynamics of the SCR-DeNO_x reaction, Chemistry Science, Vol. 51, No. 11, pp. 2965–2970, 1996.

[9] C. G. Yin, S. Cailat, and J. Harion, "Investigation of flow, combustion, heat-transfer and emission from a 609MW utility tangentially fired pulverized-coal boiler," Fuel, Vol. 81, No. 8, pp. 997–1006, 2002.

[10] M. Falcite, S. Pasini, and L. Tognotti, "Modeling paractical combustion systems and predicting NO_x emission with an integrated CFD based approach," Computers and Chemical Engineering, Vol. 26, No. 9, pp. 1171–1183, 2002.

[11] Fossil-fuel Power Plant New Atmospheric Pollutant Emission Standard, GB13223-2003, Electric Power Press, Beijing, China, 2003.

Copyright © 2009 SciRes

Energy and Power Engineering, 2009, 122-127
doi:10.4236/epe.2009.12019 Published Online November 2009 (http://www.scirp.org/journal/epe)

The Resuming Insulation Discharge Failure and Conductor Overheating Failure Judgment Method of SF_6 Electrical Equipment

Xiansheng ZHUANG, Zhi LI, Chengji HUANG
Electric Power Research Institute of Guangdong Power Grid Corporation, Guangzhou, China
Email: *zhuangxs@163.com*

Abstract: Through the long time track examination and disintegration to SF_6 circuit breaker, we obtain the massive monitor data and massive pictures. The criteria of resuming insulation discharge failure conforming to $C_{SO2}/C_{H2S}>7$, is quite broad to SO_2 and the H_2S concentration permission. Even if it reaches 100μL/L, it will not be in danger immediately to the safe operation of equipment. We may plan, arrange, and overhaul calmly. When obtaining the bare conductor overheating failure, it has not involved the resuming insulation. We may use the resuming insulation discharge failure criterion.

Keywords: SF_6; conductor, discharge, overheated, failure, method

1. 引 言

随着 SF_6 电气设备的大量使用，设备内部各种放电和过热故障时有发生，严重影响 SF_6 电气设备的安全、可靠运行。目前，在国际上，还没有关于 SF_6 电气设备内部放电和导体过热故障的判断标准，IEC60480[1]只是给出了运行中 SF_6 电气设备 SF_6 气体中分解物的最大限值。在国内，《The examination and judgment of SF_6 Electrical Equipment Discharge Failure》[2]给出了有关 SF_6 电气设备内部放电判断依据。本文通过对有故障设备进行长时间的跟踪监测，最后对设备进行检修解体，获得大量的监测数据和图片等资料，总结出 SF_6 电气设备自恢复绝缘放电故障和导体过热故障的判断依据，对 SF_6 电气设备的放电故障判断具有重要意义。

2. 设备概括

某公司110kV六氟化硫组合电器，设备参数如下：

设备型号：QF1-110,额定电压：110kV，额定电流：1250A，额定开断电流：31.5kA，制造日期：1988 年。

3. 设备运行历史

该设备 1988 年投厂后，2001 年 12 月 19 日发生＃1 主变 110 高压侧 B 相户外侧套管断裂掉下短路事故。

3.1. 事故单元概况

事故前运行工况：黄石甲线经127开关送110KV乙母线带1#、2#、3#主变运行，黄石乙线经128开关送110KV甲母线空载热备用。

6KV 系统：6023 分段开关“合”（上主 6KVⅤ、Ⅵ段）；6012 分段开关“合”（上主 6KVⅠ、Ⅱ段）；6015 母联开关“合”（上主 6KVⅠ、Ⅴ段）；6025 母联开关“分”作热备用状态；6034 分段开关“合”（上主 6KVⅢ、Ⅳ段）;6046 母联开关“合”(上主 KV Ⅳ、Ⅵ段）；6036 母联开关“分”作热备用状态。

3.2. 事故经过

2001 年 12 月 19 日 8:12 时，1#主变高压侧 B 相穿墙套管户外侧突然断裂掉下，110KV 乙母对地短路。1#主变保护动作跳主变低压侧开关、高压侧 101 开关拒动；2#主变“零序过流”保护动作跳主变两侧开关；3#主变“复合电压闭锁过流”保护动作跳主变两侧开关；4#主变“复合电压闭锁过流”保护动作跳主变两侧开关及 6034、6046 母联开关。厂电力系统与市网解列运行，同时黄埔电厂 127 开关也跳闸，厂主 6KV 系统分成三个独立系统运行。8:14 时 2#发电机“复合电压闭锁过流”保护动作跳闸，热 116 开关保护跳闸，乙

Copyright © 2009 SciRes

烯单回路供电；黄埔电厂 127 开关重合闸时，101 开关保护动作跳开。

3.3. 事故处理过程及恢复情况

12 月 29 日更换 1#主变高压侧三个穿墙套管，12 月 30 日 16:50 时 1#主变送电并网运行。

3.4. 事故原因分析

3.4.1. 主要原因

#1主变高压侧B相穿墙套管户外侧突然断裂，造成110kV乙母B相对地短路。套管断裂的原因是套管本身质量存在缺陷:套管瓷体有未烧透的夹层；固定套管的法兰存在旧裂纹，内应力作用使套管断裂，断裂后放电，断口靠乙母侧的套管内壁有严重的放电烧弧痕迹，而另一侧套管内壁则没有。

3.4.2. 间接原因

1#主变第一次差动保护动作后，101 开关拒动，未能及时切断故障点。使事故影响范围扩大。

101 开关拒动是由于操作机构的液压油受低温天气影响，油粘度大，机构动作迟缓。

4. 故障的发现、判断和追踪监测情况

4.1. 放电故障的发现

2008 年 2 月 26 日，应某公司要求，对某公司所属的 SF_6 电气设备进行水分、二氧化硫和硫化氢的预防性试验，全部测试六氟化硫组合电器 252 个气室（110kV 加氢联合变 23 气室、热电站 32 气室、热电站升压变 8 气室、乙烯总降 14 气室、动力二站 68 气室、炼化站 107 气室），除热电站 110kVGIS＃1 主变 101 开关以外，其他气室未发现异常放电缺陷。热电站 110kVGIS＃1 主变 101 开关气室 SF_6 气体中，二氧化硫浓度大于 146μL/L，硫化氢浓度 26.14μL/L，判断该设备存在异常放电故障，建议有条件尽快检修，测试结果见表 1。

2008 年 3 月 5 日应厂方要求，分相测试二氧化硫和硫化氢，并取样测试气体分解产物。测试结果判断故障点在 B 相，其他两相是否存在放电缺陷需要进一步确认。

从测试结果看，虽然 B 相二氧化硫浓度大于 146μL/L，超过仪器检测最高限，可以判断 B 相内部存在或曾经发生过放电故障，存在放电缺陷；从二氧化硫和硫化氢浓度比值大于 7（从 2008 年 2 月 26 日和 2008 年 3 月 5 日测试结果综合判断），可以判断放电缺陷属自恢复绝缘放电故障，放电部位和放电通道主要涉及自恢复绝缘。当时判断对设备的运行没有即时危险性。

4.2. 追踪测试

由于通过检测六氟化硫电气设备中二氧化硫和硫化氢组分浓度，判断设备是否存在放电缺陷以及放电的类型、涉及的绝缘种类（自恢复绝缘或非自恢复绝缘），在目前还是新生事物，还没有相关的规程和标准。厂方对我们的判断有所保留，仍然不相信该设备存在异常放电故障。为了便于监测，2008 年 3 月 5 日对 101 开关进行更换 SF_6 气体工作。24 小时后，3 月 6 日进行现场测试和取样测试。2008 年 3 月 6 日～2008 年 10 月 23 日追踪测试结果汇总见表 1。

10 月 23 日检测结果，二氧化硫已经超过仪器检测最高限。2008 年 12 月 1 日再次对 101 开关进行更换 SF6 气体处理，并把设备停运（处于冷备用状态）。并跟踪检测二氧化硫和硫化氢（此时二氧化硫和硫化氢为吸附剂释放结果，非由设备放电产生），与以前的检测结果对比，以判断二氧化硫和硫化氢增长是否由设备内部放电产生。

101 开关冷备用状态跟踪测试进行了 4 个月，检测结果汇总见表 1。

4.3. 更换 101 开关

通过 101 开关的运行和停运测试结果对比，可以判断 101 断路器存在放电故障。厂方联系北京开关厂，于 2009 年 5 月 1 日对 101 开关进行更换检修工作。更换后的检测结果见表 1。从表 1 可以看出，101 开关更换检修以后，两次检测结果都未检出二氧化硫和硫化氢，说明故障消除。

5. 101 开关解体情况和故障分析

5.1. 固体绝缘完好，满足断路器运行绝缘要求

1) 支撑绝缘筒内部和外部玻璃纤维环氧树脂绝缘件都没有损伤和破坏。

2) 支撑绝缘杆（6根）（玻璃纤维环氧树脂绝缘件）表面未发现任何损伤和破坏。

3) 上下出线绝缘子（绝缘盘）（环氧树脂绝缘件）表面未发现任何损伤和破坏，虽然上绝缘子表面粘附

Copyright © 2009 SciRes

表1. 110kVGIS #1主变101开关追踪测试结果汇总
Table 1. 101 breaker sulfur hexafluoride gas component test result

测试项目 item	空气	四氟化碳	六氟化硫	二氧化碳	氟化亚硫酰	氟化硫酰	十氟化二硫酰	二氧化硫	硫化氢
测试日期 date		CF_4	SF_6	CO_2	SOF_2	S_2OF_{10}	S_2OF_{10}	SO_2	H_2S
	%m/m	%m/m	%m/m	%m/m	%m/m	%m/m	%m/m	μL/L	μL/L
2008年 2月 26日	-	-	-	-	-	-	-	>146	26.14
2008年 3月 5日 A	0.0246	0.1325	99.79	0.0093	0.0016	0.029	0.0132	6.86	0.43
2008年 3月 5日 B	0.0268	0.2335	99.70	0.0169	0.0018	0.011	0.0078	>146	59.14
2008年 3月 5日 C	0.0292	0.1227	99.81	0.0083	0.0017	0.016	0.0127	14.71	1.00
2008年 3月 6日	0.0070	0.0045	99.989	未检出	未检出	未检出	未检出	6.29	0.00
2008年 3月 12日	0.0011	0.0031	99.983	未检出	0.0131	未检出	未检出	23.86	1.00
2008年 4月 14日	0.0012	0.0020	99.997	未检出	未检出	未检出	未检出	45.29	5.16
2008年 5月 27日	0.0012	0.0036	99.995	未检出	未检出	未检出	未检出	60.43	8.86
2008年 7月 29日	0.0059	0.0059	99.971	未检出	0.0042	未检出	0.0131	79.00	10.14
2008年 8月 26日	0.0020	0.0036	99.984	未检出	0.0008	未检出	0.0093	96.43	13.71
2008年 9月 24日	0.0132	0.0010	99.986	未检出	0.0042	未检出	0.0131	100.6	14.14
2008年 10月 23日	-	-	-	-	-	-	-	>146	25.14
2008年 12月 2日	-	-	-	-	-	-	-	1.74	0.09
2009年 1月 6日	-	-	-	-	-	-	-	3.34	0.24
2009年 2月 10日	-	-	-	-	-	-	-	5.44	0.94
2009年 3月 13日	-	-	-	-	-	-	-	7.61	1.01
2009年 5月 9日	-	-	-	-	-	-	-	未检出	未检出
2009年 5月 18日	-	-	-	-	-	-	-	未检出	未检出

的粉尘有放电痕迹，但粉尘擦除后发现粉尘表面的放电痕迹并未伤及绝缘子。

4) 操作传动绝缘杆（玻璃纤维环氧树脂绝缘件）表面未发现任何损伤和破坏。

5.2. 导体电流路径有些损伤，但基本仍能满足开关运行要求

1) 上下出线导体触头有受电弧灼伤过热痕迹。触头触子接触位置保持良好。

2) 动触头受电弧灼伤过热，损伤较严重，多数触子仍能与静触头保持良好接触，满足额定电流通过要求。动触头触子与上下静触头接触位置明显接触划痕不均匀。说明动触头触子由于受电弧高温灼伤，接触压紧力受影响。

3) 上下静触头虽然受电弧灼伤过热较严重，但与动触头触子的接触电阻仍能满足额定电流通过要求。下静触头石墨喷嘴受电弧烧蚀严重。由于动触头触子接触压紧力不均匀且上下静触头受电弧高温灼伤、过热，表面氧化严重，运行电流大时容易产生过热。

5.3. 自能压气灭弧室损伤严重，严重影响灭弧室的吹弧能力，基本丧失对开断短路电流的灭弧能力

1) 压气室上密封盖脱落，并且烧蚀严重，基本丧失自能高压吹弧功能。

压气室外筒为玻璃丝编织绝缘件；压气室密封盖

材料为聚四氟乙烯。两者采用胶粘固定在一起。一方面在断路器分闸过程中跟随动触头向下移动，与固定活塞作用使压气室空间缩小从而产生高压气体满足吹弧要求；另一方面在电弧的高温作用下，压气室中气体产生吹弧需要的高压。

由于密封盖松脱，使压气室内部不能保持产生高压气体，虽然根据设计要求，仍能满足开断额定电流以下的操作,但已严重影响对短路大电流的灭弧能力，有可能产生严重后果

2) 根据断路器内部情况、灭弧室损坏情况可以判断断路器曾经发生未能按断路器功能要求及时灭弧，从而产生如下几方面的损坏或损伤：

a) 压气室内部空间由于未能及时灭弧，在电弧高温作用下，压气室外筒与密封盖之间的胶粘融化失去粘接能力，在压气室内高压气体作用下而松脱。

b) 由于较长时间的燃弧，使密封盖烧蚀严重；

c) 下静触头石墨喷嘴烧蚀严重；

d) 动触头触子受损，影响接触压紧力；

e) 压气室外筒受热，温度升高，表面的胶漆熔融或滴落。

f) 从石墨喷嘴烧蚀位置和压气室密封盖烧蚀位置基本在同一垂直线上，可以判断电弧热气流从该位置上升喷出压气室外。

从石墨烧蚀喷嘴、动触头的水平相对位置，可以判断断路器已经产生开断动作，动触头与上静触头之间在刚要脱离瞬间，即已开始燃弧，由于断路器操作机构原因或是由于电磁力的作用，造成断路器的开断动作没能继续，也就没有进入吹弧阶段，压气室内空间在高温电弧作用下，气体压力极高，电弧热气流冲开密封盖外泄。燃弧时间持续到其他保护跳闸，切断母线和主变电流而熄灭。

g) 石墨喷嘴烧蚀产生的分解物主要为四氟化碳（CF_4），在 2008 年 3 月 5 日以前的测试数据中，四氟化碳浓度很高，见表 1，A 相 0.1325%m/m，B 相 0.2335%m/m，C 相 0.1227%m/m。

在 101 开关更换 SF_6 气体以后，从 2008 年 3 月 6 日～2008 年 10 月 23 日，几个月的跟踪测试，四氟化碳浓度都变化不大，基本在 0.0060%m/m 以下。说明在 2008 年 3 月 6 日～2008 年 10 月 23 日的时间范围内，未曾发生过未能按断路器功能要求及时灭弧的情况，即在该时间段内，断路器没有发生大电流、长时间燃弧的情况。

5.4. 由于高温粉尘等材料落下，造成断路器底座油漆熔融或松脱。

5.5. 断路器的正常开断、闭合和异常开断、闭合

断路器的开断和闭合操作燃弧可以分为正常燃弧和异常燃弧，这些都是属于有目的性的操作，并且燃弧一般都是局限在灭弧室内部，不属于断路器异常放电范围。

5.5.1. 断路器的正常开断和闭合

断路器正常开断燃弧和灭弧过程，由于灭弧室的特殊设计，电离、离子化、分解的SF_6气体在该过程结束后一般都能很好的复合。SF_6气体由于断路器正常开断和闭合过程产生的分解产物极少，设备内部的吸附剂可以慢慢把它吸附。根据多年的检测结果显示，正常开断和闭合的断路器，即使运行十几、二十年的断路器，其内部的SF_6气体都检测不到二氧化硫和硫化氢，这是可以利用检测二氧化硫和硫化氢作为判断断路器内部异常放电缺陷的首要前提条件。

5.5.2. 断路器的异常开断和闭合

断路器异常开断和闭合，分以下几种情况：

1) 断路器开断、闭合过程燃弧，但由于操作机构或其他原因造成断路器不能延续开断、闭合动作，需要其他保护动作，切断电源电流而灭弧；

2) 断路器在开断、闭合过程不能有效灭弧，需要其他保护动作，切断电源电流而灭弧；

3) 断路器开断、闭合额定短路电流以上的电流。

断路器异常开断和闭合，有如下特点：

1) 由于都是有目的性的操作，异常现象当时就能发现。

2) 都会对灭弧室动、静触头，吹弧喷嘴，压气室等造成不同程度的烧蚀或其他损害；

3) 都会产生不同浓度的二氧化硫和硫化氢等分解产物，浓度相对正常操作状态大得多。

4) 发现异常现象以后，及时进行分析、检测，就能判断断路器是否受到损害，断路器功能是否仍然有效，及时采取必要的措施，包括继续追踪监测、检修等，就能确保设备的安全运行。

如本文中 101 开关情况，如果及早进行分解产物二氧化硫和硫化氢监测，就能及时发现 101 开关的缺陷。幸好 101 开关灭弧室受到损害以后，未曾开断短路大电流。

Copyright © 2009 SciRes

5.6. 断路器内部异常放电和过热缺陷

设备内部异常放电缺陷不包括以上断路器正常、异常开断和闭合情况。虽然断路器异常开断和闭合，电弧的能量异常大或不受控，与断路器正常开断、闭合相比，会产生大量的SF_6分解产物。这些属于设备操作异常，这种操作异常事后是可知的。

设备内部异常放电缺陷是无目的性的、未知的、由于某些原因而在设备内部悄然进行的现象。由于是未知的，未能及时发现，特别是非自恢复绝缘的放电，对设备安全造成较大威胁。所以，需要象设备预防性试验一样，定期进行分解产物二氧化硫和硫化氢的检测，才能尽早发现设备内部的异常放电缺陷，采取必要的措施，确保设备安全运行。

根据对 101 开关的一年多的跟踪监测，判定 101 开关内部存在异常放电缺陷。并且根据二氧化硫和硫化氢比值大于 7 判定，异常放电主要涉及自恢复绝缘。

根据 101 开关解体情况，101 开关内部异常放电和过热缺陷并存，要分清楚放电痕迹是在追踪测试期间还是以前发生有些困难，根据解体情况判断，101 开关在追踪监测期间，放电和过热并存。有以下几方面：

5.6.1. 局部放电（电晕放电）

由于断路器开断大电流失败以后，燃弧时间过长，灭弧室内部气体压力极高。高压气体几乎像产生爆炸似地从灭弧室外泄，气体夹带大量粉尘。电弧熄灭以后，粉尘慢慢沉积在设备内部表面。

一方面由于灭弧室压气盖松脱，另一方面压气盖一边烧蚀严重。在合闸状态下，压气盖处于上静触头位置，在上静触头周围产生严重不均匀电场。由于灭弧室内部受损严重，下静触头的石墨喷嘴严重烧蚀产生凹坑等，造成喷嘴附近场强畸变，产生严重极不均匀电场。灭弧室的严重破坏，造成内部极不均匀电场，在高场强区域产生局部放电。

另外，上下绝缘盘的连接触头导体表面也产生电晕放电。

5.6.2. 裸导体过热

101 开关上下静触头材料为钢合金，与动触头触子接触表面为铜钨合金，端部喷口封接石墨作为灭弧喷嘴。

101开关动触头主要材料也是钢合金，触子为铜合金和铜钨合金。

101开关由于经历过开断短路大电流失败，对灭弧室内部造成极大的损害。特别是动触头触子及其电流路径材料的损害，接触压紧力受影响，一方面造成触子与上下静触头接触不均匀，这从触头触子与静触头的接触移动划痕可以看出来。

静触头表面氧化严重，氧化层厚度大，影响接触电阻。在运行电流较大时，容易产生导体过热。

一方面由于灭弧室压气盖松脱，另一方面压气盖一边烧蚀严重。在合闸状态下，压气盖处于上静触头位置。在上静触头周围产生严重不均匀电场，引起局部放电。

101 断路器的导体过热（没有涉及非自恢复绝缘（固体绝缘）），使六氟化硫气体分解，产生的特征组分浓度含量特征与裸金属放电特征基本一致，二氧化硫和硫化氢比值判定标准一样适用。

5.6.3. 底座粉末主要成分

抽取101开关B相底座粉末进行发射光谱测试，主要金属成分为铜和钨。基本符合铜钨触头合金的成分比例，说明设备中触头烧蚀严重。

101 开关 B 相底座粉末粉尘测试非金属成分结果：S3.52%，C29.64%。石墨为非金属碳的一种结构形式；聚四氟乙烯是碳的氟化物。从粉末测试结构含碳 29.64%，石墨喷口和聚四氟乙烯密封盖烧蚀严重。

6. 结 论

1) 检测 SF_6 电气设备 SF_6 气体中 SO_2 和 H_2S 的浓度判断 SF_6 电气设备内部放电和过热故障是有效的手段。结合预防性试验周期，进行 SF_6 电气设备 SF_6 气体中 SO_2 和 H_2S 的定期检测，可以及早发现 SF_6 电气设备内部的异常放电和过热故障。

2) SF_6 电气设备自恢复绝缘放电故障可以用 SO_2 和 H_2S 的浓度比值 $C_{SO2}/C_{H2S}>7$ 判据准确判断。SO_2 和 H_2S 的浓度允许比较大，即使浓度达到 100 μL/L，仍然不会对设备安全运行产生即时的危险，可以从容地计划、安排检修。

3) 裸导体过热，可以使用自恢复绝缘放电故障的判据进行故障判断；导体过热，如果涉及非自恢复绝缘（固体绝缘），由于多数固体绝缘分解温度较低，容易产生 H_2S 等其他气体，C_{SO2}/C_{H2S} 的数值就不同，这时可以用非自恢复绝缘放电故障判据。

Copyright © 2009 SciRes

4) 对于断路器开断、闭合操作过程异常，出现拒动、不能正常开断、闭合的操作，属于设备操作异常。必须测试 SF_6 气体分解产物 SO_2 和 H_2S 浓度,并查明原因。

5) 对于断路器开断、闭合额定短路开断电流以上的操作，应及时测试 SF_6 气体分解产物 SO_2 和 H_2S 浓度,确认断路器内部无异常，才能继续运行。

REFERENCES

[1] IEC 60480–2004, "Guidelines for the checking and treatment of sulfur hexafluoride (SF6) taken from electrical equipment and specification for its re-use", 2004.

[2] X. S. Zhuang, "The examination and judgment of SF6 electrical equipment discharge failure," Asia-Pacific Power and Energy Engineering Conference (APPEEC'09), 2009.